Structure determination of a retinal rod G protein peptide segment bound to rhodopsin by nuclear magnetic resonance spectroscopy
by Julie Ege Furstenau

A thesis submitted in partial fulfillment of the requirements for the degree of Doctor of Philosophy in Chemistry
Montana State University
© Copyright by Julie Ege Furstenau (1994)

Abstract:
The goal of this research project is to investigate the three-dimensional structure of a specific peptide segment of the retinal rod G protein, transducin, bound to light excited rhodopsin. This segment has been shown to exhibit biological activity in much the same fashion as the full G protein. The segment studied consists of a modified portion of the C-terminus of the alpha subunit of transducin that runs from amino acid numbers 340 to 350. The peptide chain has been modified to prolong its biological activity by the addition of N-terminal acylation, and the substitution of a lysine for an arginine in the 341 position.

This project studied this peptide segment using two-dimensional nuclear magnetic resonance and computer refinement methods. The goal was to determine if the peptide has significant structure when free in solution, in the presence of bovine rhodopsin in an unactivated state, and finally bound to rhodopsin in its light excited form.

The NOESY build-up rates were somewhat similar for the dark- and light-bound experiments although significantly more cross-peaks were observed in the light-bound experiments. The new cross-peaks were mainly from sidechain interactions and interactions on the C-terminal end of the peptide. The sidechain cross-peaks suggest more intimate binding in the light, and the increase in C-terminal cross-peaks suggests that this end is important in the light binding. Measurement of the peptide-protein exchange rates shows fast exchange on the cross-relaxation time scale. The final structures obtained using iterative MARDIGRAS refinement are consistent with the idea of tighter binding in the light; the dark-bound structures qualitatively show less overall agreement with each other than the light-bound structures.

This project has yielded preliminary structures for the metarhodopsin 11-bound peptide segment. Work continues in this laboratory to better define the dark- and light-bound structures and yield further understanding of this protein interface.

STRUCTURE DETERMINATION OF A RETINAL ROD G PROTEIN PEPTIDE SEGMENT BOUND TO RHODOPSIN BY NUCLEAR MAGNETIC RESONANCE SPECTROSCOPY

by

Julie Ege Furstenau

A thesis submitted in partial fulfillment
of the requirements for the degree

of

Doctor of Philosophy

in

Chemistry

MONTANA STATE UNIVERSITY
Bozeman, Montana

July 1994

D378
F9834

APPROVAL

of a thesis submitted by

Julie Ege Furstenau

This thesis has been read by each member of the thesis committee and has been found to be satisfactory regarding content, English usage, format, citations, bibliographic style, and consistency, and is ready for submission to the College of Graduate Studies.

8/4/94
Date

Edward Gadwat
Chairperson, Graduate Committee

Approved for the Major Department

8/4/94
Date

David M Dooley
Head, Major Department

Approved for the College of Graduate Studies

8/12/94
Date

R A Brown
Graduate Dean

STATEMENT OF PERMISSION TO USE

In presenting this thesis in partial fulfillment of the requirements for a doctoral degree at Montana State University, I agree that the Library shall make it available to borrowers under rules of the Library. I further agree that copying of this thesis is allowable only for scholarly purposes, consistent with "fair use" as prescribed in the U.S. Copyright Law. Requests for extensive copying or reproduction of this thesis should be referred to University Microfilms International, 300 North Zeeb Road, Ann Arbor, Michigan 48106, to whom I have granted "the exclusive right to reproduce and distribute my dissertation for sale in and from microform or electronic format, along with the right to reproduce and distribute my abstract in any format in whole or in part."

Signature Julie E Fristenau

Date August 1994

ACKNOWLEDGEMENTS

I would like to thank the people who have contributed their expertise, time and support to this project. Dr. Edward Dratz, my advisor, allowed this project to continue on a "start-and-stop" basis to accommodate my schedule, posed the problem and approach initially, and has contributed valuable insights into the interpretation of the material in this thesis. I would also like to thank the members of the Dratz lab group, past and present, for the everyday contributions they have made. I would particularly like to thank Craig Johnson for his synthesis of peptides and David Poole and Chris Lambert for their computer help and expertise. Funding support for this project came from MSU, NSF, NIH, CTR, and MT Center for Excellence in Biotechnology.

Earle Adams must be singled out for his support. Without his making sure that there would be peptides, membranes, NMR time and advice available to me when I returned each summer, I would have never finished this work.

I would like to thank the people who have provided "moral support" during my summer stays in Bozeman. Michelle and Paul McGrane, the David McLaughlin family, and Dr. and Mrs. John Amend have all provided friendship when it was most needed. Finally, I would like to thank my parents for starting me on the quest for knowledge long ago and, most importantly, my husband Ron for eating TV dinners without complaint for three summers and ALWAYS supporting me in this endeavor.

TABLE OF CONTENTS

Page

1. BACKGROUND AND LITERATURE REVIEW 1

Introduction 1
Overview of G-Proteins 2
The Rhodopsin - G_t Interaction 4
Relevant NMR Theory 11
The One-Dimensional NMR Experiment 11
Relaxation Experiments 13
The Two-Dimensional Experiments 15
The Two-Dimensional Scalar Coupling Experiments: Through-Bond Correlations 16
The Two-Dimensional Dipolar Relaxation Experiments: Through-Space Correlations 18
Investigating the Bound Structure: The Transferred NOESY Experiment 26
Kinetics of the Peptide-Receptor Exchange 28
Computer Methods 30
Energy Minimization 30
Molecular Dynamics 31
Simulated Annealing 32
MARDIGRAS Structure Refinement 32
Applications of NMR Methods to Peptide and Protein Structure: A Brief Look at the Literature 35

2. STATEMENT OF THE PROBLEM TO BE SOLVED 38

3. EXPERIMENTAL PROCEDURES 39

Preparation of Bovine Rhodopsin and Peptides 39
Preparation of NMR Samples 43
NMR Hardware Conditions 45
NMR Signal Processing 46

4. EXPERIMENTAL DATA 47

Ac-340-350(K341R)/Rhodopsin Stability Studies 47
Free Ac-340-350(K341R) 53
Spectral Assignment 53
NOE Build-up Rates 56
Relaxation Rates 59
Ac-340-350(K341R) + "Dark" Membranes 60
Spectral Assignment 60
NOE Build-up Rates 61
Peptide-Protein Exchange Kinetics 64
Ac-340-350(K341R) + "Light" Membranes 67
Spectral Assignment 67
NOE Build-up Rates 68
Peptide-Protein Exchange Kinetics 70

5. ANALYSIS AND COMPUTER SIMULATIONS 76

Initial Analysis of the 2D NMR Data 76
Energy Minimization and Molecular Dynamics 77
Simulated Annealing 79
Refinement of the Dark-Bound Structure 80
Discover Analysis 80
MARDIGRAS Refinement 89
Refinement of the Light-Bound Structure 94
Discover Analysis 94
MARDIGRAS Refinement 99
Discussion and Conclusions 103

REFERENCES CITED 108

APPENDIX 116

LIST OF TABLES

Table Page

1. G-Protein designations and functions 3
2. Sample calculation of rhodopsin concentration in ROS membranes 41
3. Stability of Peptide/MII complexes 53
4. Assignment of proton shifts in the free Ac-340-350(K341R) peptide . . . 58
5. Values used to best fit experimental $R_{1\rho}$ vs ω_{SL} data (dark-bound) 67
6. Values used to best fit experimental $R_{1\rho}$ vs ω_{SL} data (light-bound) 74
7. Simulated Annealing Results: Backbone atom RMSD agreement between the first SA generated dark-bound structure and the other SA generated structures 82
8. Simulated Annealing Results: Structure number vs Total energy (dark) 84
9. Simulated Annealing Results: Structure number vs NOE violations (dark) 84
10. MARDIGRAS R and Q factors vs τ_c^{eff} (dark) 92
11. Selected dark NOE distance restraints (lower limit) throughout the course of MARDIGRAS and molecular dynamic iterations 94
12. Simulated Annealing Results: Structure number vs Total energy (light) 99
13. Simulated Annealing Results: Structure number vs NOE violations (light) 99

14. MARDIGRAS R and Q factors vs τ_c^{eff} (light) 100

15. Selected light NOE distance restraints (lower limit) throughout the course of MARDIGRAS and molecular dynamic iterations 103

LIST OF FIGURES

Figure Page

1. The rhodopsin photocycle 5
2. Cross-section of a rod outer segment 6
3. Primary sequence of the rhodopsin protein 7
4. Proposed model of rhodopsin - G_t binding 8
5. The cGMP model of activation in the vertebrate rod 8
6. The primary sequence of the modified $G_t\alpha$ peptide Ac-340-350(K341R) 10
7. The one-dimensional NMR experiment 12
8. An inversion-recovery pulse sequence for the determination of T_1 13
9. Refocussing magnetic isochromats to form a spin-echo 14
10. Processing a 2D NMR data set 15
11. The pulse sequence for the COSY experiment 16
12. The pulse sequence for the TOCSY experiment 18
13. Possible relaxation pathways in a homonuclear system 20
14. NOE intensity vs rotational correlation time 21
15. The pulse sequence for the NOESY experiment 22
16. The pulse sequence for the ROESY experiment 25

17. Maximum NOE intensity vs $\omega\tau_c$ for ROESY 26

18. A diagram of the transferred NOESY effect 28

19. Generalized Simulated Annealing Protocol 33

20. UV/VIS absorption spectrum of a washed rod outer segment membrane sample containing rhodopsin 40

21. Electrospray mass spectrometry spectrum of Ac-340-350(K341R) 42

22. Analytical HPLC trace of Ac-340-350(K341R) 43

23. Difference absorption spectra for a 15:1 peptide/rhodopsin mix after bleaching 49

24. Linear regression plot of a 15:1 peptide/rhodopsin mixture after bleaching 50

25. Initial decay rate constant ("k^{fast}") of peptide-MII complex vs peptide concentration 52

26. Initial decay rate constant ("k^{slow}") of peptide-MII complex at pH 6.5 . . 52

27. TOCSY spectrum (αH - NH region) of the free peptide Ac-340-350 (K341R) 54

28. NOESY spectrum (NH - αH and sidechain H) of the free peptide Ac-340-350 (K341R) 55

29. NOE build-up curves for the free peptide Ac-340-350 (K341R) 57

30. NOESY spectrum (NH - αH and sidechain H) of the peptide Ac-340-350 (K341R) and rhodopsin (dark) in a 15:1 molar ratio 62

31. NOE build-up curves for the free peptide Ac-340-350 (K341R) and a 15:1 mixture of peptide and rhodopsin (dark) 63

32. $R_{1\rho}$ vs log (ω_{SL}) for a 15:1 mixture of peptide and rhodopsin (dark) . . 66

33. NOESY spectrum (NH - αH and sidechain H) of the peptide Ac-340-350 (K341R) and metarhodopsin II (light) in a 15:1 molar ratio 69

34. New NOESY cross-peaks observed per amino acid for the peptide in both the dark-bound and light-bound forms. 71

35. NOE build-up curves for the free peptide Ac-340-350 (K341R) and a 15:1 mixture of peptide and metarhodopsin II (light) 72

36. NOE build-up curves for a 15:1 mixture of Ac-340-350 (K341R) and rhodopsin (dark) or metarhodopsin II (light) 73

37. $R_{1\rho}$ vs log (ω_{SL}) for a 15:1 mixture of peptide and metarhodopsin II (light) 75

38. A sample input file for a Discover minimization and dynamics run . . . 78

39. Superposition of the twenty dark-bound structures generated by a simulated annealing run 81

40. Superposition of five dark-bound structures (numbers 1, 3, 5, 9, 18) generated by a simulated annealing run 83

41. Superposition of two dark-bound structures (numbers 2, 20) generated by a simulated annealing run 85

42. Superposition of two dark-bound structures (numbers 6, 8) generated by a simulated annealing run 86

43. Superposition of two dark-bound structures (numbers 7, 14) generated by a simulated annealing run 87

44. Superposition of four dark-bound structures (numbers 4, 11, 16, 19) generated by a simulated annealing run 88

45. Superposition of one structure of each of the three groups of dark- bound structures after three rounds of MARDIGRAS and MD calculations . . 93

46. Superposition of the twenty light-bound structures generated by a simulated annealing run 95

47. Superposition of seven light-bound structures (numbers 1, 4, 6, 7, 10, 15, 19) generated by a simulated annealing run 96

48. Superposition of five light-bound structures (numbers 2, 8, 11, 13, 18) generated by a simulated annealing run 97

49. Superposition of three light-bound structures (numbers 5, 9, 17) generated by a simulated annealing run 98

50. Superposition of one structure of each of the four groups of light- bound structures after three rounds of MARDIGRAS and MD calculations . 102

51. TOCSY spectrum (quadrant 1) of the free peptide Ac-340-350 (K341R) 117

52. TOCSY spectrum (quadrant 4) of the free peptide Ac-340-350 (K341R) 118

53. NOESY spectrum (quadrant 1) of the free peptide Ac-340-350 (K341R) 119

54. NOESY spectrum (quadrant 3) of the free peptide Ac-340-350 (K341R) 120

55. NOESY spectrum (quadrant 4) of the free peptide Ac-340-350 (K341R) 121

56. NOESY spectrum (quadrant 1) of the peptide Ac-340-350 (K341R) and rhodopsin (dark) in a 15:1 molar ratio 122

57. NOESY spectrum (quadrant 3) of the peptide Ac-340-350 (K341R) and rhodopsin (dark) in a 15:1 molar ratio 123

58. NOESY spectrum (quadrant 4) of the peptide Ac-340-350 (K341R) and rhodopsin (dark) in a 15:1 molar ratio 124

59. NOESY spectrum (quadrant 1) of the peptide Ac-340-350 (K341R) and metarhodopsin II (light) in a 15:1 molar ratio 125

60. NOESY spectrum (quadrant 3) of the peptide Ac-340-350 (K341R) and metarhodopsin II (light) in a 15:1 molar ratio 126

61. NOESY spectrum (quadrant 4) of the peptide Ac-340-350 (K341R) and metarhodopsin II (light) in a 15:1 molar ratio 127

ABSTRACT

The goal of this research project is to investigate the three-dimensional structure of a specific peptide segment of the retinal rod G protein, transducin, bound to light excited rhodopsin. This segment has been shown to exhibit biological activity in much the same fashion as the full G protein. The segment studied consists of a modified portion of the C-terminus of the alpha subunit of transducin that runs from amino acid numbers 340 to 350. The peptide chain has been modified to prolong its biological activity by the addition of N-terminal acylation, and the substitution of a lysine for an arginine in the 341 position.

This project studied this peptide segment using two-dimensional nuclear magnetic resonance and computer refinement methods. The goal was to determine if the peptide has significant structure when free in solution, in the presence of bovine rhodopsin in an unactivated state, and finally bound to rhodopsin in its light excited form.

The NOESY build-up rates were somewhat similar for the dark- and light-bound experiments although significantly more cross-peaks were observed in the light-bound experiments. The new cross-peaks were mainly from sidechain interactions and interactions on the C-terminal end of the peptide. The sidechain cross-peaks suggest more intimate binding in the light, and the increase in C-terminal cross-peaks suggests that this end is important in the light binding. Measurement of the peptide-protein exchange rates shows fast exchange on the cross-relaxation time scale. The final structures obtained using iterative MARDIGRAS refinement are consistent with the idea of tighter binding in the light; the dark-bound structures qualitatively show less overall agreement with each other than the light-bound structures.

This project has yielded preliminary structures for the metarhodopsin II-bound peptide segment. Work continues in this laboratory to better define the dark- and light-bound structures and yield further understanding of this protein interface.

CHAPTER 1

BACKGROUND AND LITERATURE REVIEW

Introduction

How cells detect their environment, respond to it and communicate these responses to other areas of the cell or the entire organism are key research areas in biological chemistry today. There are a variety of routes through which this information is communicated - hormones, neurotransmitters, growth factors, and ion channels that are selectively activated. All of the routes involve a receptor that can specifically discriminate and respond to chemical signals from outside the cell. In many cases the receptors are not themselves ion channels or enzymes, but are coupled to specific enzymes to produce the desired cellular response. There are several superfamilies of receptors that appear to have very similar structures within each superfamily. The largest superfamily of receptors are coupled to amplifier proteins called guanine-nucleotide-binding-proteins, or G proteins, and are called G protein coupled receptors (GPCR).

Overview of G proteins

A review by Simon et al states that over 100 different G protein coupled receptors had been found in mammals by 1990(1). Current estimates are that there are nearly 900 different GPCR in all species including insects and fungi (98). A classic review by Gilman (2) in 1987 classifies and defines G proteins on the basis of their structure and functions. His functional definition of G proteins is that they act as intermediates in transmembrane signalling by means of receptor-induced GTP binding. The signalling pathway always consists of the sequence: Receptor → G protein → Effector. As a structural definition, G proteins discovered to date are either heterotrimers, consisting of α, β, and γ subunits or so-called "small G proteins"(1) which appear to be homologous to a section of the heterotrimer α subunit. These small G proteins regulate cell growth, protein secretion and intracellular vesicle interaction (3). This discussion will focus on the heterotrimeric G proteins, the class in which the G proteins involved in vision are found. Among the receptors for the heterotrimeric G proteins, virtually all are thought to have a heptahelical transmembrane structure. The heterotrimeric G proteins are thought to exist in two distinct states depending on the state of excitation of the receptor to which they are bound (1).

Currently, the α subunits are believed to be key differentiators between G proteins, whereas the β and γ subunits are more similar to one another. Among all

the known α subunits, 20 % of the amino acids are fully conserved (4) and the α subunits can be grouped into several different classes based on amino acid and functional similarities (Table 1; reference 1).

Table 1. G protein designations and functions.

α Subunit Designation	Function
G_s	stimulatory regulator of adenylyl cyclase
G_i	inhibitory regulator of adenylyl cyclase
G_q	stimulates phosphatidylinositol-specific phospholipase C
G_{12}	little currently known about function
G_t	stimulates cGMP phosphodiesterase

Features of the Gα subunits to be noted are in the NH_2 and COOH terminal regions. The NH_2 terminal region is believed to be involved in the interaction between the α and βγ subunits and the receptor; and the extreme C terminal region is thought to be involved with the recognition of specific receptors (1). A recent paper (5) changed three of the four C terminal residues in a $G\alpha_q$ sequence to match those of a $G\alpha_{i2}$ sequence and changed the receptor specificity to that of $G\alpha_{12}$.

The literature indicates that much less is known about the function and structure of the β and γ subunits. The review article by Simon et al (1) states that four distinct Gβ subunits have been found in mammals, with over 80 % of their amino acid sequences conserved. Tamir et al (6) investigated five different sources of

$G\beta\gamma$ and found only two highly conserved β forms. It is also postulated that the 30-40 initial amino acids on the NH_2 terminal end of the β subunit is responsible for the interaction with the γ subunit (1). As for the γ subunit, more diversity has been found here, with up to seven different $G\gamma$ sequences found (6). Tamir and co-workers hypothesize that the $G\beta$ subunits contain a common recognition site for various $G\alpha$ subunits, while the $G\gamma$ subunit is involved in receptor specificity.

In this research project the G protein involved is often referred to in the literature as transducin or G_t and is involved in the light activation of cGMP phosphodiesterase (PDE) in retinal rod outer segments (ROS). G_t is considered to be a distinct type of G_i protein by some researchers and it acts as an intermediate between the transmembrane rhodopsin and the enzyme PDE bound to the cytoplasmic surface of the membrane. Rhodopsin is able to function as a single photon detector in retinal rods by virtue of G_t, which acts as a pre-amplifier of the light signal and PDE which acts as a power amplifier for the output signal of the receptor cell via the cGMP cascade to be discussed further.

The Rhodopsin - G_t Interaction

The rhodopsin - G_t system has many advantageous features for study by modern biophysical techniques. A key advantage of the system is the availability and relative ease of isolation of the rhodopsin protein and G_t. Rhodopsin, along with its associated lipids, can be rather easily isolated from bovine retinas (7). Since the proteins in the rod outer segment are approximately 70% rhodopsin (8), it is relatively

easy to obtain rhodopsin in milligram amounts. Rhodopsin consists of two parts: the protein opsin and the small chromophore retinal, which is closely related to vitamin A(9, 10).

If ease of obtaining rhodopsin is one of the advantages of this system, a major complexity of this system is the photocycle of rhodopsin. Shown in Figure 1 is a diagram for the early events in the photocycle for rhodopsin, showing some of the major intermediates, structures and absorption maxima of the chromophore at each intermediate state (11). Several other intermediates have been described, including a metarhodopsin III (MIII) intermediate that can follow metarhodopsin II (MII) under appropriate temperature and pH conditions (12).

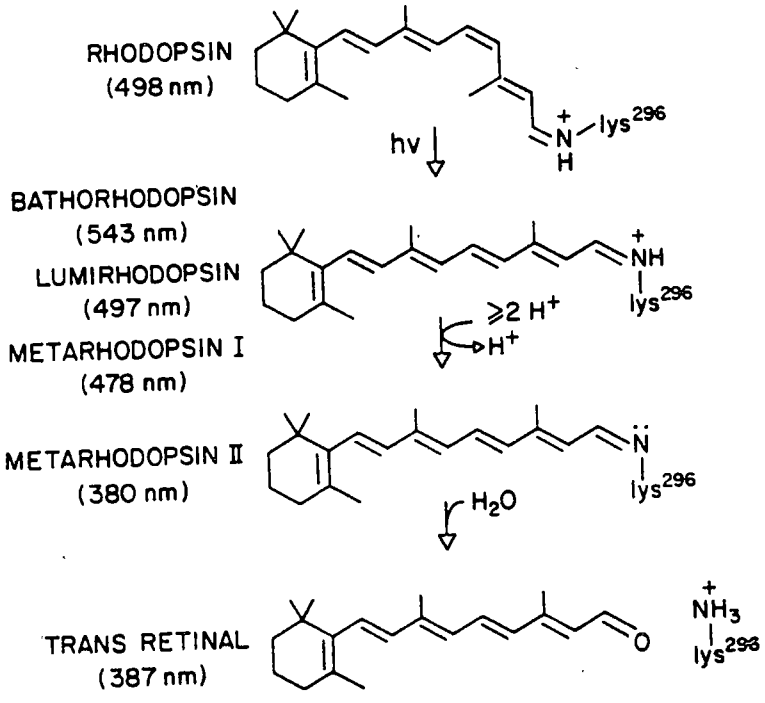


Figure 1. The rhodopsin photcycle. Shown are the changes in the chromophore structure and the absorption maximum of each intermediate. [Taken from Nathans (11)]

Another factor to be accounted for in the interaction of rhodopsin with the G protein is the physical structure of rhodopsin. Figure 2 gives a model of the rhodopsin protein within a rod outer segment, showing seven transmembrane helices that are thought to be present and a cut-away view of the approximate position of the chromophore within the protein (13).

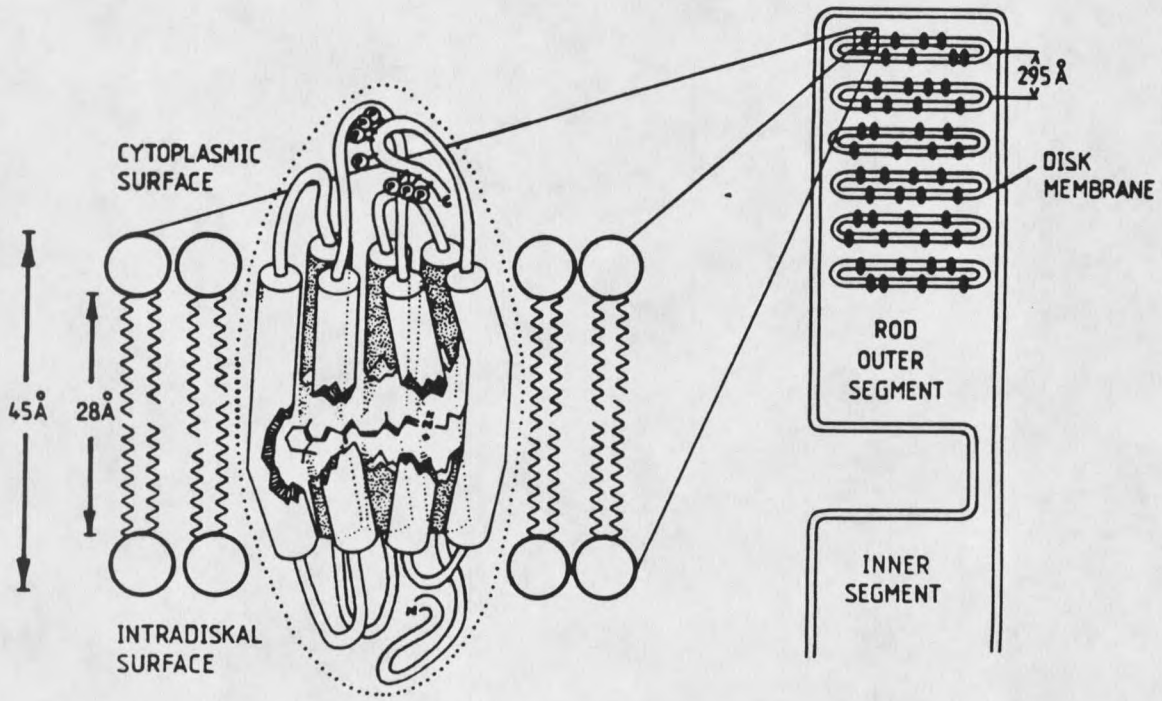


Figure 2. Cross-section of a rod outer segment. The drawing is not to scale. [Taken from Dratz and Hargrave (13)]

Figure 3 shows the primary sequence of bovine rhodopsin (13), and a model for the transmembrane topology, that is useful for further discussion of the interaction of rhodopsin with the G protein. The binding of photolyzed rhodopsin to a guanyl nucleotide binding protein with GTPase activity was first proposed by Fung and Stryer

(14), and is now generally accepted by researchers in this field (15). A diagram of a recent model for this binding is shown in Figure 4, and the complete cyclic GMP cascade that couples rhodopsin photolysis to an electrical response of the cell is shown in Figure 5.

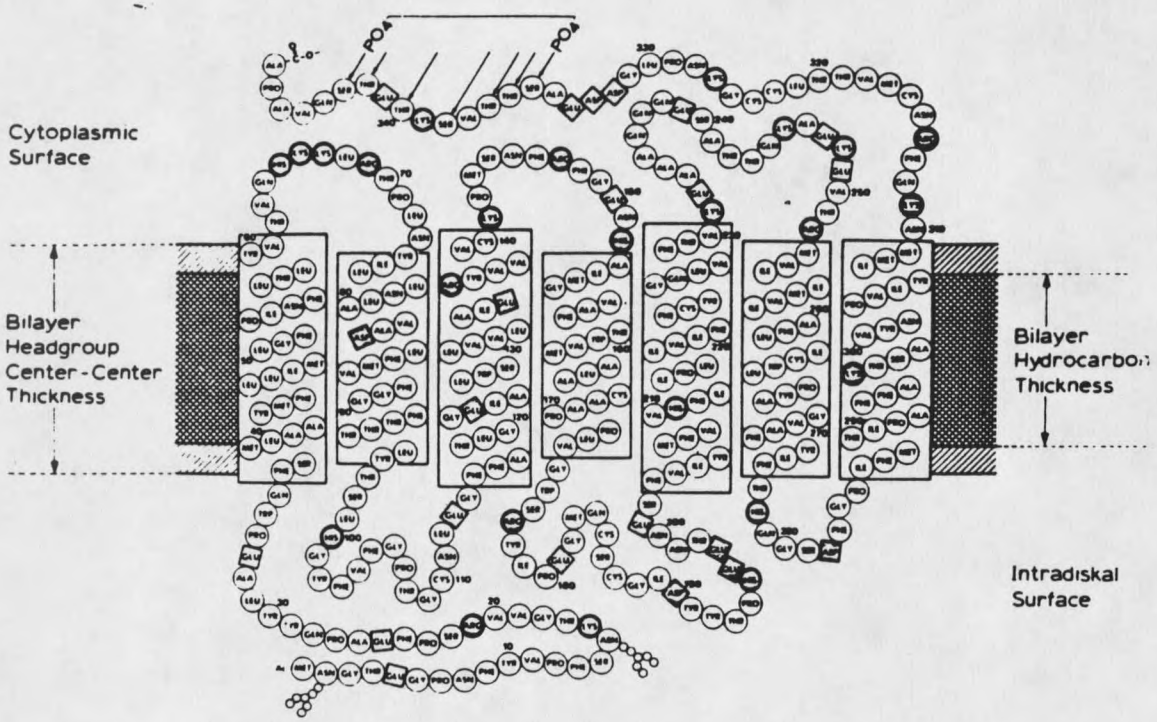


Figure 3. Primary sequence of the rhodopsin protein. [From Dratz and Hargrave (13)]

The photolysis intermediate of rhodopsin that interacts with the G protein has been shown in a variety of studies to be MII, which is equivalent to the activated state rho* (or R* shown in Figure 5) originally referred to by various researchers (16). It has also been noted that the G protein shows some binding affinity to phospholipid

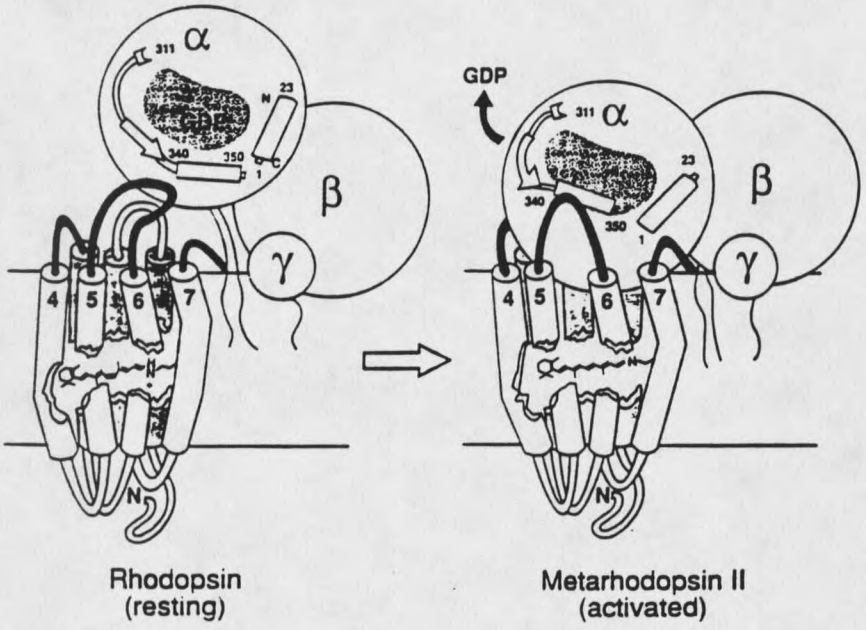


Figure 4. Proposed model of rhodopsin - G_t binding. [From Dratz et al (20)]

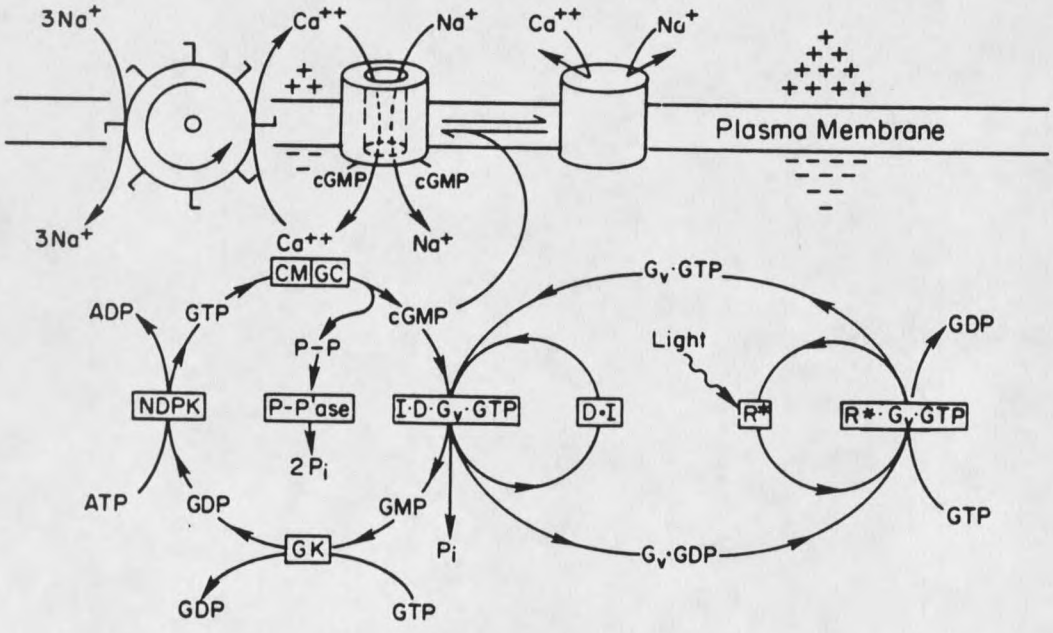
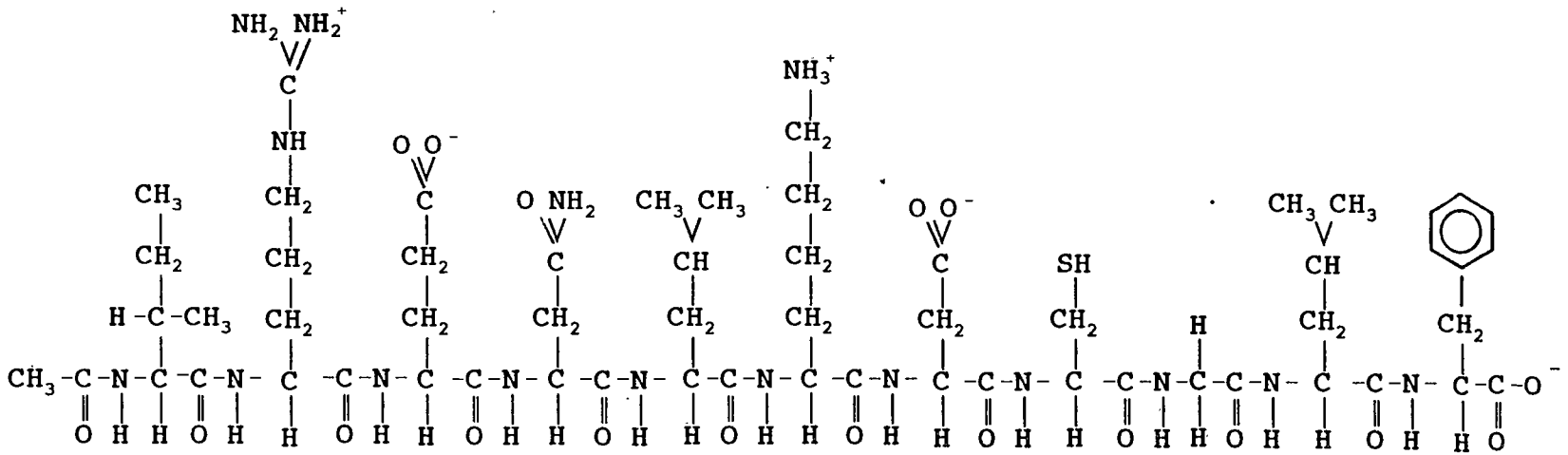


Figure 5. The cGMP model of activation in the vertebrate rod. [From Liebman et al (15)]

vesicles containing unactivated ("dark") rhodopsin (17), but not to pure phospholipid vesicles. Studies have also shown that MII binds to the α subunit of the G protein (18), but that the overall activity of the cyclic GMP cascade is dependent on all three subunits of the G protein (17).

Three of the cytoplasmic loops of rhodopsin (peptide segments 141-153, 230-252, and 310-321) appear to be sites that interact with the G protein (19). The specific areas of the G protein that interact with MII have been mapped by peptide competition with formation of MII-G protein complex (7). These areas are segments of the α portion of the G protein trimer and consist of peptide segments 1-23, 311-329, and 340-350, with the 340-350 segment being the most effective for the stabilization of MII (7). Further work (20) has shown a modified version of the 340-350 segment, where the N-terminal has been acylated and the lysine at residue 341 replaced with an arginine, provides a more persistent stabilization of MII than the native 340-350. Amino groups are able to non-specifically inactivate MII and the N-acylation and K341R "mutations" remove two amino groups from the peptide without compromising the initial stabilization of MII. The N-Ac-340-350 (K341R) segment was therefore selected for the initial conformational studies of the binding site on the rhodopsin MII intermediate, and the primary sequence of this peptide is shown in Figure 6. Since this region consists of only eleven amino acids, it is a favorable candidate as well for study by NMR techniques, which will be discussed in the following sections.



Ac-Ile-Arg-Glu-Asn-Leu-Lys-Asp-Cys-Gly-Leu-Phe

Figure 6. The primary sequence of the modified $G_t\alpha$ peptide Ac-340-350 (K341R).

Relevant NMR Theory

NMR techniques have emerged as powerful tools for studying the three dimensional structure of peptides and small proteins under conditions similar to their physiological states (see references 21 - 24 for some excellent review articles). In this section, the relevant fundamental theory of NMR will be presented, along with the theory and application of the NMR experiments that were used in this research.

The One-Dimensional NMR Experiment

Numerous articles and books have been written on the principles of NMR (23 - 31). Complete presentations of the detailed fundamental theory of NMR are quite complicated and most generally involve product operator (23) or density matrix (26) formalism. However, the 1D experiment is relatively easy to picture. A sample is placed in a static magnetic field (conventionally referred to as $\mathbf{B}_0$). We will discuss nuclei with a spin of 1/2 (e.g. ^{1}H, ^{13}C, ^{15}N, or ^{31}P) which align parallel or antiparallel with the magnetic field according to the Boltzmann distribution. These two states are generally referred to as α and β, with the α state usually chosen to be the lower energy level of the two. A short radiofrequency (rf) pulse is applied to the system along the x axis (B_1), which flips the spins into the y axis (z being defined as the direction of $\mathbf{B}_0$). This magnetization will then precess about the z axis in the xy plane and eventually relax back along the z axis. How fast the magnetization precesses and relaxes depends on the chemical and motional environment of the spins involved, and

is detected in the form of a free induction decay (FID) in the xy plane after the pulse. The FID can be Fourier transformed so that a spectrum in the frequency, rather than time, domain is obtained. A vector representation of this process is given in Figure 7. What is actually being detected is the difference in the rate of precession of the spins relative to that of a carrier frequency, so the resulting spectrum is often labeled in terms of the difference in these two frequencies, or in terms of the chemical shift from the resonance frequency of some reference compound. For protons, the full chemical shift range is generally only on the order of ten parts per million (10 ppm) for organic compounds.

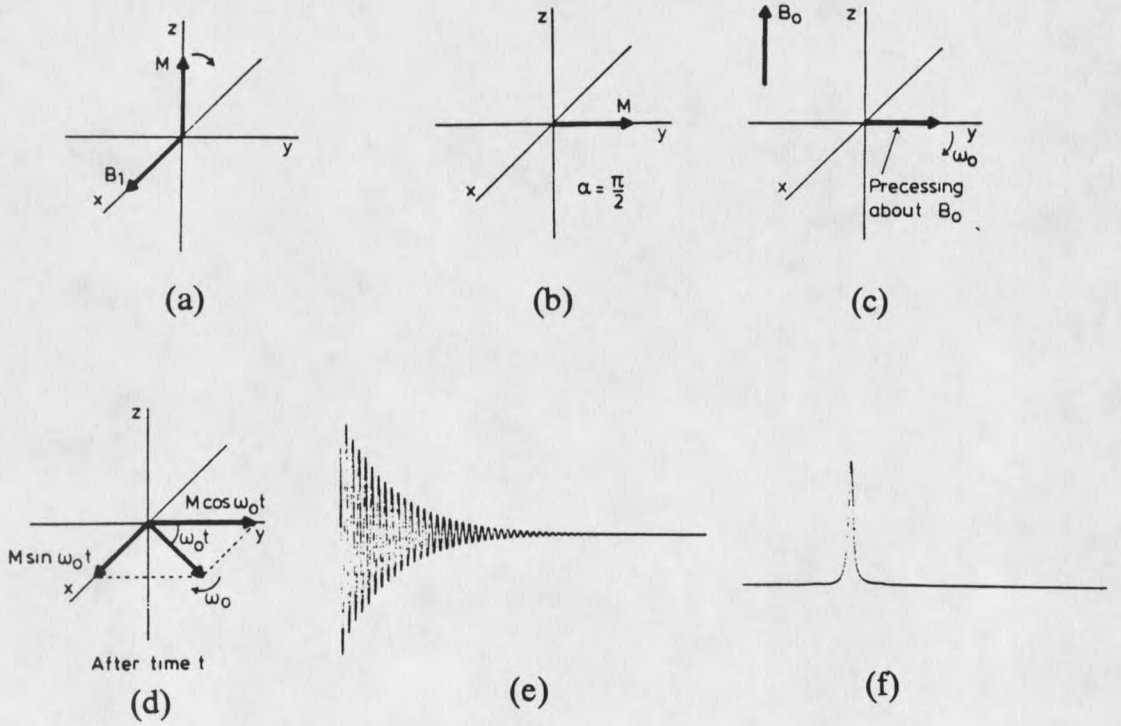


Figure 7. The one-dimensional NMR experiment. (a) Net sample magnetization (**M**) and rf pulse direction ($\mathbf{B}_1$). (b) Effect of a 90° pulse along x. (c) and (d) After the pulse, magnetization begins to precess in the *xy* plane. (e) FID detected relative to carrier frequency. (f) Result of a Fourier transform on the FID. [From Derome (28)]

Relaxation Experiments

In NMR, there are two primary relaxation pathways of concern: longitudinal and transverse relaxation. Longitudinal, or spin-lattice, relaxation is commonly referred to by the value of its time constant, T_1. To quote Derome (28): "any time the magnetization is moved away from the z axis, we assume that in the absence of external influences it will return there exponentially with time constant T_1." For a sample with multiple protons, there can be numerous values of T_1 due to the different environments that the protons experience. Experimentally, the longest T_1 in the molecule is usually the one of most interest, since most multi-pulse experiments contain a delay of two to five times the value of T_1 to allow for relaxation of the protons before the pulse sequence is recycled. T_1 values can be measured by an inversion-recovery experiment, such as that diagrammed in Figure 8. T_1 values are determined by a graphical procedure, plotting a function of the signal intensities vs the variable relaxation delay τ.

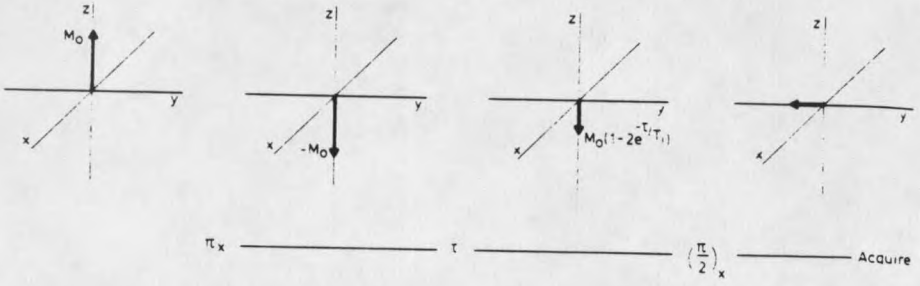


Figure 8. An inversion-recovery pulse sequence for the determination of T_1. [From Derome (28)]

Transverse, or spin-spin, relaxation is a result of magnetization in the xy plane gradually "fanning out" as a result of varying precession frequencies of magnetization within the molecule. Each frequency component is known as an isochromat. The collective amplitude of the isochromats can be refocussed and a spin-echo formed, which can be used to determine the rate of transverse, or T_2 , relaxation. One method of forming a spin-echo is shown in Figure 9. T_2 is measured experimentally with some difficulty, since the B_1 fields are not totally homogeneous over the sample volume. The Carr-Purcell-Meiboom-Gill (CPMG) pulse sequence uses a series of pulses along both the x and y axes and suitable delays to overcome both B_1 inhomogeneity and 180° pulse inaccuracy and to thereby more accurately refocus the spin-echo. For liquid-state samples, where motion is fast, T_1 and T_2 are approximately equal, and have precisely the same value if motion is fast enough.

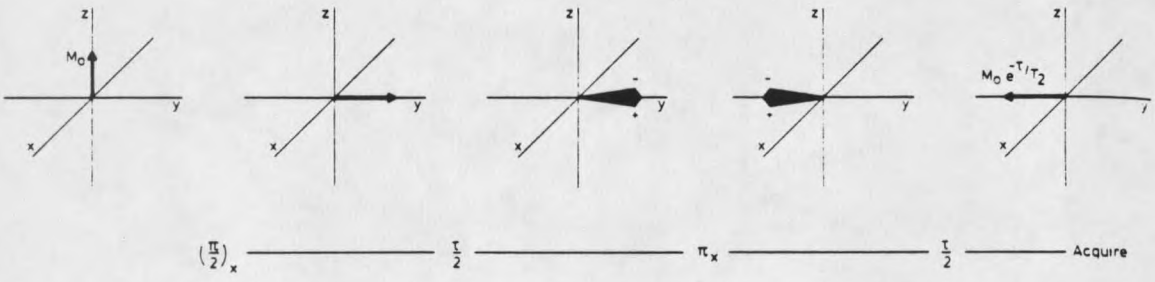


Figure 9. Refocussing magnetic isochromats to form a spin-echo. [From Derome(28)]

There are other pathways for the relaxation of magnetization. Dipole-dipole interactions that give rise to the NOE effect will be discussed where appropriate in later sections of this chapter.

The Two-Dimensional NMR Experiments

Two-dimensional NMR was first proposed by Jeener in 1971 and later expanded upon by Ernst (26). The second acquisition dimension in an NMR experiment is a second time dimension. In general, a 2D experiment can be thought of as existing in the following parts (26):

preparation - evolution (t_1) - mixing - detection (t_2)

In the 2D experiment, the detection time t_2 is just as it is for a 1D experiment and the FT of the signal in this direction provides the so-called ω_2 axis of the spectrum. The evolution time, t_1, is incremented in small steps and a second FT is performed in the t_1 direction to obtain the ω_1 axis. This process is shown graphically in Figure 10.

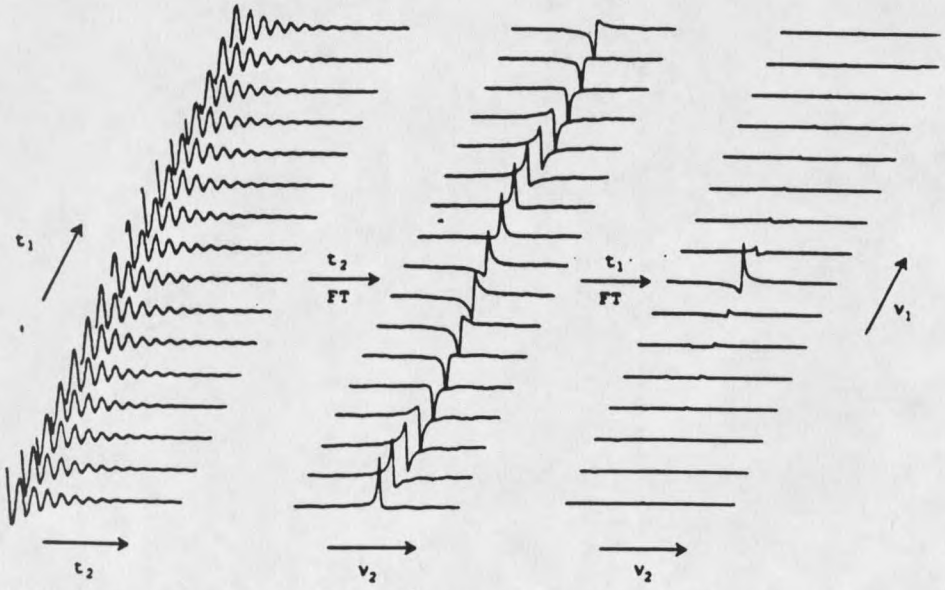


Figure 10. Processing a 2D NMR data set. [Taken from Wemmer (32).]

The mixing time allows spins to interact with each other via scalar coupling or dipolar interactions. How the system is treated during this mixing time generally distinguishes one NMR experiment from another. 2D NMR experiments fall into two broad classes that rely on through bond J (scalar) coupling or through space dipolar interactions, with homonuclear and heteronuclear experiments possible in each class. The following discussions will first focus on two experiments that rely on scalar couplings (COSY and TOCSY), and then on three experiments that focus on through-space dipolar interactions (NOESY, ROESY, and transfer-NOESY).

The Two-Dimensional Scalar Coupling Experiments: Through-Bond Correlations

The COSY (**CO**rrelated Spectroscop**Y**) experiment shows couplings between neighboring protons, allows determination of the protons that are responsible for couplings, and aids in the assignment of the peaks to chemical structures. The basic pulse sequence for a COSY experiment is shown in Figure 11.

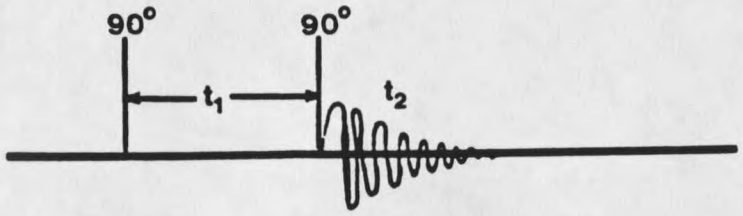


Figure 11. The pulse sequence for the COSY experiment.

The first 90° pulse provides the excitation magnetization, which evolves during the period t_1. The second 90° pulse has two effects: first, it records the various magnetization components present at that instant and creates frequency labelling of the

amplitude of the different frequency components. The second 90° pulse also mixes the components of the transverse magnetization and causes coherence transfer between coupled spins. To illustrate this with a simple AX spin system, if A and X are coupled, the magnetization on spin A precessing with frequency υ_A is partially transferred to υ_X by the second 90° pulse. This magnetization then continues to precess with frequency υ_X during the detection period. This transfer of magnetization gives rise to the off-diagonal cross-peaks observed in COSY (33). To quote Gray (in ref. 29):

> The existence of the off-diagonal intensity is proof of spin coupling between the proton at the shift value present in t_1 and the proton at the detected shift value.

An empirical rule for assigning standard COSY spectra is that cross-peaks are generally observed only between protons separated by three or fewer covalent bonds (27). This "short range" is an advantage since it allows starting with an easily identified spectral peak (e.g. the aromatic peaks of a phenylalanine residue or the terminal CH_3 group on a residue such as valine) and working back step-wise by way of 2D cross-peaks to assign many of the peaks in simpler 1-D spectra. The assignment process in the case of peptides is assisted by the use of tables giving the observed shifts of protons in amino acids in random coils (27). The COSY experiment is limited, however, since the peaks occur in antiphase pairs limiting resolution and there is often overlap of cross-peaks in various regions of the spectrum. It is often not possible to work through the couplings of each proton within a residue by COSY alone. An alternative experiment to COSY that provides longer range

coupling information is the homonuclear Hartmann-Hahn (HOHAHA) (34) or total correlation spectroscopy experiment (TOCSY) (35). This experiment can, in theory, reveal the entire spin system of each amino acid residue in one experiment by showing all spin correlations, not just those between protons separated by three or fewer bonds. The TOCSY experiment can also be set up so that the resulting spectrum gives all cross-peaks with positive intensity and a pure absorption mode (35) rather than in COSY where each peak occurs in positive and negative intensity pairs with phase-twist line shapes (26). The pulse sequence for TOCSY is given in Figure 12. Note that the single detection pulse of the COSY experiment has been replaced with a spin-lock. The spin-lock is created with a set of short pulses to minimize sample heating. The most common spin-lock pulses for TOCSY is the MLEV-17 (34) series. During the time of the spin-lock, magnetization can flow between protons at a rate determined by their J coupling (24) so that all correlations in a system are obtained.

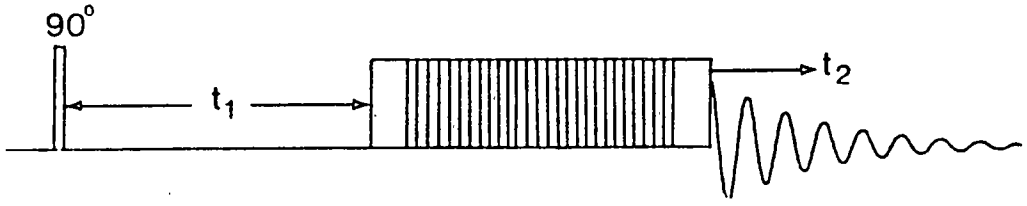


Figure 12. The pulse sequence for the TOCSY experiment.

The Two-Dimensional Dipolar Relaxation Experiments: Through-Space Interactions

Two NMR experiments are extremely useful in detecting nearest neighbor relationships to finalize peak assignments. The first of these, 2-D Nuclear Overhauser

and Exchange SpectroscopY (NOESY), uses a phenomenon known as the nuclear Overhauser effect (NOE) to determine the proximity of pairs of protons through space. Before discussing NOESY, and the related ROESY experiment, a short discussion of the nuclear Overhauser effect is in order.

To quote from Derome (28): "the NOE is a change in the intensity of an NMR resonance when the transitions of another one are perturbed". In the original continuous wave or pulsed FT observation of the NOE, the perturbation used was saturation of one signal while changes in intensity of the signals of other nuclei were observed. This technique provides a way to get information about the existence of "through space" dipolar couplings in a molecule, which in turn can be related to internuclear distances and molecular motions. When we speak of "saturation", this means that the population differences across one or more transitions are eliminated. This leads to another interpretation of the NOE as being:

> ...an attempt of the total system to stay at thermal equilibrium; we have forcibly changed the population differences of part of it, so other parts change in compensation (28).

To fully understand NOE's, it is necessary to examine the relaxation pathways available to nuclear spins in the molecule. In addition to the dipole-dipole interaction, which gives rise to the NOE signal, spin-lattice relaxation mechanisms discharge magnetization in competition with the NOE pathways. The energy levels of the simplest two-spin system that can exhibit NOE and the different possible relaxation pathways between these levels are diagrammed in Figure 13.

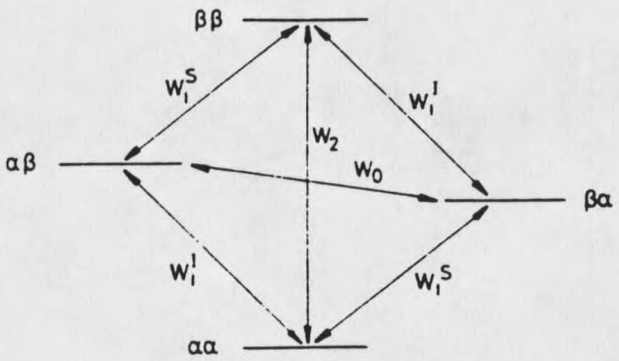


Figure 13. Possible relaxation pathways in a homonuclear system. [From Derome(28)]

Spin-lattice interactions occur between the excited spins and other protons in the molecule, the solvent or paramagnetic species in solution (29). The complete treatment of these competing relaxation pathways can take entire chapters, and entire books (36) dedicated to the subject! For this discussion, let us note that saturation of the S transitions equalizes the populations of the levels connected by the S transitions. The W_2 double quantum transition increases the population difference and the intensity of the I transitions to $+1/2 + \delta/2$ (positive NOE), where δ is the population difference caused by W_2. The W_0 zero quantum transition decreases the population difference and the intensity of the I transitions to $+1/2 - \delta/2$ (negative NOE), where δ is the population change caused by the W_0 transition. Fast motions provide fluctuations with frequency twice the resonance frequency ($\omega_I + \omega_S \approx 2\omega_0$) that favor W_2 transitions, while slow motions provide fluctuations with low frequencies ($\omega_I - \omega_S$) that favor the W_0 transition. At a motional frequency near the Larmor frequency (ω_0), the W_0 and

W_2 effects cancel and the NOE is zero. For protons with slow motions the NOE is negative (maximum value = -1) and for fast motions the proton NOE is positive (maximum value = +1/2) as shown in Figure 14. The NOE signal observed from spin I when spin S is saturated, $\eta_I(S)$, is proportional to $1/r^6$ (where r=internuclear distance) (28):

$$\eta_{I(S)} \propto (\tau_c / \rho^*)(1/r^6)$$

where τ_c is the rotational correlation time of the molecule and ρ^* is the nuclear relaxation from mechanisms other than I-S cross-relaxation. Figure 14 shows the relationship between NOE intensity and rotational correlation time of the molecule for different nuclei.

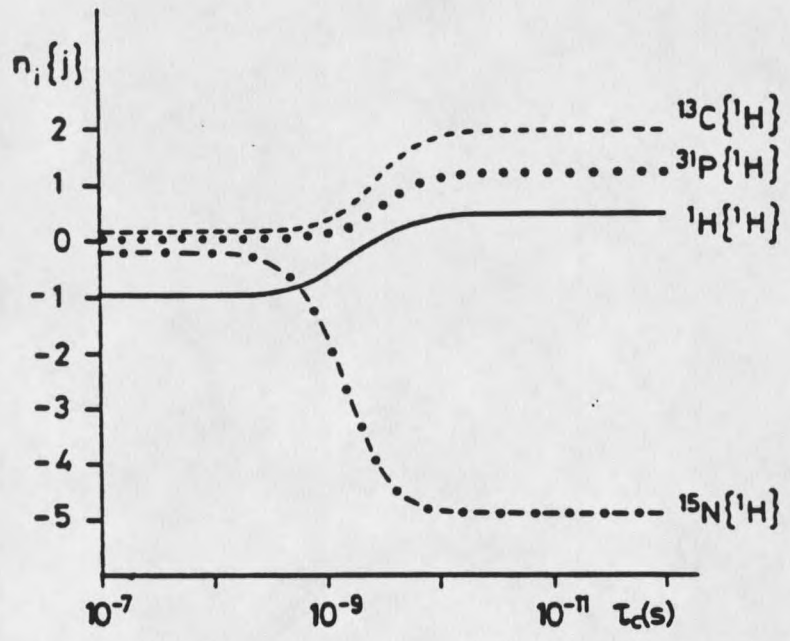


Figure 14. NOE intensity vs. rotational correlation time. [From Wüthrich (27)]

As we have noted in the discussion of the 1D NOE experiment, a particular transition is saturated and then the changes in intensities of the remaining transitions are measured. This is most commonly done by difference spectroscopy, where the spectrum with no transitions saturated is subtracted from a spectrum where a particular transition has been saturated and the resulting intensity changes are measured. Obviously, if there are many peaks in the 1D spectrum, the process of saturating each peak, obtaining a difference spectrum and measuring intensities will be a time-consuming process, and if peaks are overlapping it is difficult to saturate with sufficient selectivity. The NOESY experiment uses inversion rather than saturation and provides a systematic way to observe all possible NOEs with optimum resolution. The pulse sequence required is shown in Figure 15.

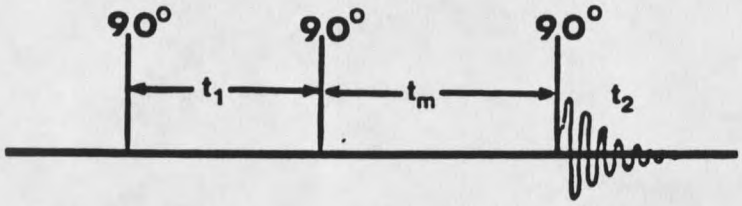


Figure 15. The pulse sequence for the NOESY experiment.

As in the COSY experiment, the first two 90° pulses, separated by a variable evolution time labels and modulates the amplitudes of the different nuclei by their relative chemical shifts. The second 90° pulse generates non-equilibrium spin components inverted along the -z axis where they are not affected by transverse (T_2) relaxation. The -z components are allowed to modulate each other's amplitude by

NOE cross-relaxation during the t_m (τ_{mix}) time. The amplitude cross modulation by cross-relaxation during t_m leads to off-diagonal cross-peaks analogous to the 1D NOE experiment. By going through a regularly incremented series of evolution times (e.g. incrementing t_1), each spin has an amplitude modulated nonequilibrium population distribution with a frequency equal to the offset from the carrier. Therefore all possible population transfers will occur. The amplitude of the magnetization transfer that has occurred is sampled by the third 90° pulse, which is followed by the usual t_2 detection. When the cross-modulation of transverse magnetization observed has come from dipolar relaxation between two spins during t_{mix} an off-diagonal NOESY signal is observed. Note that this pulse sequence also detects chemical exchange, but Hull states (in reference 29) that for small molecules chemical exchange and NOE effects have opposite signs, so the NOESY experiment does distinguish between these two effects if performed in a phase-sensitive mode. Later where transferred NOESY is discussed, the case of interest is fast exchange where the two states for each nucleus have a single resonance frequency. Under this condition, the NOESY does not detect chemical exchange directly because separate peaks are needed to see exchange peaks between them.

There is one potentially major complication with the NOESY experiment, however. Depending on molecular size, tumbling rates and the applied field, NOE's can be observed as either positive or negative peaks. Abraham et al (30) make the generalization that small molecules display positive NOE's and that large molecules display negative NOE's. This leads to the obvious questions of what is "small",

"large", and what about a molecule that is "intermediate" in size? The NMR parameters that govern this behavior are ω (the angular Larmor frequency) and the τ_c (the rotational correlation time of the molecule). If the product $\omega\tau_c$ is approximately equal to 1, the observable NOE signal is zero, as seen previously (Figure 14). Berstein (in ref 29) refers to this condition as "somewhat rare", but it is important to note that $\omega\tau_c \approx 1$ corresponds to molecules with molecular weight of 1000-2000 - the size range of many peptides of interest. Fortunately, the CAMELSPIN or ROESY experiment has been developed to overcome this intermediate molecular weight problem. The original experiment reported for detecting NOE's on these intermediate size molecules was called CAMELSPIN (**C**ross-relaxation **A**ppropriate for **M**inimolecules **E**mulated by **L**ocked **SPIN**s) (37), but is now more commonly referred to as ROESY (**R**otating-frame **O**verhauser **E**nhancement **S**pectrosco**Y**) (38) to make the connection that this is related to a NOE experiment.

In the ROESY experiment, the magnetization transfer is performed using spin-locking in the rotating reference frame. In the laboratory frame, we can envision the sample in a static magnetic field, B_0, and a radiofrequency field, B_1. This combination of fields, along with the precession of the nuclei makes for a conceptually complicated system. The rotating reference frame simplifies this by setting a coordinate system that rotates at the nuclear precession frequency instead of the laboratory Cartesian coordinate system (28). The pulse scheme for ROESY is shown in Figure 16. This pulse sequence serves to give rotating frame NOE's that are always positive and which increase in magnitude for increasing τ_c (38). The theory behind why the rotating

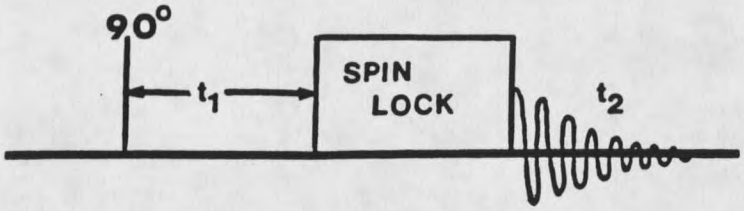


Figure 16. The pulse sequence for the ROESY experiment.

frame enables observation of NOE's for these molecules is quite complicated for a multi-spin system, but can be more easily explained for a simple two-spin system. With spin-locking in the rotating frame, the spins precess around the spin-lock field. So molecular motions, which are of the order of the resonance frequency ($\approx 5 \times 10^8$ sec^{-1}) for intermediate sized molecules, are very fast relative to the spin-lock frequencies ($\approx 5 \times 10^3$ sec^{-1}) and so positive ROEs result. In the original CAMELSPIN paper by Bothner-By (37), it is shown that for a two-spin system the maximum NOE signal in the rotating frame is given by:

$$\eta_{max} = -\frac{(\rho_2+\sigma_2)}{(\rho_2-\sigma_2)}^{-(\rho_2+\sigma_2)/2\sigma_2} + \frac{(\rho_2+\sigma_2)}{(\rho_2-\sigma_2)}^{-(\rho_2-\sigma_2)/2\sigma_2}$$

In this expression, ρ_2 and σ_2 are the autorelaxation and cross-relaxation rate constants respectively of spin 2 when spin 1 is saturated. Additionally, expressions for ρ_2 and σ_2 can be given in terms of $\omega\tau_c$, and the graph of η_{max} vs $\omega\tau_c$ (Figure 17) shows that the ROE intensity is always positive for the two-spin case (37). This will allow determination of ROE intensities even if the tumbling rate of the peptides of interest fall in the range that has near zero NOE intensity in the laboratory frame.

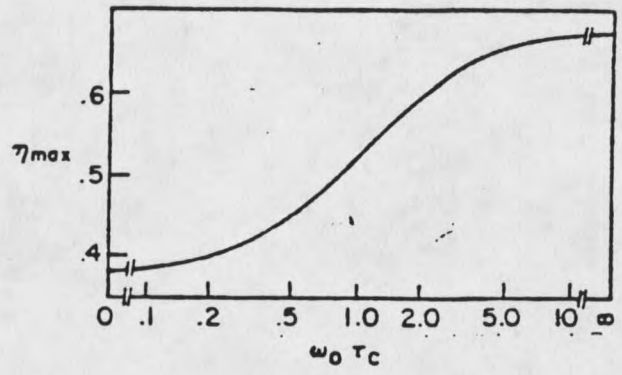


Figure 17. Maximum NOE intensity vs $\omega\tau_c$ for ROESY. [From Bothner-By (37)]

Investigating the Bound Structure: The Transferred NOESY Experiment

The principle NMR experiment employed in this project is transferred NOESY (TRNOE or TRNOESY). This experiment was chosen to allow us to obtain information about the 3D structure of the peptide when bound to its receptor.

The TRNOE experiment was first proposed over 20 years ago, also by Bothner-By's group (39, 40), to determine the structure of a protein bound ligand. Since then, numerous papers have been published to explore the theory behind this effect (41 - 44) and an excellent review of both theoretical and practical aspects was recently published (31). A brief qualitative perspective on the transferred NOESY experiment follows.

From an NMR standpoint, this experiment uses exactly the same pulse sequence as a NOESY experiment, only the sample now contains both the peptide or ligand of interest and its specific receptor. The TRNOE effect relies on the differing correlation times (τ_c) of the peptide in its free and bound states. In the free state, the peptide has a short correlation time (typically $\tau_c \leq 10^{-10}$ s) and displays NOE's that are

small and positive, approaching zero (41), or slightly negative depending on the details of the peptide and experimental conditions. When bound to the protein, the peptide experiences the long correlation time of the protein ($\tau_c > 10^{-8}$ s) which gives it large, negative NOE values (44) due to the more efficient cross-relaxation between protons in the bound form of the peptide. The basis of TRNOE is that when there is rapid chemical exchange between the free and bound forms of a ligand, information can be obtained concerning the bound conformation of the ligand (41) since the loss of the cross-relaxation information obtained in the bound state is quite slow in the free state. The NMR measurement of the free peptide signal is possible since these lines are very much narrower than those of the bound peptide, and through chemical exchange, the free peptide retains the spin population information of the bound state for times comparable to the T_1 of the free peptide. This can be seen by considering the binding reaction:

$$P + R \underset{k_{-1}}{\overset{k_1}{\leftrightharpoons}} PR$$

where P is the peptide, R is the receptor and PR is the peptide-receptor complex. If P is in excess, $k_1[R]$ can be rewritten as a pseudo-first order rate constant k_1'. As long as the peptide's exchange rate with the receptor, $k_{-1} + k_1'$, is substantially faster than the total spin-lattice relaxation rate (T_1) of the nuclei, a TRNOE signal can be observed. As long as $k_{-1} + k_1'$ is $\geq$ 10 times faster than the maximum cross-relaxation rate the TRNOE is most straightforward to interpret. This process is depicted schematically in Figure 18, and a discussion of the kinetics of the peptide-receptor exchange follows. A detailed theoretical evaluation of the TRNOE effect using the

full relaxation-matrix is given by Landy and Rao (43). Campbell and Sykes utilize the Landy and Rao treatment, and have developed a computer program to simulate TRNOE build-up curves for peptides under a full relaxation-matrix treatment including relaxation sink processes from the receptor (44).

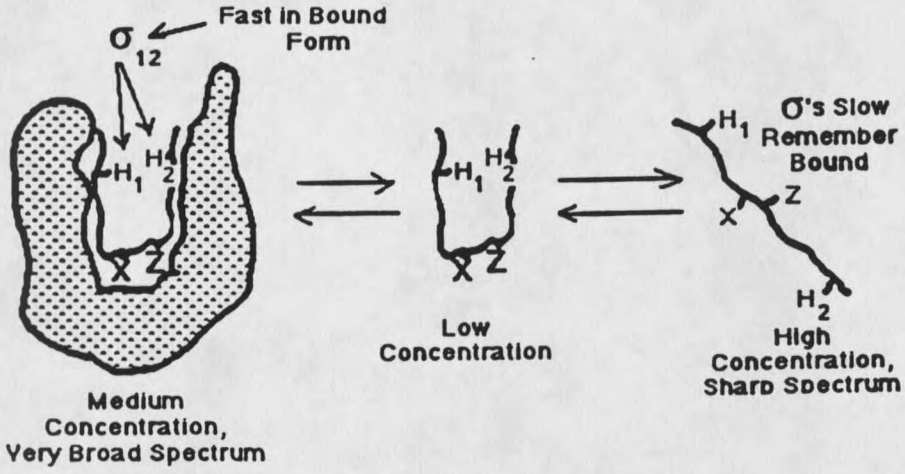


Figure 18. A diagram of the transferred NOESY effect.

Kinetics of the Peptide-Receptor Exchange In order to confidently interpret the results of the TRNOESY, it must be known if the peptide is in fast, slow, or intermediate exchange with the receptor (41, 42, 48, 49). The NOEs observed can be interpreted as a simple function of both the free and bound peptide cross-relaxation rates only if the peptide is in fast exchange. If fast exchange is present, the relationship that applies is:

$$\sigma_{ij}^{obs} = p_f\sigma_{ij}^{f} + p_b\sigma_{ij}^{b}$$

where σ_{ij}^{obs}, σ_{ij}^{f}, and σ_{ij}^{b} are the observed, free, and bound cross-relaxation rates respectively, and p_f and p_b are the mole fractions of free and bound peptide (45). In

many cases, where the free peptide has small NOEs, even if there is a large excess of free peptide (as is generally the case), $p^f\sigma_{ij}^f \ll p_b\sigma_{ij}^b$ and the resulting NOE observed is dominated by the bound-state NOE. Analysis of the data is also simplified if k_{-1} (the peptide off-rate) is > 10 times the largest bound cross-relaxation rate (i.e. the peptide is in fast exchange) with respect to cross-relaxation.

Recent work by Davis, London and coworkers (45) has demonstrated a means for measurement of k_{-1} based on the dependence of the $T_{1\rho}$ relaxation rate on the strength of the applied spin-lock field. $T_{1\rho}$ is the time for relaxation of magnetization that is parallel to a spin-lock field, but not necessarily in the transverse plane of the static field. They have shown that the relaxation rate $R_{1\rho}$ ($R_{1\rho} = 1/T_{1\rho}$) when plotted versus the spin-lock power can be fit by the following equation:

$$R_{1\rho}^{ex}(\omega_{SL}) = p_f[\cos^2(\beta_f)/T_1^f + \sin^2(\beta_f)/T_2^f] + p_b[\cos^2(\beta_b)/T_1^b + \sin^2(\beta_b)/T_2^b] + p_f p_b \sin^2(\beta)\Delta\omega^2[k_{ex}/(k_{ex}^2 + \omega_{SL}^2)]$$

Several terms in this equation are familiar, while others are not. The β terms refer to the angle between the effective field (spin-lock and offset fields) and the static field, $\Delta\omega$ is the chemical shift difference between the free and bound resonance of interest, and $k_{ex} = k_{-1}p_f$. The measurements of T_1^f and T_2^f are straight-forward, and T_1^b and T_2^b must be calculated from experimental data. Since the observed T_1 and T_2 in the presence of the receptor will contain a great deal of free peptide, a true value for the bound state relaxation parameters must be calculated. London et al (45) provides a relationship:

$$\frac{1}{T_1^{obs}} = \frac{p_f}{T_1^f} + \frac{p_b}{T_1^b}$$

with an analogous equation for T_2. Experimentally determined values of p_f, p_b, T_1^f, T_2^f, T_1^b, and T_2^b can then be put into a fitting program, along with experimental values of $R_{1\rho}$ and ω_{SL} and the k_{ex} and $\Delta\omega$ parameters are varied to best fit the calculated data to the experimental values. Additional theory on the relationship of the off-rate and other kinetic factors can be found in publications by London and coworkers (46, 47) and by Hallenga and co-workers (48, 49).

Computer Methods

In the course of this research, several computer programs were employed to aid in the refinement of the structure initially obtained from the simplest interpretation of the NMR data. These methods are described briefly in the following sections and further details are given in the discussion in chapter 5.

Energy Minimization

In a molecular energy minimization, an equation describing the energy of a system as a function of its nuclear coordinates is defined and evaluated for a given conformation. The gradient (slope) of the energy as a function of distortion of the coordinates is calculated and the conformation is adjusted to move downhill on the energy gradient to lower the value of the energy expression (50). A forcefield is used to model the potential energy surface of the molecule as a function of distortions of the coordinates of the molecule. Specific energy minimization routines that will be used in this project are the methods of steepest descents and conjugate gradients.

In a steepest descents energy minimization the position of the search on the potential energy surface is updated whenever the trial point has lower energy. This is considered to be a fairly "robust" method of minimization, used when structures are far from their global energy minimum.

In a conjugate gradients minimization, each point in the minimization produces "a complete basis set of mutually conjugate directions" (50), which allows a quicker convergence to the minimum, without the oscillations that are normally a part of a steepest descents procedure. Minimizations are mathematically considered to be converged when the derivatives of the function are zero and the second derivative matrix is positive definite. Practically, a minimization is considered to have converged when the root-mean-square (RMS) values for the atomic derivatives have reached some arbitrarily defined small criterion value. This value can range from 1.0 kcal$\circ$ $mol^{-1}\circ Å^{-1}$ for a molecule that will undergo further molecular dynamics analysis, to 0.02 $kcal\circ mol^{-1}\circ Å^{-1}$ or less for a well-minimized final structure of a protein or polypeptide(50).

Molecular Dynamics

In a molecular dynamics simulation, the program solves the equations of motion for a system of atoms. These solutions model the time-dependence of the molecular motions, and also allow the molecule to cross energy maxima so that the conformational energy space can be explored (50). In a dynamics run, the temperature of a system is held constant by modelling the system as being in equilibrium with a constant temperature heat bath. This allows molecules to fluctuate energetically and

conformationally using thermal energy to cross energy barriers. Molecular dynamics, therefore, is less likely than molecular minimization to lead to a molecular conformation that is trapped in a local, rather than the global, energy minimum. Two review papers (51, 52) on the use of molecular dynamics and its applications to biochemical models are suggested for further reading.

Simulated Annealing

Simulated annealing can be described as "a protocol for finding low energy structures by mimicking the natural processes of heating and cooling." (50) There are several different ways that simulated annealing is carried out. The protocol used in this project first greatly reduced the repulsive force constants in the molecular potential functions, and then gradually increased the force constants to their full values followed by thermal cooling and energy minimization (53, 54). Figure 19 shows a flow-chart for the simulated annealing protocol that was followed in this work.

MARDIGRAS Structure Refinement

To a first approximation, the intensities of NOE cross-peaks can be related to $1/r_{ij}^6$, where r_{ij} is the distance between the two protons involved (see discussion, page 21). The approximation that treats the two protons as an isolated spin system is known as the isolated spin-pair approximation, or ISPA. It assumes that there are no other relaxation pathways that affect the observed cross-relaxation rate and consequent NOESY signal. Use of ISPA can generate an approximate structure based on the NOESY data, but the neglect of relaxation pathways to other nearby protons can cause

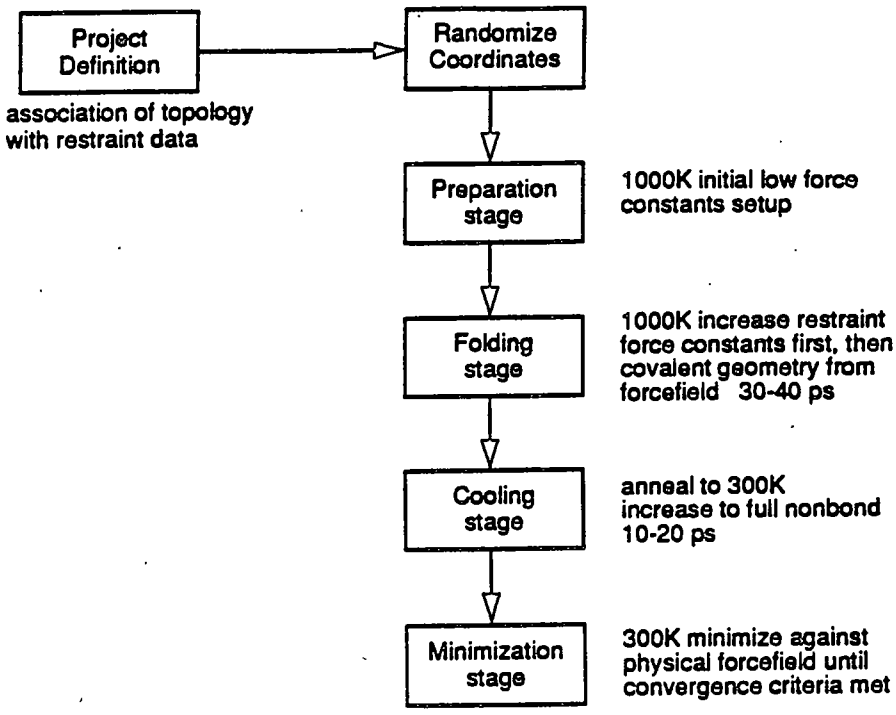


Figure 19. Generalized Simulated Annealing Protocol [From (53)]

substantial errors in distances. Methods have been introduced to more completely model the influence of other protons in the local environment (55 - 58). Two methods that were used in this project to overcome this problem were CORMA (**CO**mplete **R**elaxation **M**atrix **A**nalysis (57, 58)) and MARDIGRAS (**M**atrix **A**nalysis of **R**elaxation for **DI**scerning the **G**eomet**R**y of an **A**queous **S**olution (56, 58)).

CORMA is designed to use the approximate structure generated by ISPA to calculate a complete matrix of cross-relaxation mixing coefficients which are proportional to the NOESY intensities (58). CORMA expands on the ISPA model by calculating the effects of other nearby protons in the structure on the spin pair of interest; effects that were ignored in ISPA. The MARDIGRAS program then iteratively uses the matrix generated by CORMA to get the best set of distances to fit

the observed NOESY constraints and the approximate structure. Two important points of the MARDIGRAS program to note are that it only allows distances with observed intensity to change throughout the course of iterations, and that known distances (i.e. geminal protons) are not allowed to change. MARDIGRAS seeks convergence "in a self-consistent set of distances which simultaneously satisfy the experimental intensities and the set of model intensities" (58) that are derived from the approximate structure. The convergence of a MARDIGRAS run can be evaluated using the so-called R and Q factors, which are defined as:

$$R(\tau_m) = \sum_{ij} |E_{ij}(\tau_m) - T_{ij}(\tau_m)| / \sum_{ij} E_{ij}(\tau_m)$$

$$Q(\tau_m) = \sum_{ij} |E_{ij}(\tau_m) - T_{ij}(\tau_m)| / \{\sum_{ij} E_{ij}(\tau_m) + \sum_{ij} T_{ij}(\tau_m)\}$$

where $E_{ij}(\tau_m)$ is the experimental intensity of the cross-peak between protons i and j at mixing time τ_m and $T_{ij}(\tau_m)$ is the theoretical intensity (59). When a MARDIGRAS calculation is finished, the calculated distances are used to generate an improved structure with simulated annealing and/or molecular dynamics. This improved structure can then be used as a new starting point for CORMA, and the cycle of CORMA and MARDIGRAS calculations repeated until the distances obtained converge.

Applications of NMR and Computer Methods to Peptide and Protein Structure: A Brief Look at the Literature

In the past ten years, as NMR spectrometers and the computers associated with them have become more powerful, the use of 2D, 3D and 4D NMR has become more and more routine as a method to study conformations of all types of molecules. Many early experiments studied the basic pancreatic trypsin inhibitor (BPTI), a 58-amino acid protein, since a high-resolution X-ray crystal structure of it was available (24, 60). The structure of BPTI is well defined in solution and it contains three disulfide bonds which stabilize the structures against unfolding. Indeed, BPTI continues to be used as a reference molecule in the development of new experiments (61) and testing computer analysis of data in the form of molecular geometry programs (52, 62).

Many early studies addressed the bends and turns commonly observed in peptide and proteins (22, 63 -67) and how they would manifest themselves in NMR spectra. This has allowed compilations of tables (24, 27, 66) of NOE interactions that can be observed in polypeptide chains in different conformations. Chemical shifts of different residues in random coils and the assignment of amino acid spin systems and NOE interactions are used to elucidate their solution structures (27). Care must always be used, since the chemical shift of a given amino acid proton can vary with the environment of the residue (68). Another area of caution in the NMR spectroscopy of peptides and proteins is the exchange of the amide protons with water

(69). This can be a problem if a sample is run in concentrated enough D_2O to allow for a significant amount of H ⇌ D exchange or if the pH is sufficiently high to favor rapid exchange with saturated solvent resonances. The problem of suppression of the H_2O signal (which is 110 M compared to millimolar peptide signals) has also been addressed in many hardware and software schemes (61, 70 - 72).

Structures determined by NMR have ranged from peptides (74 - 80), hormones and coenzymes (73, 81), an insulin monomer (82), short DNA sequences (83) and small proteins. Of particular interest in the present research are systems where the TRNOE effect has been successfully employed to determine a receptor-bound structure. This includes the early work of Clore and Gronenborn (41, 42) on the interaction of adenosine 5'-monophosphate with a variety of dehydrogenases and the work of Sykes and Campbell's group on the troponin I - troponin C interaction (31, 44, 84, 85). Campbell and Sykes papers contain many other references to relevant literature. Most of the work in this field has been determining the intramolecular TRNOE signals, although work is underway in the group of Professor Jacob Anglister which also investigates intermolecular TRNOE signals (86 - 88).

The use of NMR constrained molecular dynamics and simulated annealing to refine structures is well documented in the literature. Nilges et al have used NMR constrained simulated annealing to investigate the structure of crambin (a 46 residue peptide) and potato carboxypeptidase inhibitor (a 39 residue peptide) (54). The laboratory of Professor Holak has used simulated annealing in combination with distance geometry to investigate the three dimensional structure of the *E. coli* acyl

carrier protein(89) and a squash trypsin inhibitor, including the stereospecific assignment of the side chains (90, 91). Other groups have used a combination of NMR constrained molecular dynamics and distance geometry to study the structure of neutrophil peptide 5 (92) and a human parathyroid hormone fragment (93). Several excellent review articles on the use of NMR methods in protein structure determination have been published by Bax (24), Clore and Gronenborn (102-104), Opella (105), and Wüthrich(62).

CHAPTER 2

STATEMENT OF THE PROBLEM TO BE SOLVED

The goal of this research project was to investigate the rhodopsin-bound three-dimensional structure of a specific bioactive peptide segment of the retinal rod G protein, transducin. This segment has been shown (7, 20) to possess biological activity similar in some respects to the full G protein. The segment studied consists of a modified portion of the C-terminus of the α subunit of the retinal rod G protein transducin (G_t) that includes amino acid numbers 340 to 350. The peptide chain has been modified to enhance the persistence of its biological activity by the addition of a N-terminal acylation group, and the substitution of a lysine for an arginine in the 341 position. The peptide under study is referred to in shortened notation as Gα Ac-340-350(K341R) to reflect these modifications. This project studied this peptide segment using two-dimensional nuclear magnetic resonance (NMR) and computer refinement methods to investigate the structure of the peptide when free in solution, when the peptide is bound to bovine rhodopsin in an unactivated (dark) state, and finally when the peptide in solution is bound to rhodopsin in its active, metarhodopsin II (light excited) form.

CHAPTER 3

EXPERIMENTAL PROCEDURES

Preparation of Bovine Rhodopsin and Peptides

Critical to the success of this research is the preparation and purification of both the rhodopsin in retinal rod membranes and the peptides to be used. The rhodopsin in retinal rod membranes used in most of the experiments to be reported was supplied by the laboratory of Professor Heidi Hamm. The retinal rod membranes used were isolated from bovine retinas and suitably washed in low salt to remove the native G protein and other proteins bound to the surfaces of the membranes (7, 20). The rod outer segment membranes were washed in the NMR medium which consisted of a solution of 100 mM NaCl, 0.02% sodium azide (NaN_3), 1 mM dithiothreitol (DTT), and 0.2 mM ethylenediaminetetraacetic acid (EDTA). Rhodopsin concentration and purity were checked by ultraviolet/visible absorption spectroscopy on a Shimadzu UV 3000 spectrometer in a scattered transmission sample compartment. A small aliquot (10 microliters) of a rod outer segment sample was diluted to 1000 microliters with the final wash solution for measurement in the spectrometer.

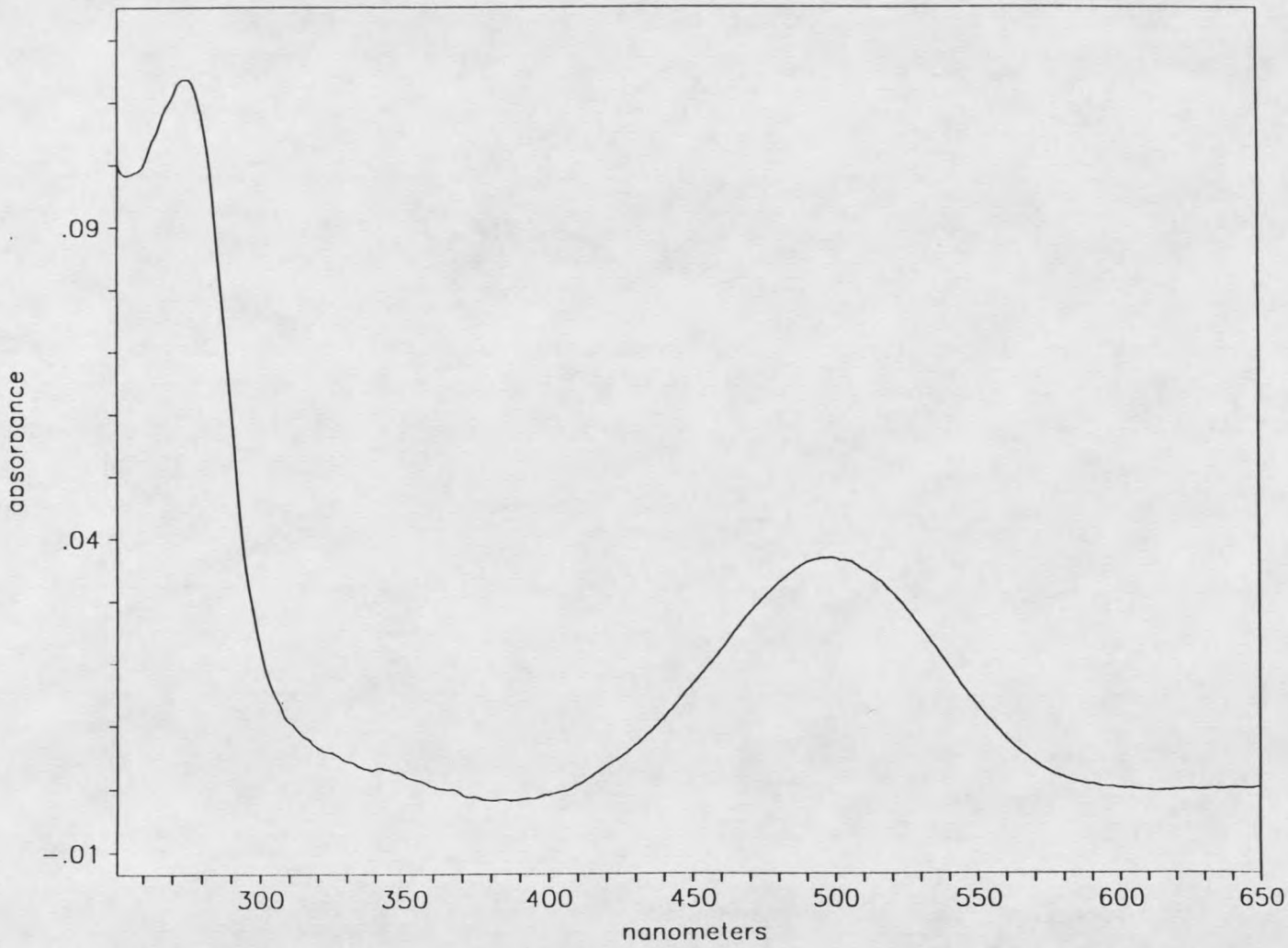


Figure 20. UV/VIS absorption spectrum of a washed rod outer segment membrane sample containing rhodopsin.

Figure 20 shows a sample spectrum from a typical uv/vis run. The spectrum, with its maximum at 500 nm (A_{max} for rhodopsin) and lack of absorption at 380 nm (A_{max} for metarhodopsin II) shows that the rhodopsin has not yet been exposed to light, which is a prime concern at the start of each experiment. The spectrum is also corrected by the subtraction of a scattering baseline. Table 2 gives sample calculations to determine the concentration of native rhodopsin in the sample.

Table 2. Sample calculation of rhodopsin concentration in ROS membranes.

$$A^{498} = 0.037 \qquad C = \frac{0.037}{(40,600)(1)} = 9.13 \times 10^{-7} M$$

$$\frac{(9.13 \times 10^{-7})(810\,\mu L)}{(10\,\mu L)} = 7.38 \times 10^{-5} M = 0.0738\ mM$$

$$7.38 \times 10^{-5} mmol/mL \times 40,000\ mg/mmol = 2.66\ mg/mL$$

The peptide was synthesized using standard solid-phase FMOC (9-fluorenylmethoxycarbonyl) chemistry with Bop/Hobt (benzotriazolyloxy-trisdimethylaminophasphoniumhexafluorphosphate/hydroxybenzotriazole) activation on a Milligen 9050 peptide synthesizer. DMF (dimethylformamide), DCM (dichloromethane), and piperidine used in the synthesis were HPLC grade as supplied by Fisher and VWR. The peptide was purified by HPLC using a Vydac C18 reverse phase preparatory column, and analyzed on a Vydac C18 reverse phase analytical column. Peptide purity was estimated to be greater than or equal to 95% by UV absorbance of the phenylalanine ring in the peptide. Peptide molecular weights were

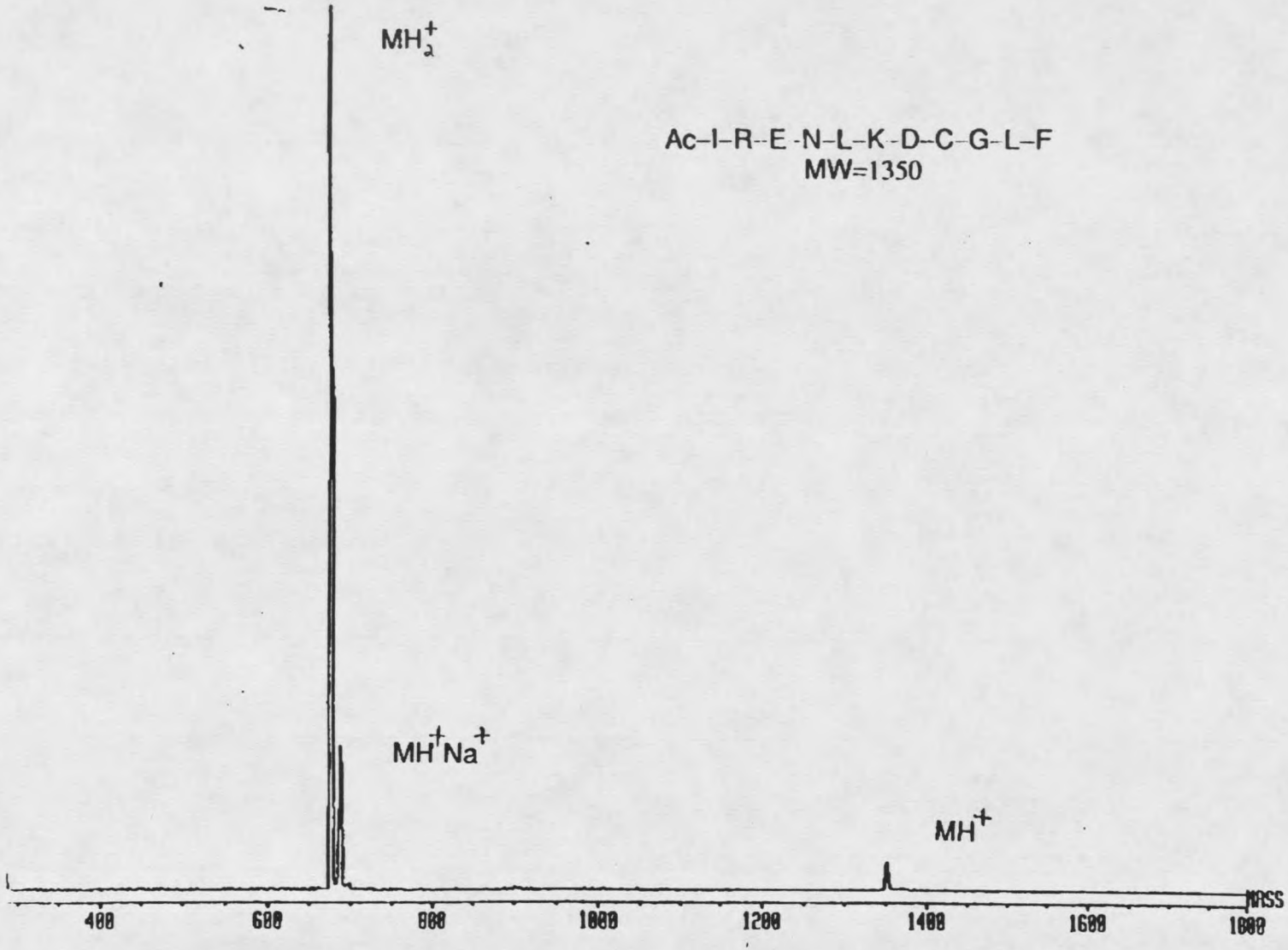


Figure 21. Electrospray mass spectrometry spectrum of Ac-340-350 (K341R).

established by electrospray mass spectrometry. Figure 21 shows the electrospray mass spectrum for the Ac-340-350(K341R) peptide, and Figure 22 shows an analytical HPLC trace of the same peptide sample, both confirming the purity of the peptide used in the experiments. The electrospray shows that peptide impurities are undetectable. The 260 nm HPLC trace indicates low levels of a variety of nonpeptide impurities that have not been characterized.

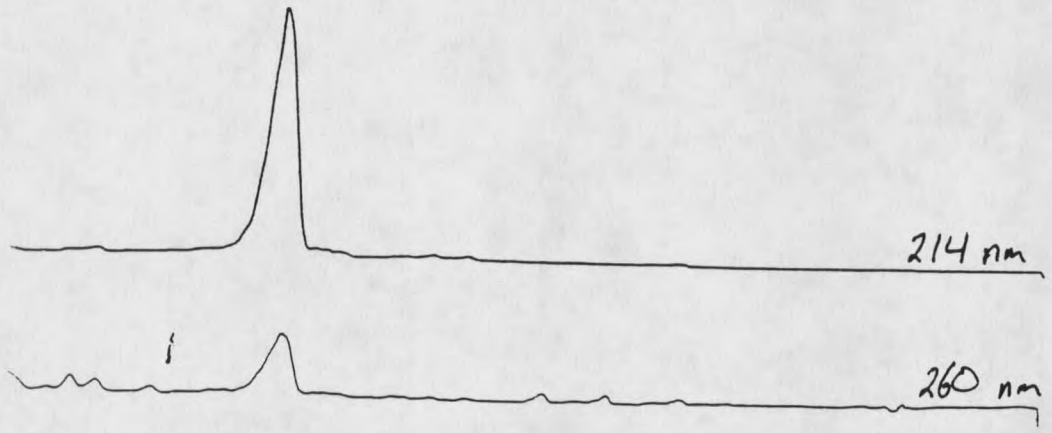


Figure 22. Analytical HPLC trace of Ac-340-350 (K341R).

Preparation of NMR samples

The NMR tubes were cleaned using several washes of absolute ethanol and three final washes of distilled, deionized water. Peptides were dissolved in the same buffer solution as the final rod outer segment membrane wash (100 mM NaCl, 0.02% NaN_3, 1 mM DTT, 0.2 mM EDTA). Depending on the experiment, from 20 to 2 milligrams of peptide was dissolved in 475 microliters of this solution, and the pH was adjusted with NaOH and/or HCl. The peptide solution was then filtered through a centrifugal filter to remove particles greater than 0.22 μm in diameter and pipetted

into an NMR tube. At this time, 25 microliters of 99.9% deuterated water with 0.75% 3-(trimethylsilyl)propionic-2,2,3,3-d_4 acid, sodium salt (D_2O/DSS) was also added. The D_2O served as the lock signal for the NMR, and the DSS as the internal standard in determining chemical shifts. Once the sample was in the NMR tube, the tubes were back-filled with argon gas for 30-second intervals, inverted 10-15 times and the procedure repeated three times to remove excess oxygen that could slowly oxidize cysteine and/or DTT in the sample and could also interfere with certain aspects of the NMR signals (30). After NMR experiments on the free peptide in solution were completed, rod outer segment membranes that had been pH adjusted to match the experimental pH were added to the NMR tubes. The samples were re-purged with argon in the manner described above. If the addition of membrane solution was found to have diluted the D_2O to a level where it was difficult to obtain a sufficiently strong lock signal, additional D_2O/DSS was added, but never to exceed 10% of the total sample volume. ROS membrane samples were kept cold (0°C) in a light-tight container at all times, including when they were being transferred from the laboratory to the NMR instrument. Bleaching of samples, to obtain the activated peptide-MII complex, was accomplished while the sample was immersed in an ice-water bath and exposed to light from a 250-watt tungsten/halogen illuminator equipped with a parabolic cold mirror and light pipe. The illumination was passed through a yellow long wavelength pass optical filter with a 510 nm cutoff. The samples were exposed to light between two and four minutes.

NMR Hardware Conditions

All NMR experiments were conducted on a Bruker AM-500 spectrometer using a proton selective probe. The proton probe had been kept updated by Bruker to give optimum water suppression. Critical to the success of the NMR experiments was the ability to accurately control the temperature of the sample in the probe for the entire course of the experiment. The spectrometer was equipped with a Bruker Eurotherm temperature control unit, which gives a rated temperature stability of 0.1 °C. The Eurotherm controller was calibrated using a methanol standard to ensure that it was reading the proper sample temperature. All experiments were conducted at 1°C, which required other external hardware modifications to the NMR system. A special non-magnetic heat exchanger was constructed that was placed next to the NMR magnet to ensure a short transfer line to supply a continuous supply of cold, dry air to the probe. The Eurotherm controller was used to heat the cold air to provide temperature stability. The air was taken from a compressor, oil and water vapor were removed using three dryers in series. The dry air was run through a 25-foot length of copper tubing immersed in a ethanol cooling bath that was maintained at -40.0°C. Insulated lines then ran from the cooling bath to the heat exchanger for both ethanol and air. The heat exchanger contained a copper coil (approximately 5 feet long) which the air passed through, that was immersed in ethanol circulating from the -40.0° C cooling

bath. The connection for the heat exchanger to the probe was short (approximately 8 inches) and well insulated.

NMR Signal Processing

NMR experiments were performed using spectrometer control software provided by Bruker that was modified for some of the experiments. In particular the NOESY experiments were modified to use a "jump and return" pulse sequence to suppress the water signal (94), an adjustable change in D0/2 to help flatten the baseline in f_1 (95), and hardware phasing (PH0 and PH1) to flatten baselines in f_2 (96). Raw NMR data was transferred via an ethernet connection by the program Bruknet (Bruker Instruments) to Silicon Graphics Indigo or Indigo^2 workstations. Data was then processed using the NMR software FELIX (Biosym Technologies) using several macro routines written by Chris Lambert in our laboratory. Structure analysis was carried out using programs contained within the Discover (50) and NMRchitect packages (53) and the structure refinement program MARDIGRAS (55), obtained from Professor Thomas James at the Department of Biochemistry and Biophysics at the University of California - San Francisco.

CHAPTER 4

EXPERIMENTAL DATA

Ac-340-350(K341R)/Rhodopsin Stability Studies

NMR studies used in determining the structure of the peptide when bound to light excited rhodopsin required the establishment of experimental conditions that would give an Ac-340-350(K341R) (peptide)-metarhodopsin II (MII) complex that was stable for a minimum of 4-6 hours. Work done by other researchers (Thierault and Dratz, unpublished data) had shown that the peptide-MII complex could be stabilized for varying lengths of time at high (> 8) pH. These higher pH studies were unsuitable for NMR work, since the rate of hydrogen-deuterium exchange by amide protons has been shown to be pH dependent (29), and to increase above pH 7 to the point that it obviates the ability to observe the amide protons in NMR. The present work investigated lower pH conditions. Another concern in the stability studies was thought to be the conflicting effects of elevated peptide concentration on destabilization of the peptide/MII complex and the positive dependance on peptide concentration of the signal-to-noise in the transfer-NOE experiments. Several sets of experiments to investigate the stability of the MII-peptide complex as a function of pH and peptide concentration were carried out, and a representative set of data will be shown

in the following discussion.

It should be noted that in the following experiments the peptide/rhodopsin (Rho) concentration will be referred to, not the peptide/MII concentration. The concentration of Rho in the dark membranes can be determined spectrophotometrically at the beginning of an experiment (see Chapter 3, Figure 20 and Table 2), whereas sample bleaching may not be 100 % complete, peptide stabilization of MII is certainly not 100 % efficient, and other intermediates will be present in variable amounts. All peptide ratios are expressed as between the peptide and the initial concentration of rhodopsin. Figure 23 shows uv/vis absorption plots (difference mode) for the 15:1 peptide/Rho concentration as a function of time after bleaching at pH 6.5 and 5 °C, allowing observation of the decrease in absorbance at 380 nm (the MII absorbance maximum) to be measured. The top trace (between 340 and 410 nm) is the first scan immediately after bleaching, with a scan time of two minutes between 650 and 250 nm; subsequent traces are taken at 15 to 30 minute intervals (see Figure 24). The half-life of the complex was determined by plotting the natural logarithm of the absorbance difference at 380 nm (maximum absorbance wavelength of MII) relative to the unbleached sample versus the time after the bleaching of the sample was completed. An example of a plot of this data is given in Figure 24. An initial linear regression was performed on the first seven data points since the data is not linear over the course of the entire experiment, and a second regression performed for the residual later data. The line shown in the plot has an equation of log A = -0.0022 x time - 1.01 and first-order kinetics implies the half-life of this complex as 2.3 hours.

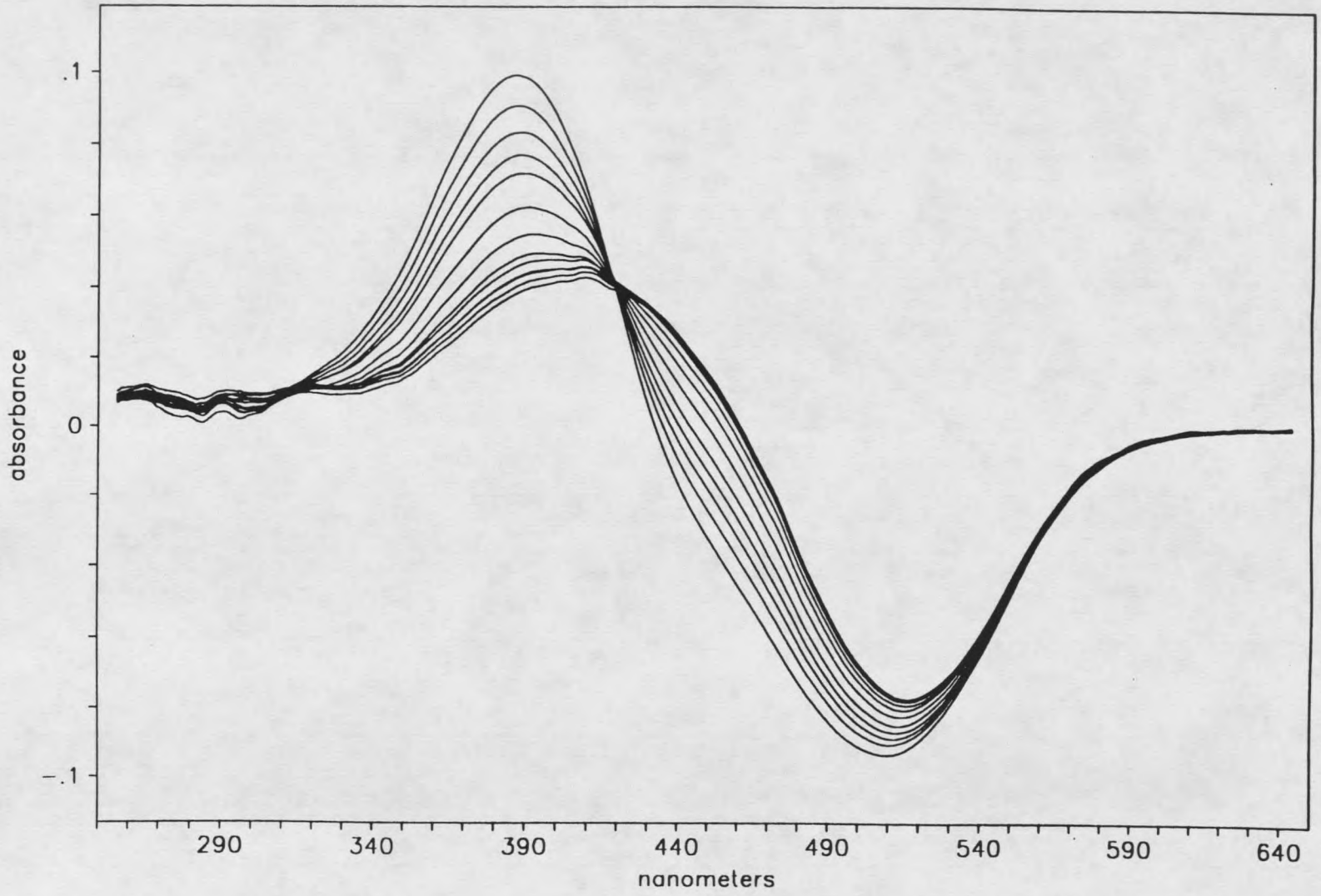


Figure 23. Difference absorption spectra for a 15:1 peptide/rhodopsin mix after bleaching. Successive traces are 15 - 30 minutes apart. (See Fig. 24)

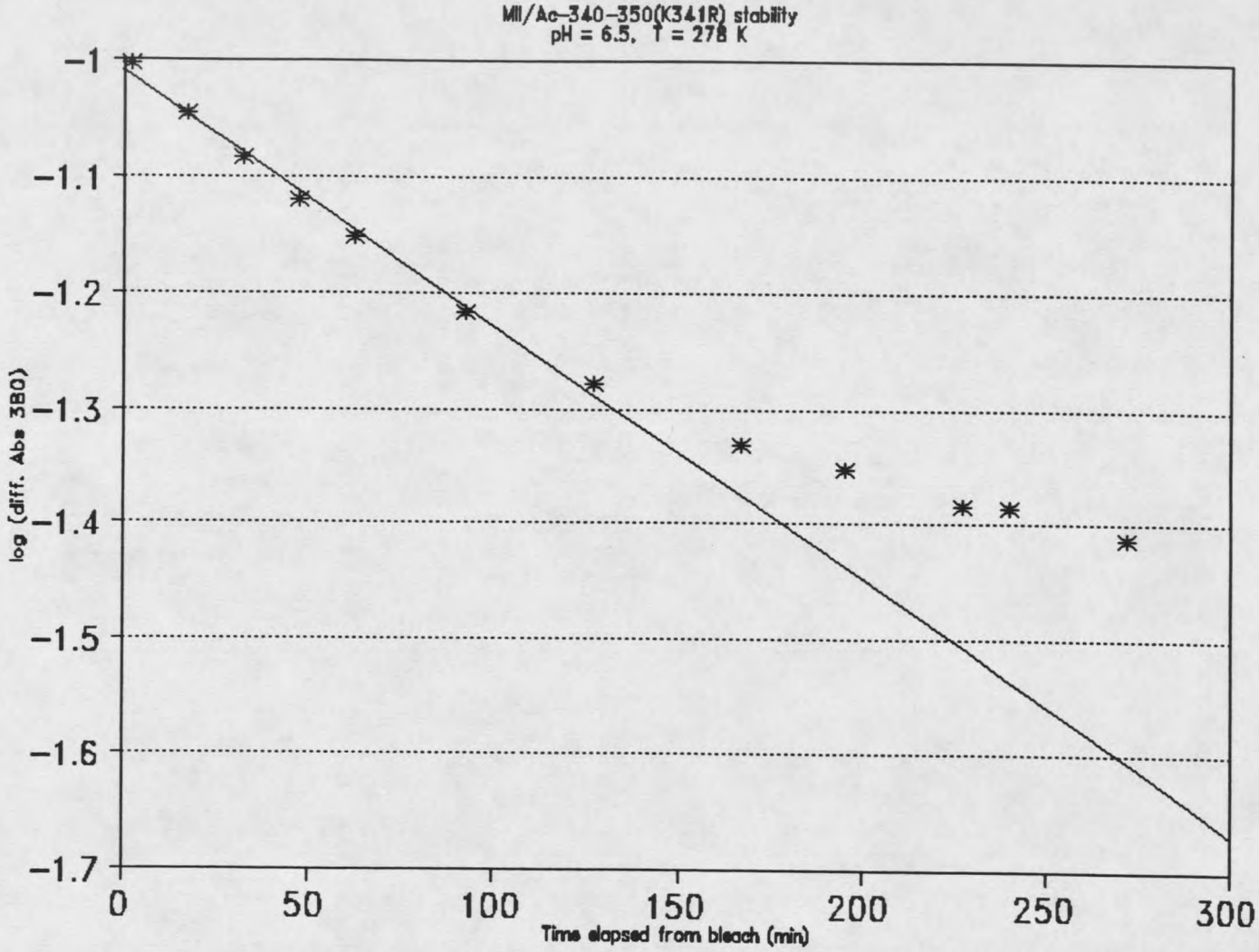


Figure 24. Linear regression of a plot of a 15:1 peptide/rhodopsin mixture after bleaching.

The source of the slower decay beyond 150 min is thought to be due to the build-up of the MIII intermediate. Litman and coworkers have shown (16) that MIII can be pulled back to MII by the intact G_t heterotrimer. Since the G_t heterotrimer can stabilize MII relative to MIII, it is likely that the most active Gα-340-350 can also do so. Shifting of the MII⇌MII equilibrium toward MII by the peptide could reasonably give a slower decay of MII as MIII appears. Data for the rate constants at various peptide concentrations, along with the pH dependance of the initial (fast) decay rate, is given in Figure 25, with the slower decay rate constants at pH 6.5 plotted in Figure 26. The dominant effects in the initial decay are stabilization of MII with increased peptide concentration, but destabilization at the lower pH. It is also possible that the slower decay phase of MII is due to retinal formation which has peak absorbance at 387 nm. A large number of uv-vis experiments at pH 6.5 with various peptide concentrations all appear to give long enough MII-peptide stability for NMR experiments to be carried out at these conditions (see Table 3). On the basis of this data, combined with knowledge of the amide exchange rate as a function of pH, it was determined that the best pH condition to try for the NMR experiments was pH = 6.5. The NMR work was started at an initial peptide/Rho concentration of 100:1, and peptide concentration was gradually incremented to lower values. Data for a number of these experiments is summarized in Table 3.

Lower peptide/protein ratios were emphasized in the present work because of an initial miscalculation of the MII decay rate as a function of peptide concentration at pH 6.5. Further experiments with the Ac-340-350(K341R) peptide should be carried

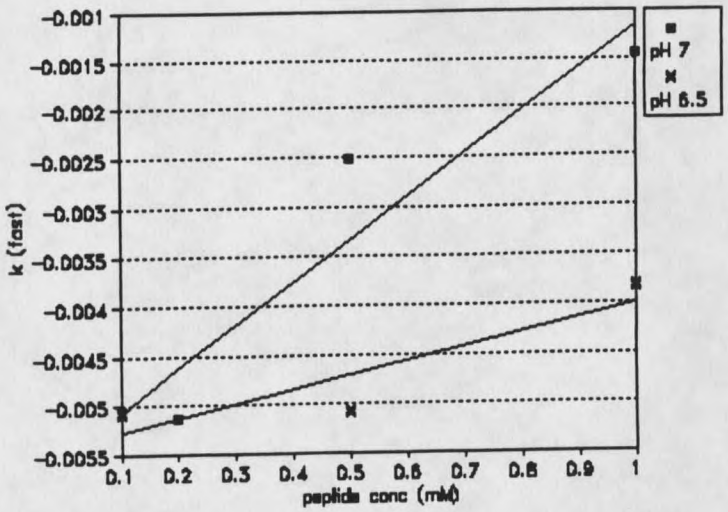


Figure 25. Initial decay rate constant ("k^{fast}") of peptide-MII complex vs peptide concentration.

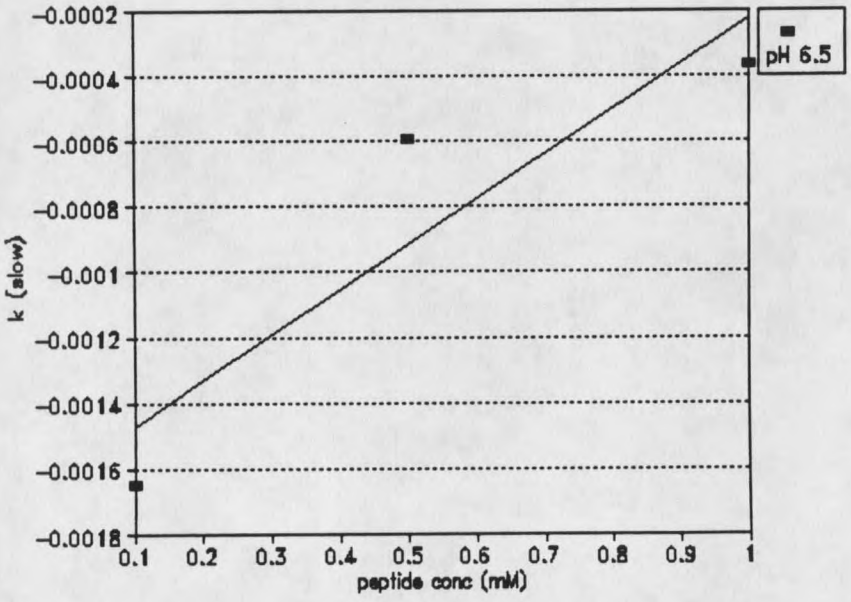


Figure 26. Secondary rate decay constant ("k^{slow}") of peptide-MII complex at pH 6.5.

out at higher peptide concentrations, which will prolong the persistence of MII for better signal-to-noise. The higher peptide concentrations may not increase the signal-to-noise ratio of the transfer NOESY experiments done in the same time frame unless the amount of receptor protein is also increased. This is due to the fact that intramolecular TRNOESY increases with the percent of bound peptide (p_b), and p_b goes down with elevated peptide at a fixed protein concentration.

Table 3. Stability of Peptide/MII complexes.

Peptide/Rho ratio	pH	Half-life (k^{fast})(hr)	Half-life (k^{slow})(hr)
30:1	7.0	2.26	NA
50:1	7.0	4.54	NA
100:1	7.0	6.95	NA
15:1	6.5	2.30	7.0
50:1	6.5	2.27	19
100:1	6.5	3.00	32

Free Ac-340-350(K341R)

Spectral Assignment

The assignment of the proton resonances in the free peptide was accomplished with two principle experiments. The first experiment used is TOtal Correlation SpectroscopY (TOCSY). This experiment allows the assignment of most of the protons in a given spin system, in this case each amino acid residue, in a single experiment. Figure 27 shows the backbone αH - NH region of the TOCSY spectrum of the free peptide; the other regions of the TOCSY spectrum are shown in the Appendix. The TOCSY spectrum leaves some ambiguities in assignments when

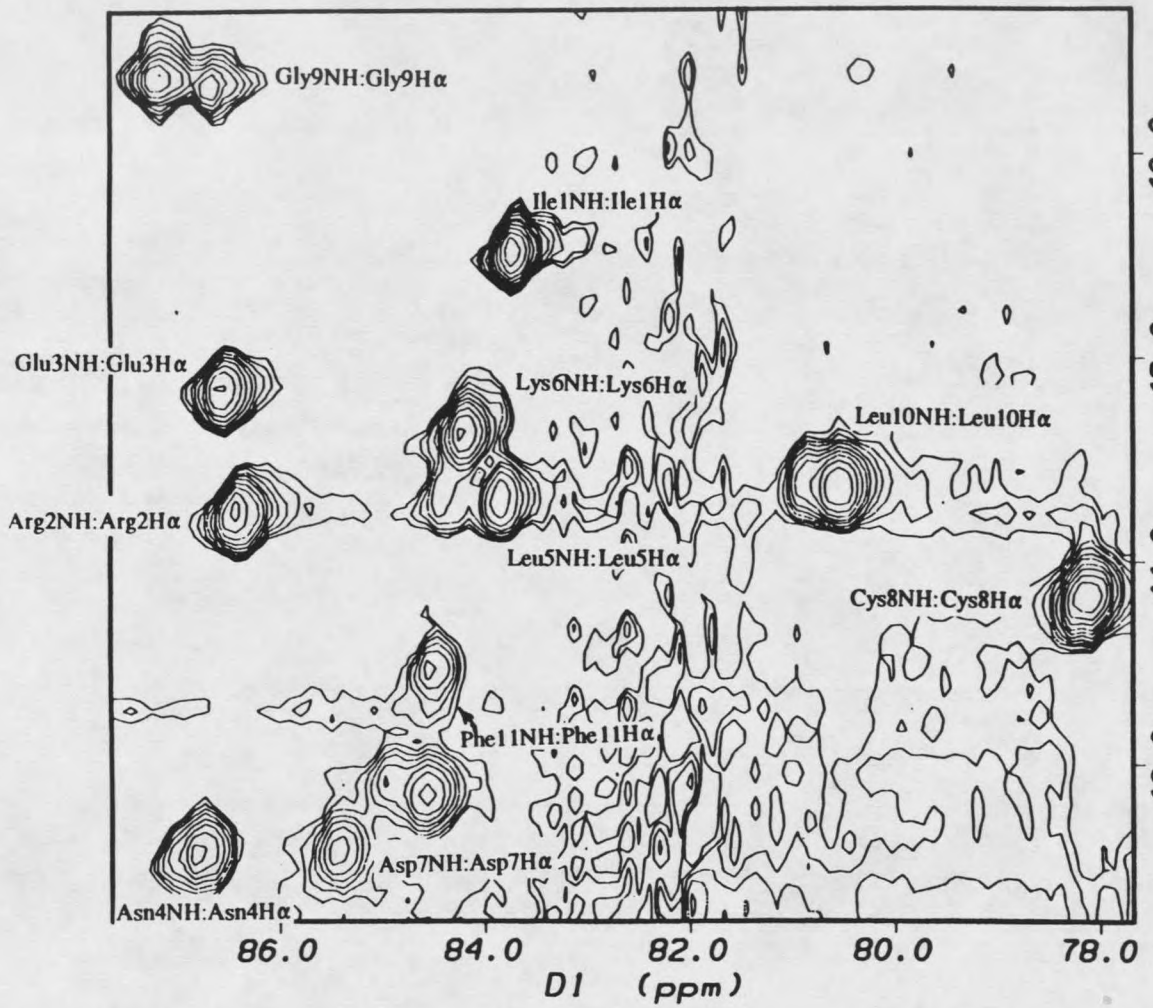


Figure 27. TOCSY spectrum (αH - NH region) of the free peptide Ac-340-350(K341R). NS = 48, NE =936.

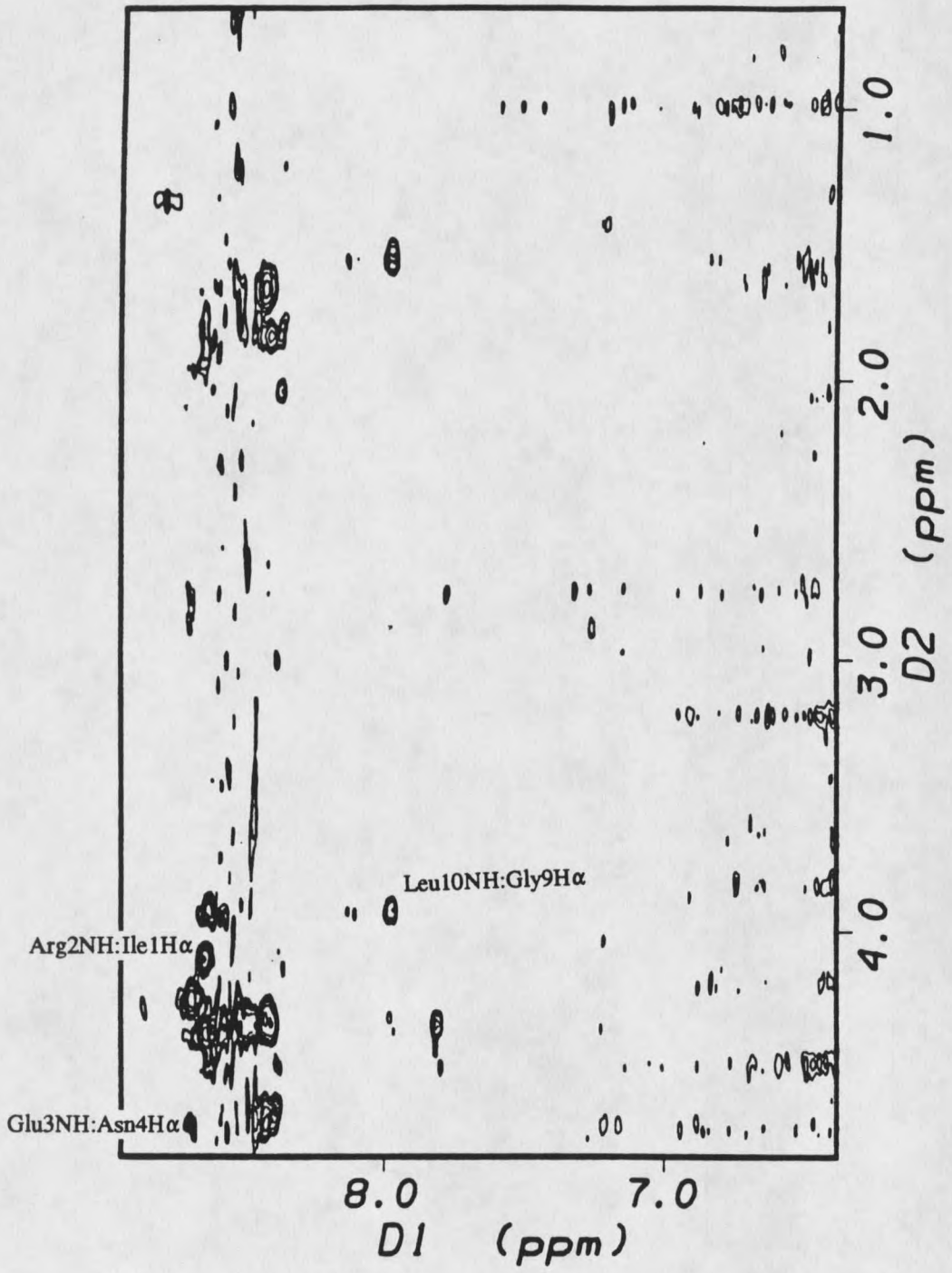


Figure 28. NOESY spectrum (NH - αH and sidechain H) of the free peptide Ac-340-350(K341R). τ_{mix} = 150 msec, NS = 32, NE = 256.

residues have very similar or overlapping shifts, so Nuclear Overhauser and Exchange SpectroscopY (NOESY) experiments were also carried out to complete the assignments. In a NOESY experiment, the cross-peaks are the result of cross-relaxation between two protons within an acceptable distance of each other in space, not because they are a part of the same coupled spin system (see Chapter 1). Figure 28 gives the NH - αH and NH -sidechain region of a NOESY spectrum, with a mixing time (τ_{mix}) of 150 msec, for the free peptide. Other regions of the NOESY spectrum are shown in the Appendix. At this mix time, the NOESY spectrum of the free peptide is weak and longer mix times were useful to confirm assignments (data not shown). A total of 22 NOESY cross-peaks were observed in the free peptide, with the majority of them being either intra-mononer NH - αH or sequential inter-monomer NH - αH. By using these two experiments, all protons of the free peptide were assigned. The list of assignments for the free peptide is given in Table 4.

NOE Build-up Rates

Another important set of experiments for the free peptide was the determination of the rates of NOE build-up for various protons. This information is useful in the computer simulations and indicates t_{mix} values where the system is in an approximately linear build-up region. When the build-up is nearly linear, the NOE intensity is approximately inversely proportional to the sixth power of the distance between two protons. Comparison of NOE build-up rates between the free, dark-bound, and light-bound peptides show new relaxation pathways as the peptide undergoes changes in conformation as it binds to rhodopsin and metarhodopsin II. NOESY experiments

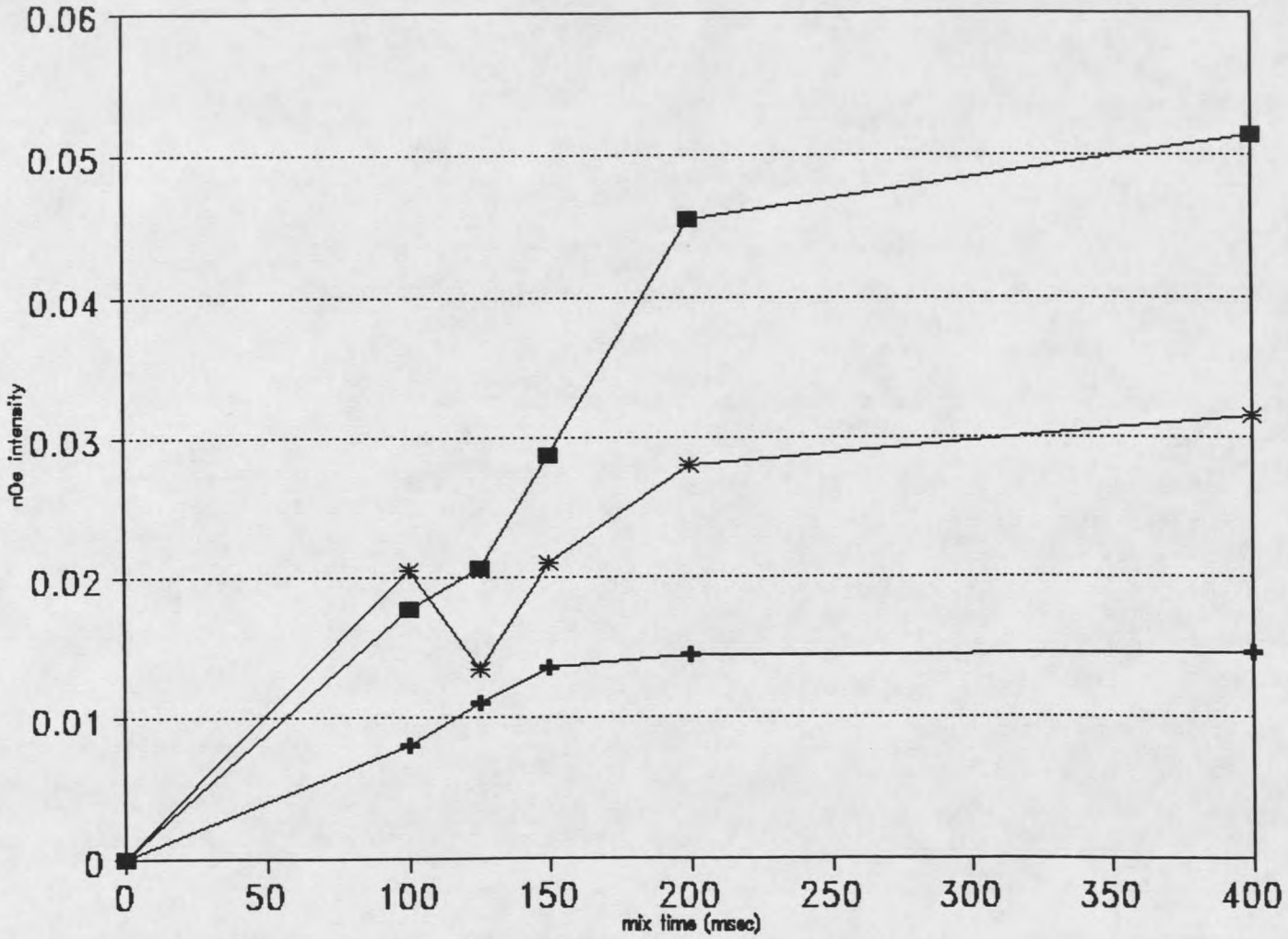


Figure 29. NOE build-up curves for the free peptide Ac-340-350 (K341R).

Table 4. Assignment of proton shifts in the free Ac-340-350 (K341R) peptide.

Proton	Chemical Shift (ppm)	Proton	Chemical Shift (ppm)
Ile NH	8.36	Lys NH	8.41
Ile αH	4.10	Lys αH	4.28
Ile βH	1.84	Lys βH	1.83
Ile γCH_2	1.22, 1.50	Lys γH	1.44
Ile γCH_3	0.92	Lys δH	1.68
Ile δH	0.89	Lys ϵH	2.99
Arg NH	8.63	Asp NH	8.48
Arg αH	4.36	Asp αH	4.62
Arg βH	1.78, 1.88	Asp βH	2.68, 2.78
Arg γH	1.66	Cys NH	7.81
Arg δH	3.22	Cys αH	4.45
Arg ϵNH	6.54, 6.98	Cys βH	2.96, 3.19
Glu NH	8.63	Gly NH	8.65
Glu αH	4.24	Gly αH	3.95
Glu βH	1.95, 2.03	Leu NH	8.08
Glu γH	2.28	Leu αH	4.32
Asn NH	8.68	Leu βH	1.46, 1.53
Asn αH	4.70	Leu γH	1.51
Asn βH	2.77, 2.87	Leu δH	0.83, 0.91
Asn NH_2	7.05, 7.77	Phe NH	8.44
Leu NH	8.42	Phe αH	4.52
Leu αH	4.34	Phe βH	2.99
Leu βH	1.68	Phe 2,6H	7.24
Leu γH	1.62	Phe 3,5H	7.35
Leu δH	0.87, 0.94	Phe 4H	7.30

were run on the free peptide at a variety of mixing times (τ_{mix}): 100, 125, 150, 200, and 400 msec. Figure 29 shows the build-up rates for several representative protons in the peptide. These protons were selected for the graph since they show a backbone NH-CαH inter-monomer interaction, a backbone NH-CαH and CβH-CγH intra-

monomer interactions. In each of these cases, the NOE build-up maximized by the 200 msec mixing time or showed little further increase at 400 msec. Since the peptide should show faster relaxation times when bound to the protein (41, 42), this also determined that when the peptide-protein experiments were carried out, that 200 msec was the longest mixing time that needed to be investigated. This is very useful information, since the light activated state of the protein has limited stability. Experiments with shorter mixing times take significantly less time to run than the long mixing times such as 400 msec. Also, since fresh samples are needed for each mixing time in the light-excited samples, it is useful to avoid mixing times that have little chance of providing useful data.

Relaxation Rates

The final measurements on the free peptide were determination of the longitudinal (T_1) and transverse (T_2) relaxation rates. T_1 for the free peptide was determined by the use of an inversion-recovery pulse sequence and T_2 was determined with a CPMG pulse sequence. T_1 was calculated from the slope of a graph of $\ln(M_\tau - M_\infty)$ vs. τ(the delay in the pulse sequence) and found to be 490 msec for the asparagine NH proton. The T_1 value of this proton was of interest, since it showed a small but detectable shift in the free and bound chemical shift, which has great significance later. T_2 was determined in a similar manner and found to be 69 msec. The free peptide had small negative NOEs, so the peptide was on the slow side of the T_1 minimum under these conditions and T_2 is expected to be faster than T_1. Slight increases in sample temperature were able to zero the free peptide NOEs, also showing

that the initial motional state was on the slow motion side of the NOESY null which is also on the slow side of the T_1 minimum. Experimentally, measurement of T_2 is more difficult than T_1 due to greater sensitivity to mis-set pulses, and errors could have occurred.

Ac-340-350(K341R) + "Dark" Membranes

Before beginning the discussion of the rhodopsin-bound peptide, one key point should be introduced. The experiments in this project were designed to optimize the conditions for the light-bound state, not for the dark-bound state. The dark-bound experiments were carried out as controls for light - dark differences under the same experimental conditions that were used for the light-bound state. Conditions optimized for the best light-bound data gave poorly defined dark-bound structures, due to the short NOESY experiments involved. Experiments carried out by others in the laboratory provide much more detailed structural information on the dark-bound state and the dark-bound structure is still undergoing refinement.

Spectral Assignment

Initial investigation of the TOCSY spectrum of the peptide plus dark membranes showed little change in the position of cross-peaks, and essentially no changes in the relative positions of the cross-peaks. TOCSY data for the rhodopsin-bound peptide will not be shown here as assignments were based on the table given previously (Table 4).

NOE Build-up Rates

NOE build up curves were generated for the peptide in the presence of the dark adapted membranes using multiple NOESY experiments. The experiments were carried out up to 200 msec mixing time. Longer mixing times were not deemed necessary since, in the free peptide, NOE build-up had maximized or leveled off by 200 msec. The bound NOE should build-up much quicker (41, 42), therefore longer mixing times were not used. A spectrum from fingerprint region of the 150 msec τ_{mix} NOESY experiment is shown in Figure 30, with the other portions of the spectrum shown in the Appendix. This spectrum was acquired under the same conditions as the portion of the free peptide shown in Figure 28. The NOESY spectrum of the peptide plus dark membranes contains more cross-peaks than the free peptide (48 vs. 22). In addition, several of the cross-peaks present in the free peptide are lost in the presence of the dark membranes. The loss of NOESYs present in the free peptide upon binding indicates definite conformational restriction upon binding to rhodopsin. Additionally, more of the peaks in the presence of the dark membrane represent longer range NOEs and more NOEs within side-chains, indicating a more rigid structure. However, a small number of these cross-peak assignments (e.g. Phe 11 H2,6:Cys 8 Hα shown in Figure 30) have been called into question (Rizo and Gierasch, personal communication). In the structure refinement programs used, this did not affect the results, since these peaks were discarded as unable to fit with the rest of the data.

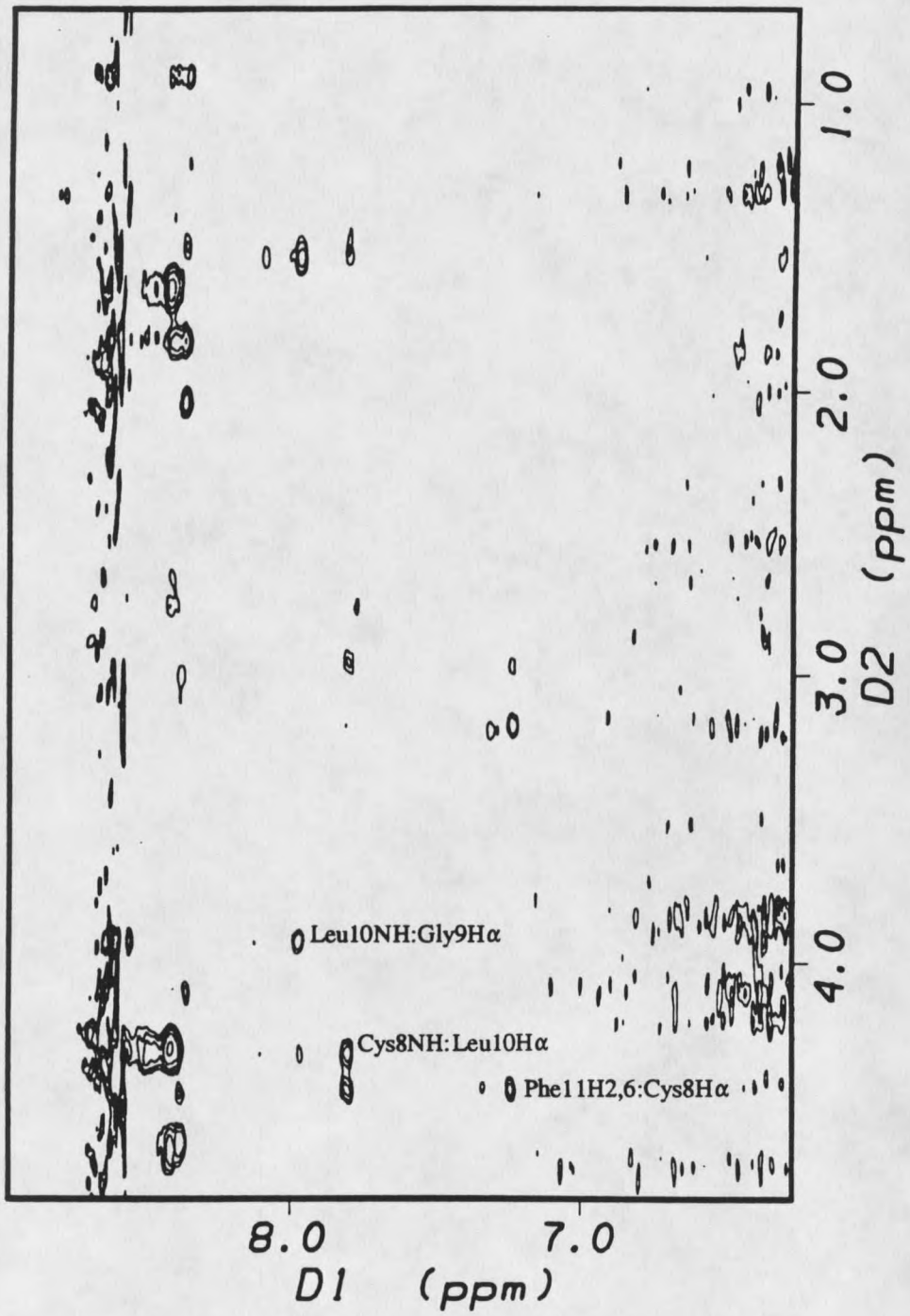


Figure 30. NOESY spectrum (NH - αH and sidechain H) of the peptide Ac-340-350 (K341R) and rhodopsin (dark) in a 15:1 molar ratio. τ_{mix} = 150 msec, NS = 32, NE = 256.

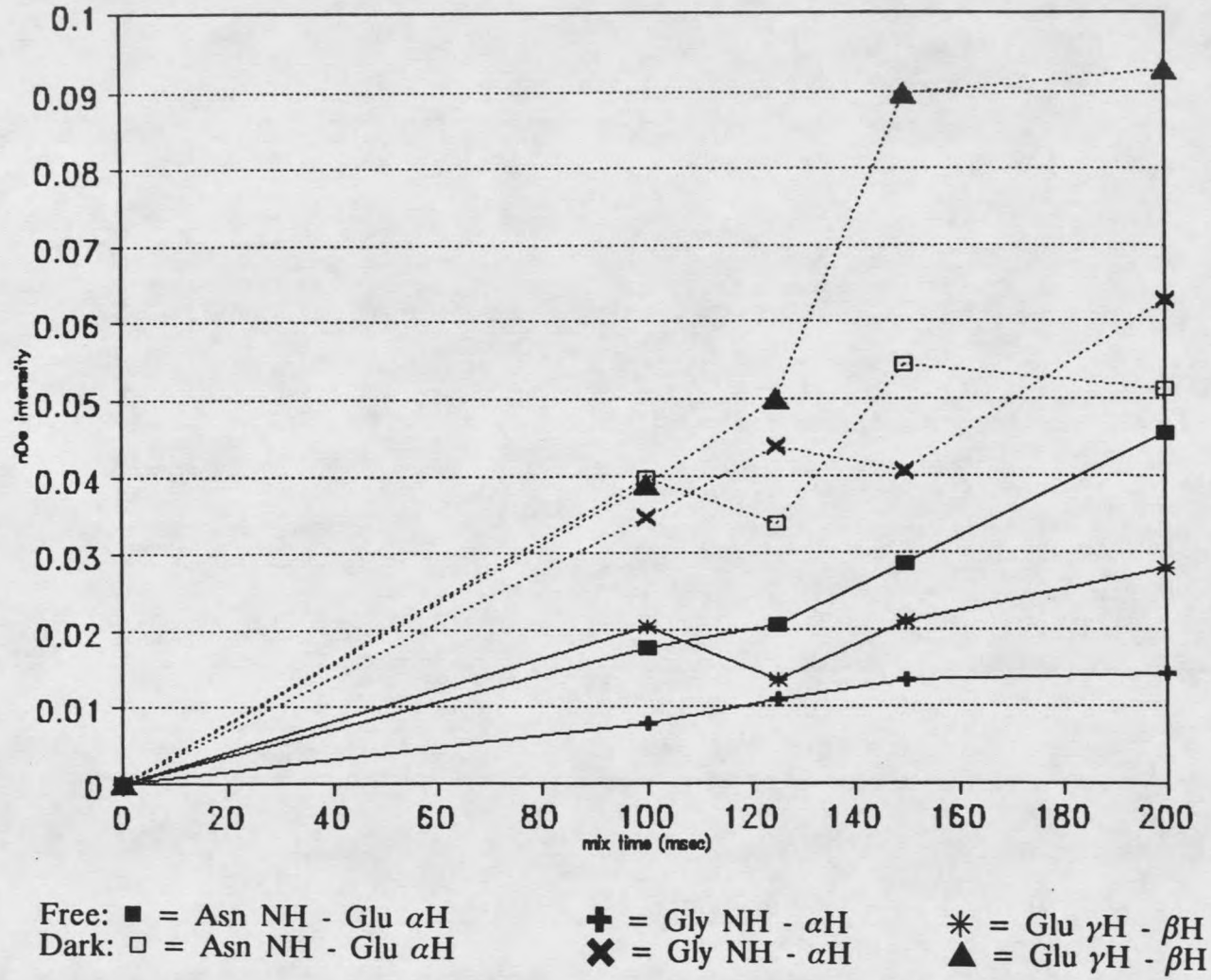


Figure 31. NOE build-up curves for the free peptide Ac-340-350 (K341R) and a 15:1 mixture of peptide and rhodopsin (dark).

Investigation continues in the Dratz laboratory to resolve the possible problem of these assignments.

Figure 34 shows, for both the dark-bound and light-bound states, the number of new NOESY cross-peaks seen per amino acid. This data indicates new cross-peaks in both the N- and C-terminal ends of the peptide. In Figure 31, several series of NOE build-up curves are shown, comparing the free peptide and dark adapted membrane bound states. In general, the curves show increased build-up rates, although some build-up rates do go down in the presence of dark and light membranes (data not shown), indicating changing peptide conformation in the presence of the membrane receptors.

Peptide - Protein Exchange Kinetics

The relaxation rates (T_1 and T_2) of the peptide when bound to the "dark" membranes were determined, as part of estimates of the rate of peptide-protein exchange. T_1 and T_2 measurements were carried out in the presence of dark membranes as described previously for the free peptide, and values of T_1 = 347 msec and T_2 = 25 msec were obtained at a 15:1 peptide to protein ratio. These observed values contain contributions from the free peptide and must be corrected to represent the values for the bound peptide only. The relationship

$$\frac{1}{T_1^{obs}} = \frac{P_f}{T_1^f} + \frac{P_b}{T_1^b}$$

can be used to calculate the true T_1 for the bound peptide (and the analogous equation

used for calculating T_2). The values for the mole fraction of free and bound peptide (p_f and p_b) were estimated initially to be 0.933 and 0.067 respectively, based on the 15:1 peptide to protein ratio. This gave a value of 68 msec for T_1^b and 2 msec for T_2^b.

Next, an experiment to measure $T_{1\rho}$ as a function of spin-lock power was performed in order to arrive at a value for k_{ex}, which is related to the peptide off-rate. As discussed previously, $R_{1\rho} = 1/T_{1\rho}$, can be related to the spin-lock power (ω_{SL}) by the equation (45):

$$R_{1\rho}^{ex}(\omega_{SL}) = p_f[\cos^2(\beta_f)/T_1^f + \sin^2(\beta_f)/T_2^f] + p_b[\cos^2(\beta_b)/T_1^b + \sin^2(\beta_b)/T_2^b] + p_f p_b \sin^2(\beta)\Delta\omega^2[k_{ex}/(k_{ex}^2 + \omega_{SL}^2)]$$

Figure 32 shows a plot of the experimental $R_{1\rho}$ vs. spin-lock power data (data points with error bars), and a computer fit of the above equation (solid line). The three dashed lines represent the three terms shown in the above equation. In order to fit the equation to the data, values of T_1^b, T_2^b, p_f, p_b, k_{ex}, and $\Delta\omega$ were all varied. The validity of allowing T_1^b, T_2^b, p_f, and p_b to vary can perhaps be questioned, but since the relaxation values were determined from assuming a certain percent of peptide bound, it seems that flexibility must be allowed to account for uncertainties in these variables until a better, independent way to measure the percent of bound peptide can be established. The largest discrepancies were at higher spin-lock powers, where sample heating could be a problem. Terms 1 and 2 tended to be too large to fit the $R_{1\rho}$ at high ω_{SL}, whereas the large inflection in the third term as a function of ω_{SL}, that was the only term that depended on kinetic exchange, fit reasonably well. The smaller the p_b, the larger the T_1^b and the T_2^b, and the smaller the second term. The

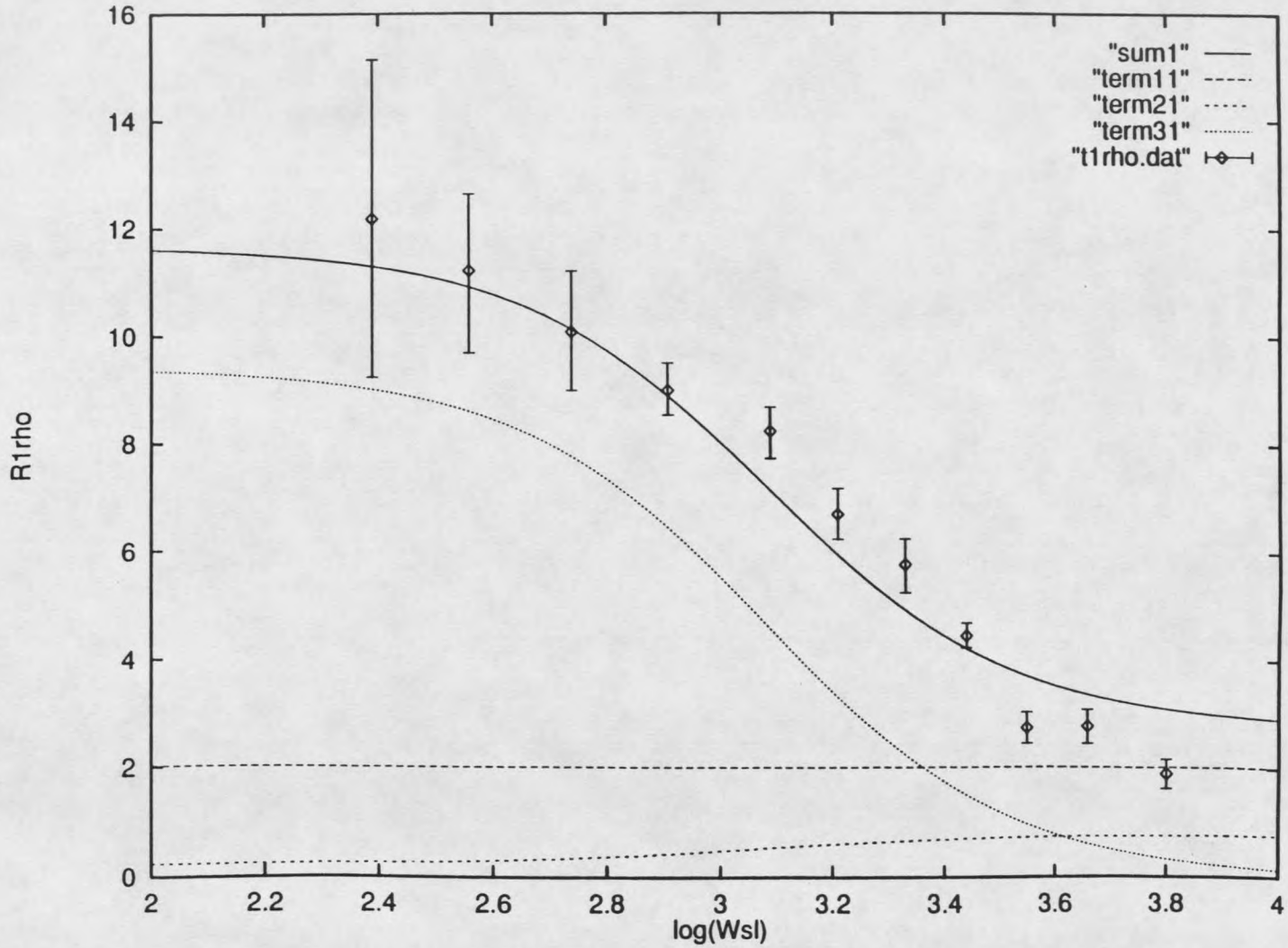


Figure 32. $R_{1\rho}$ vs. log (ω_{SL}) for a 15:1 mixture of peptide and rhodopsin (dark).

parameters were pushed to the limits of $T_2^f \approx T_1^f$ and $p_b \approx 0.01$ to obtain the fit shown in Figure 32. We were reasonably comfortable with the value of k_{ex}, which depends primarily on the break point of the third term, but do not have a lot of confidence in the other parameters derived from the fit. Perhaps there is more than one important correlation time for the relaxation, or the $T_{1\rho}$ relaxation rates are much too low at the higher spin-lock power due to experimental error. It is estimated that k_{ex} could fall between 1000 and 1400 sec^{-1}, which is well above the fast exchange limit on the pertinent cross-relaxation time scale. Figure 32 represents the best fit of the data, and Table 5 gives the values used in this fit.

Table 5. Values used to best fit experimental $R_{1\rho}$ vs ω_{SL} data (dark-bound).

$T_1^f = 0.490$ sec	$p_b = 0.01$
$T_2^f = 0.490$ sec	$p_f = 0.99$
$T_1^b = 0.043$ sec	$k_{ex} = 1200\ sec^{-1}$
$T_2^b = 0.013$ sec	$\Delta\omega = 170$ Hz

Ac-340-350(K341R) + "Light" Membranes

Spectral Assignments

Due to the relatively short-lived nature of the activated peptide/MII complex, TOCSY experiments were not run on this system. Instead, 1D NOE and NOESY peaks were compared between the free, dark, and light experiments. Once again,

shifts in cross-peak positions were quite small, so the original assignment list generated for the free peptide (Table 4) was used.

NOE Build-up Rates

NOE build-up curves were generated for the peptide with a series of NOESY experiments in the presence of the light excited membranes at τ_{mix} values of 100, 125, 150 and 200 msec. Figure 33 shows a portion of the spectrum of the 150 msec experiment, with the rest of the spectrum given in the Appendix. This spectrum is of the same sample after light excitation as shown in Figure 30 for the dark sample. Since the MII-peptide complex has a relatively short lifetime, fresh samples were needed for each mix time to complete build-up curves for the light bound state. These curves were normalized to absolute fractional NOE intensities by using the volume of several diagonal peaks that were known to be single protons (such as an isolated alpha) or half the volume of degenerate beta or gamma proton pairs. This procedure of conversion of relative NOE intensities to absolute fractional NOE intensities was also carried out for the free and dark-bound spectra, so that the build-up curves could be properly compared. A larger number of NOE cross-peaks were measured for the peptide in the short NOESY experiments in the presence of the light excited membranes (71 cross-peaks) than in the presence of the dark membranes (48 cross-peaks). Figure 34 shows the number of new cross-peaks for each residue in both the light- and dark-bound state. It should be noted that the cross-peaks that appeared in the dark-bound form are still present in the light. It is particularly interesting to note the significant number of new cross-peaks noted for the two leucine residues.

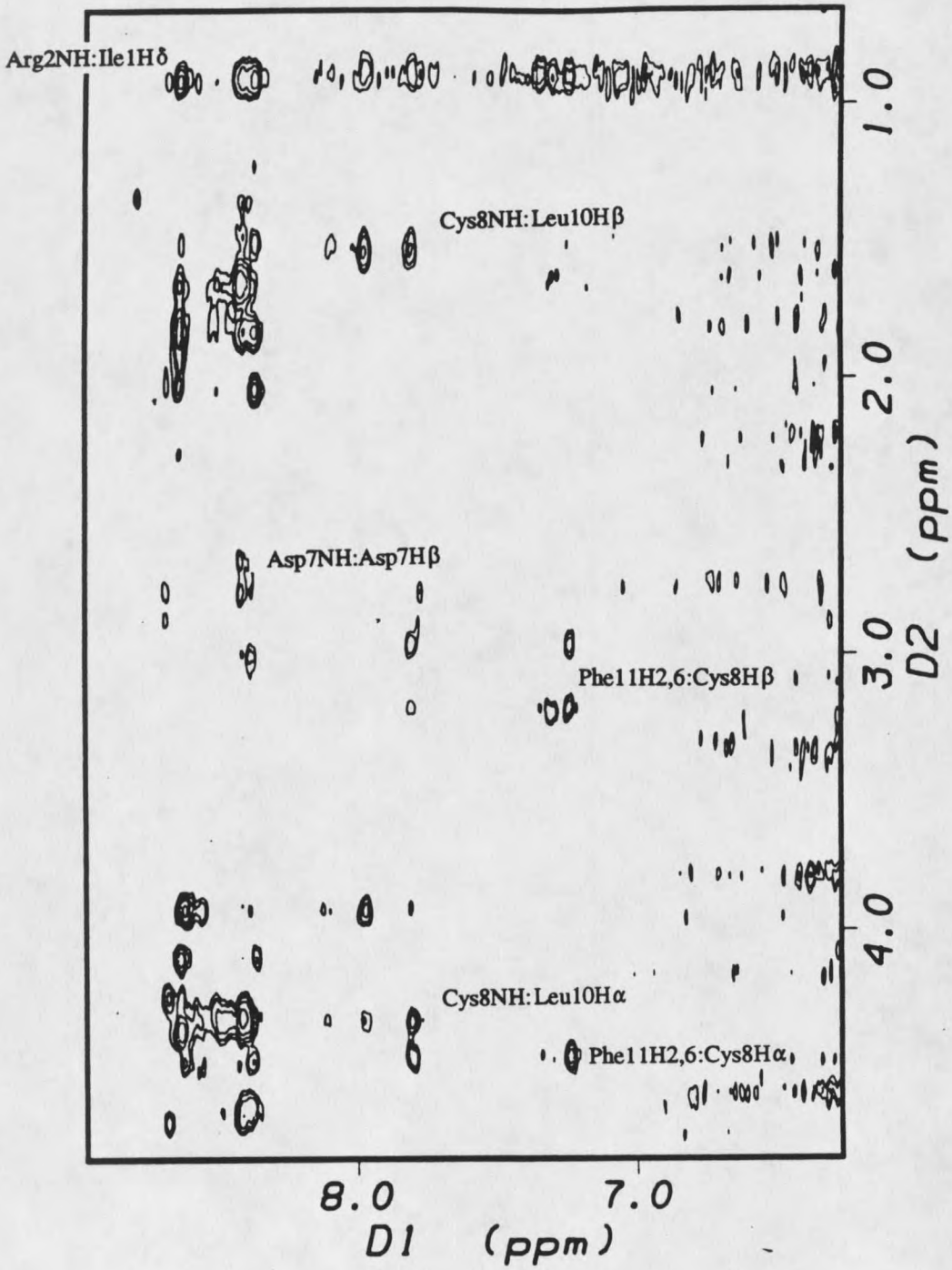


Figure 33. NOESY spectrum (NH - αH and sidechain H) of the peptide Ac-340-350 (K341R) and metarhodopsin II (light) in a 15:1 molar ratio. τ_{mix} = 150 msec, NS = 32, NE =256.

These residues are conserved in a number of other G protein α subunits (20), and appear to have particularly strong interactions in the light-bound form of the peptide.

The light-bound database of NOE assignments was also overlaid on the dark spectrum and integrated to check for any cross-peaks that may have also been present in the dark sample, only at a very low intensity. Using this database revealed a few low intensity cross-peaks in the dark-bound spectrum, and also showed that there were no significant shifts in cross-peaks in the dark- and light-bound spectra. Figure 35 shows the build-up curves for the same NOE's as in Figure 31, now comparing the free and light build-up rates. Finally, Figure 36 plots the build-up rates of the same NOE's in the dark- and light-bound states.

Peptide - Protein Exchange Kinetics

The relaxation rates (T_1 and T_2) of the peptide when bound to the "light" membranes were initially assumed to be the same as those for the "dark" membranes, so that the lifetime of the light bound peptide could be fully used to run $T_{1\rho}$ measurements. Figure 37 shows a plot of the experimental $R_{1\rho}$ vs. spin-lock power data (data points with error bars), and a computer fit of the above equation (solid line). The three dashed lines represent the three terms shown in the equation. In order to fit the equation to the data, values of T_1^b, T_2^b, p_f, p_b, k_{ex}, and $\Delta\omega$ were allowed to vary as described previously for the dark-bound peptide. Figure 35 represents the best fit of the data, and Table 6 gives the values used in this fit. It can be seen in comparing Table 5 with Table 6 that very little change in the best fit parameters relating $R_{1\rho}$ to spin-lock power occurs between the dark and light bound states, except for a shorter

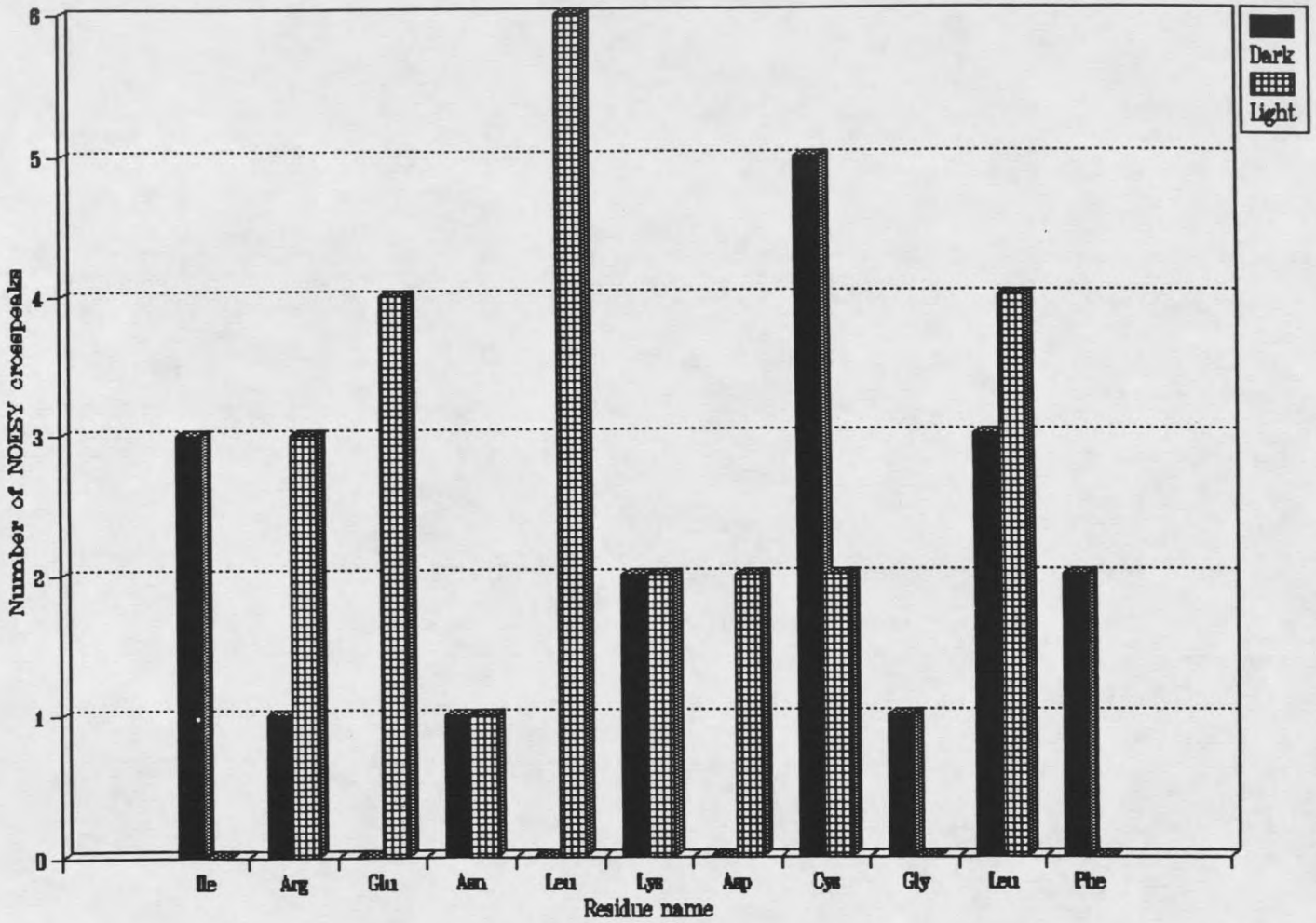
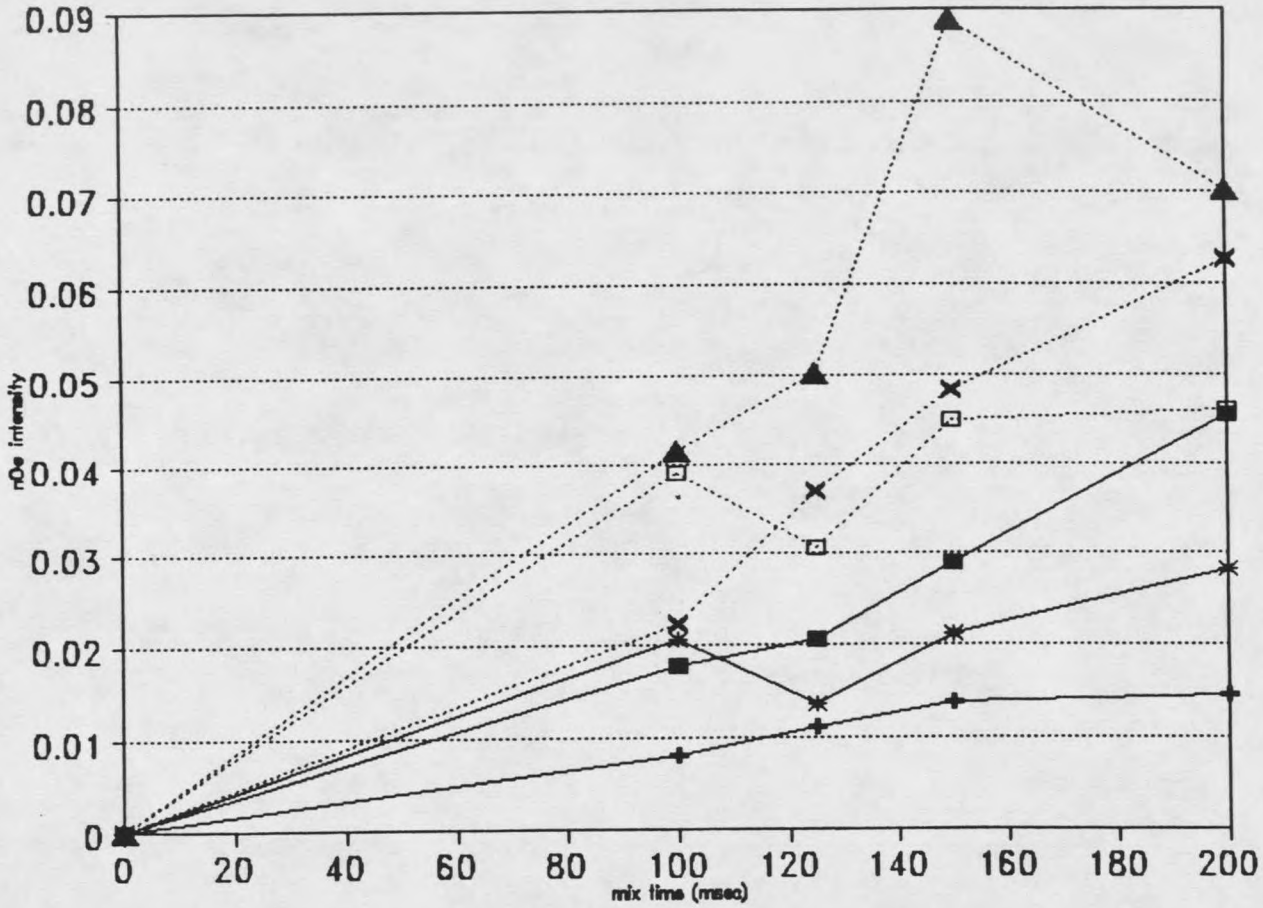


Figure 34. New NOESY cross-peaks observed per amino acid for the peptide in both the dark-bound and light-bound forms. "Dark" cross-peaks were still observable in the light-bound spectra; "light" cross-peaks were only seen in the light-bound spectra.



Free: ■ = Asn NH - Glu αH ✚ = Gly NH - αH ✳ = Glu γH - βH
Light: □ = Asn NH - Glu αH ✖ = Gly NH - αH ▲ = Glu γH - βH

Figure 35. NOE build-up curves for the free peptide Ac-340-350 (K341R) and a 15:1 mixture of peptide and metarhodopsin II (light).

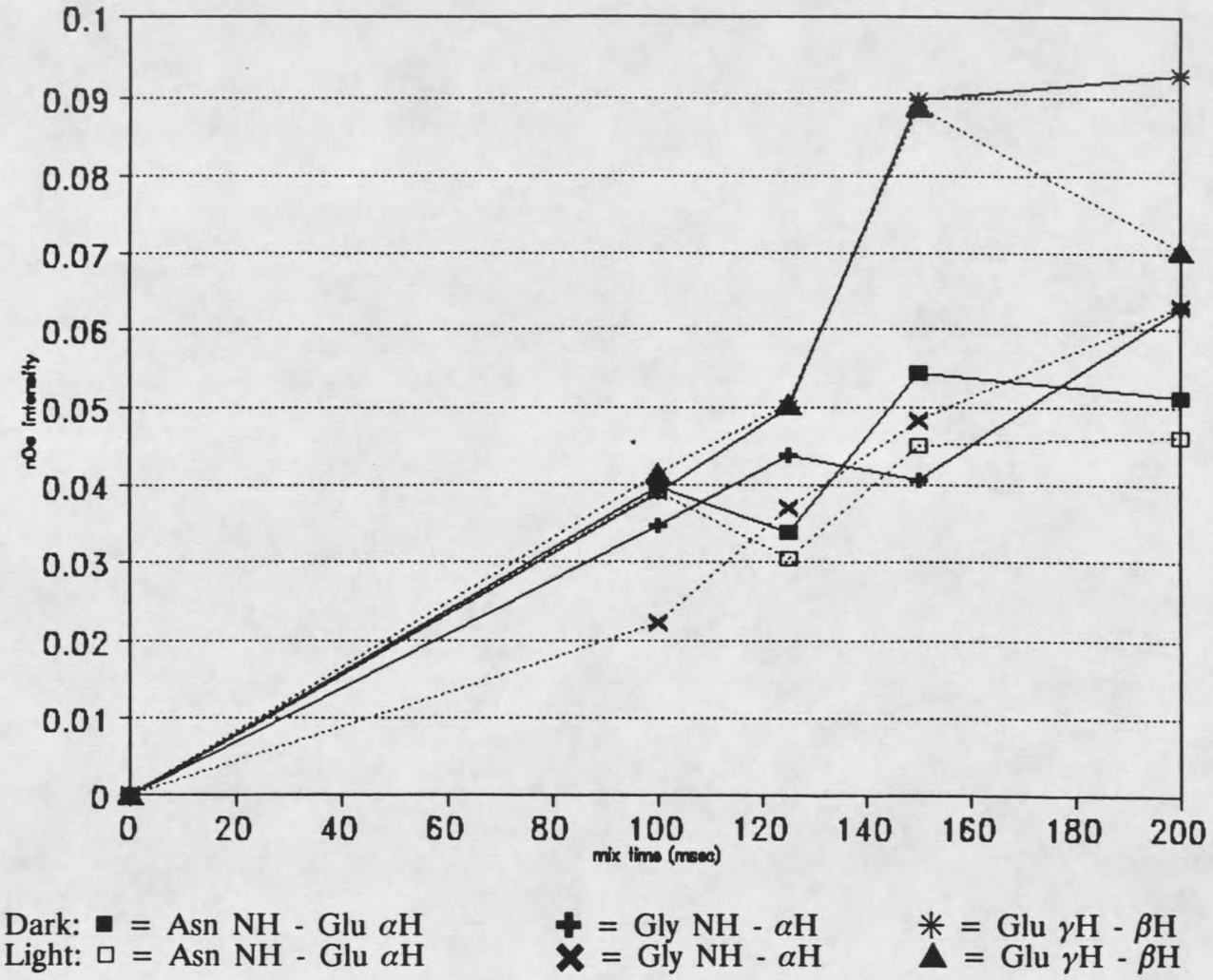


Figure 36. NOE build-up curves for a 15:1 mixture of Ac-340-350(K341R) and rhodopsin (dark) or metarhodopsin II (light).

Table 6. Values used to best fit experimental $R_{1\rho}$ vs ω_{SL} data (light-bound).

T_1^f = 0.490 sec	p_b = 0.01
T_2^f = 0.490 sec	p_f = 0.99
T_1^b = 0.043 sec	k_{ex} = 1500 sec^{-1}
T_2^b = 0.005 sec	$\Delta\omega$ = 170 Hz

T_2^b and a slightly faster k_{ex} in the light state. Because the fit to the data is not perfect, it is difficult to know if the change in the best fit exchange rate between the light and dark bound states is significant. The shorter, but rather poorly defined, T_2^b in the light-bound structure could be indicative of tighter binding with the protein: as the peptide is in stronger contact with the protein, it experiences more "protein-like" conditions, such as the shorter T_2 characteristic of the membrane immobilized large receptor molecule. These observations will be discussed further in chapter 5.

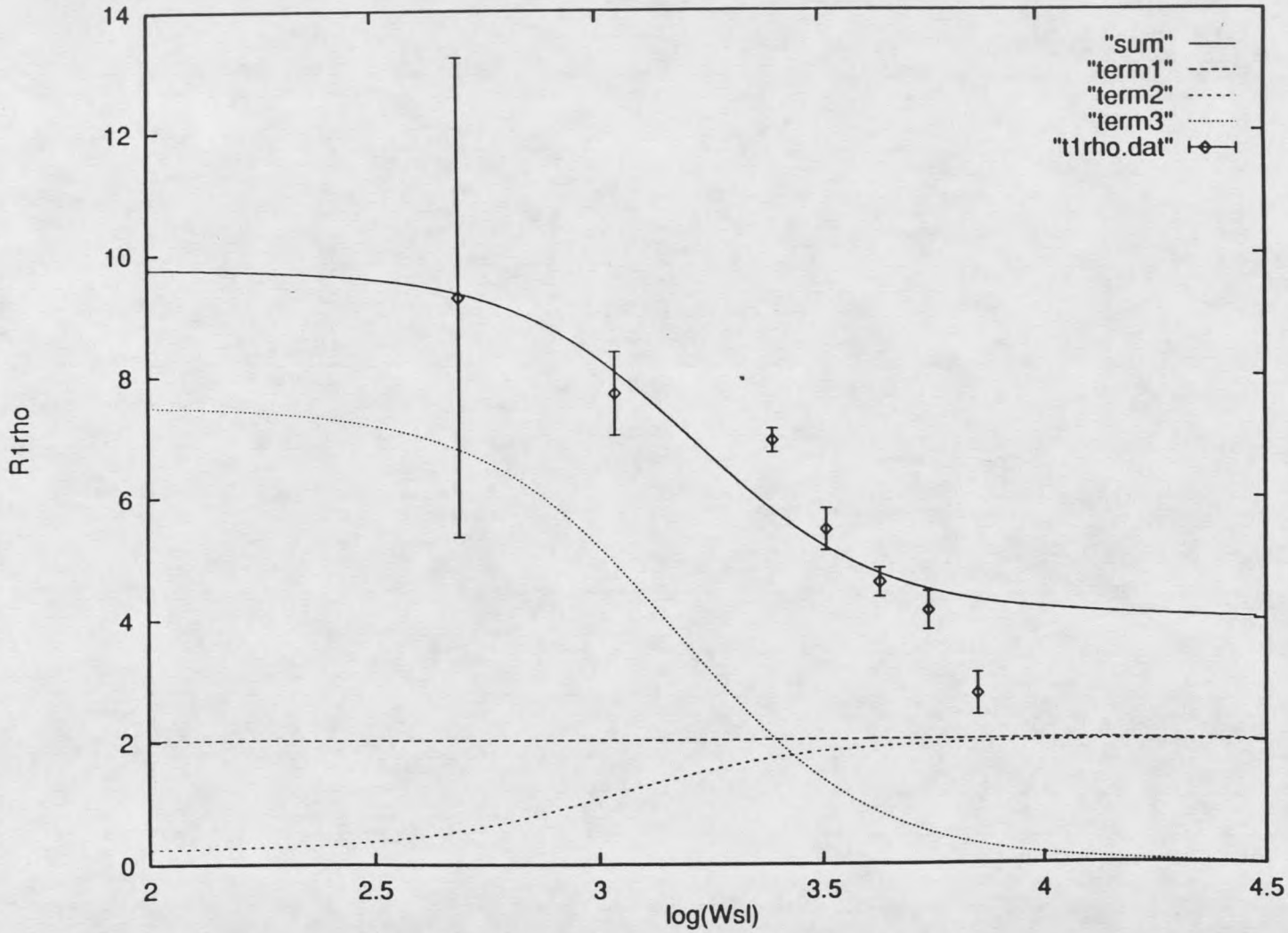


Figure 37. $R_{1\rho}$ vs. log (ω_{SL}) for a 15:1 mixture of peptide and metarhodopsin II (light).

CHAPTER 5

ANALYSIS AND COMPUTER SIMULATIONS

Initial Analysis of the 2D NMR Data

Once NMR data was obtained, it was converted to approximate distance constraints using several steps of processing. The types of manipulations carried out using the initial NMR distance constraints to develop initial approximate structures were energy minimization of initial structures to remove bad atomic contacts, molecular dynamics, and simulated annealing. The distances were refined using the approximate structures with the iterative steps with the distance refinement program MARDIGRAS. Each of these procedures was carried out on Silicon Graphics workstations (Indigo or Indigo^2) initially using the NOE constraints determined experimentally at a 100 msec mixing time to minimize the effects of spin diffusion on the NOE distances calculated (see the previous chapter's discussion of NOE build-up curves). In further calculations, structures were also assessed using data from TRNOESY experiments with longer mixing times.

Energy Minimization and Molecular Dynamics

The energy minimizaton and molecular dynamics procedures used were part of the Discover and NMRchitect packages of Biosym Technologies (50, 53). Figure 38 shows sample input file for a minimization and dynamics run. The run begins with the extended chain molecule, NOE constraints, chiral and dihedral restraints, and then performing 1000 steps of steepest descents minimization, followed by an additional 1000 steps of conjugate gradients minimization. For both the dark and the light structures, the same initial NOE data base that contained 71 cross-peaks was used; but the intensities of the cross-peaks varied in the dark and light structures. At this point, the structure was fairly well-minimized (derivatives in the minimization are less than 1.00 kcal/mol∘Å), and the dynamics portion was begun. In this phase, the dynamics of the molecule were simulated by the solving of the equations of motion for a system of atoms (53). The dynamics calculation includes a variable amount of random thermal energy which allows the molecule to cross energy maxima and was run at a speed where each frame recorded was equivalent to one femtosecond in real time. The molecule was first run through 50000 frames (50 psec) of dynamics at 300K to equilibrate it, and then the molecular coordinates for different dynamics frames began to be saved by the program. In order to maintain a well-minimized structure, the dynamics portion proceeded for 1000 frames (1 psec), and then the structure was re-minimized with 200 steps of conjugate gradients minimization. This procedure of dynamics then minimization was carried out for 30 cycles (30 psec) before the run

```
!    INPUT FILE FOR DISCOVER GENERATED BY INSIGHT
!
!

     overlap = 0.01

     begin simulation
*    add-automatic bond torsion valence out-of-plane
     reduce
!
     set dielectric  = 1.000000
     constrain
!
!
!

     Minimize
*    no cross terms
*    no morse
*    and no charges
*    for 1000 iterations
*    using steep descents
*    until the maximum derivative is less than 0.0010 kcal/A
     Minimize
*    no cross terms
*    no morse
*    and no charges
*    for 1000 iterations
*    using conjugate gradients
*    until the maximum derivative is less than 0.0010 kcal/A
!
!

     initialize dynamics
*    for 50000 iterations
*    at  300.000 K
*    steps of    1.000
*    no charges
*    no cross terms
*    no morse
*    write history  file every 1000 steps

     idx=1
2000 resume dynamics for 1000 steps at 300 K
*    steps of    1.00
*    no charges
*    no cross terms
*    no morse
     Minimize using conjugate gradients for 200 cycles
*    no morse
*    no cross terms
*    no charges
*    until the maximum derivatives is less than 0.001 kcal/A

     archive as file number idx
     idx = idx + 1
     if idx.le.30 then 2000
!
     end
```

Figure 38. A sample input file for a Discover minimization and dynamics run.

was completed. At the end of the run, thirty structures were available for further analysis. The total energy and energy derivative for each structure was read from the output file, and those structures with the lowest energy and the smallest derivative values, which also showed good agreement with the experimental NOE values, were used in further minimizations. The NMR data initially did not provide discrimination between several degenerate protons, nor in many cases were stereospecific assignments between those protons which were distinguishable in NMR (such as the β protons of the cystine residue). The structure produced by the first minimization and dynamics runs contained pseudo-atoms for the degenerate protons, and created initial arbitrary assignments for the sets of distinguishable α, β, and γ protons. The structure after dynamics is examined to see which proton of a pair would best satisfy the experimental NOE constraints. These test stereospecific assignments were then put into the restraint file used by the MD program, and the same cycles of minimization and dynamics as described previously were carried out. When completed, the structure with the lowest energy was then ready to be the starting point for simulated annealing with several stereospecific assignments selected.

Simulated Annealing

In the simulated annealing protocol (53), a model starting structure was taken, along with the restraints generated by the NOE data, and exposed to higher temperatures (1000 K) and much lower repulsive forces. The simulated annealing is designed to allow escape from false minima and to allow the molecule to experience a much wider range of conformations than it did under high barrier MD conditions kept

at 300K. Another feature of the simulated annealing protocol is that it allows the coordinates of the starting structure to be randomized at the beginning of each pass, if desired. This randomization of coordinates is designed to allow the structure to escape from false energy minima that it may have fallen into. The standard simulated annealing protocol provided in the NMRchitect software (53), as described briefly in chapter 1 (page 32), was used for both the dark-bound and light-bound structures, and in both cases twenty structures were generated.

Refinement of the Dark-Bound Structure

Discover Analysis

At the conclusion of each simulated annealing run, the twenty structures generated were overlapped and their backbone atoms compared for RMS deviations. Figure 39 shows the superposition of the backbone atoms (along with a "ribbon" so that the backbone is easier to follow) for the twenty structures generated in a dark-bound SA run. As for all structures shown in this chapter, the computational results were obtained using software programs from Biosym Technologies of San Diego and graphical display using *Insight II*. These structures do not show a very close agreement with each other, and so further analysis was carried out. As a part of the "Analysis" package of *Discover*, utilities are supplied that allow structures to be superimposed on a given structure and the RMS deviation of each structure to the reference calculated. Table 7 shows the RMSD comparison output for the superposition of the SA generated structures, using the first structure of the run as the

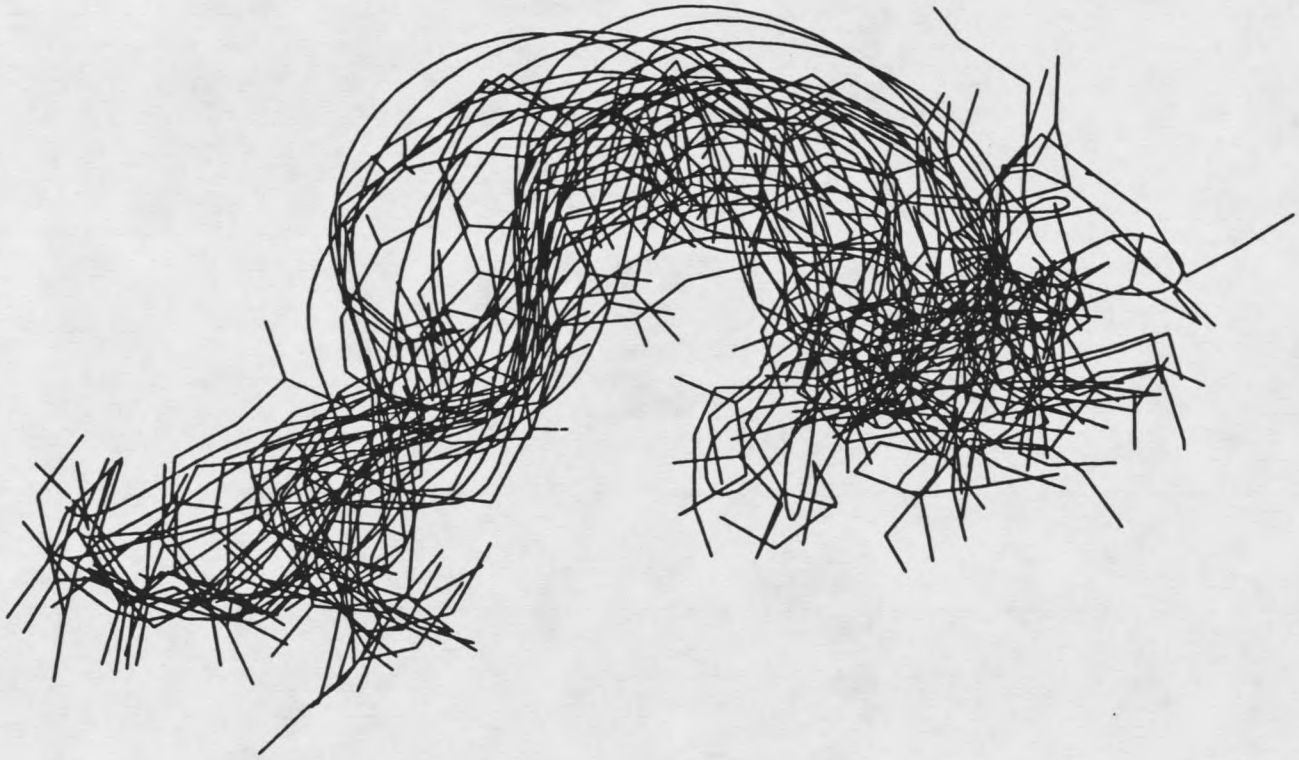


Figure 39. Superposition of the twenty dark-bound structures generated by a simulated annealing run.

Table 7. Simulated Annealing Results: Backbone atom RMSD agreement between the first SA generated dark-bound structure ("dark5test1") and the other SA generated structures.

```
backbone RMSDs between dark5test1 .. dark5test20 and dark5test1:

            dark5test1
dark5test1   0.000
dark5test2   3.012
dark5test3   1.845
dark5test4   3.913
dark5test5   0.946
dark5test6   3.376
dark5test7   3.554
dark5test8   3.077
dark5test9   0.965
dark5test10  2.932
dark5test11  3.640
dark5test12  3.162
dark5test13  3.056
dark5test14  3.989
dark5test15  2.580
dark5test16  3.836
dark5test17  3.249
dark5test18  0.764
dark5test19  3.676
dark5test20  2.944

Average pairwise RMSD:  2.72593  +/-  0.925437.
```

template. In this case, the structures that agree, within an arbitrarily chosen RMSD value of less than 2.00 Å, with the first structure are numbers 3,5,9, and 18. These structures were then considered to be a "family" or "cluster" of structures, and the superposition of these structures are shown in Figure 40. Similar analyses were carried out for each of the remaining structures, with several different families of structures being found. This is an approximate method of an approach called "cluster analysis." Table 8 summarizes the relationships observed, including the energy range of the structures in each family.

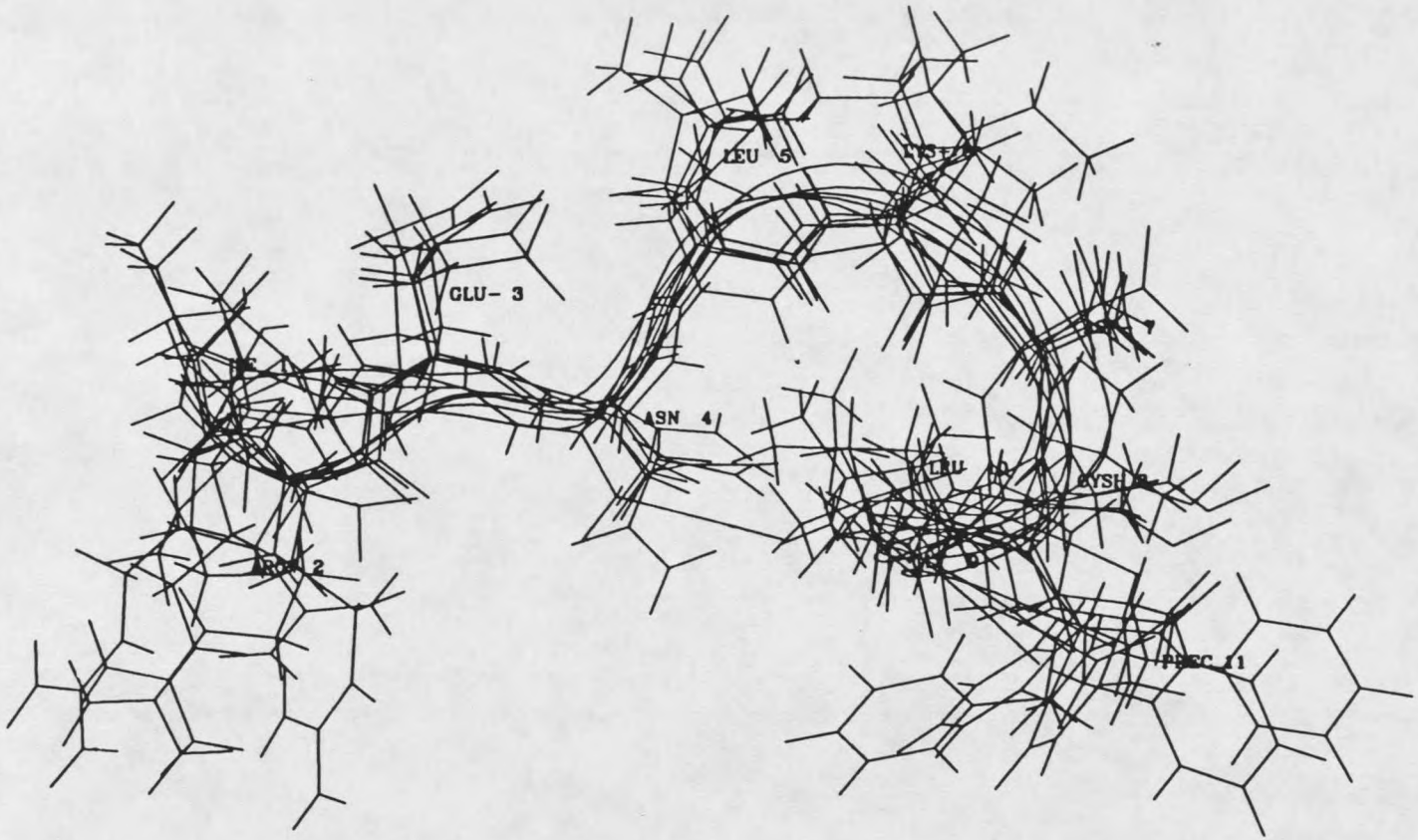


Figure 40. Superposition of five dark-bound structures (numbers 1, 3, 5, 9, 18) generated by a simulated annealing run.

Table 8. Simulated Annealing Results: Structure number vs. Total energy (dark).

SA Structure Family	Total Energy Range (kcal/mol)
1, 3, 5, 9, 18	657 - 741
2, 20	677 - 711
6, 8	721 - 739
7, 14	688 - 752
19, 4, 11, 16	652 - 734

As shown in Table 7, structures 10,12,13,15 and 17 showed no RMSD agreement of less than 2.00 Å with any other structure, and were therefore not considered for further analysis. Figures 41 through 44 show the superposition of structures for the other four different families shown in Table 8. It can be seen that these structures are in some cases quite different, but that the energy range of each family is similar (Table 8). All structures fit the experimental NOE constraints to a reasonably low degree of error (see Table 9), and so it is clear that some aspects of the structure were not well defined for the short NOESY experiments employed.

Table 9. Simulated Annealing Results: Structure number vs. NOE violations (dark).

Structure #	NOE violations > 0.1 Å	max. NOE violation (Å)
1	11	-0.82
2	12	-0.83
6	13	-0.83
7	12	-0.85
19	12	-0.81

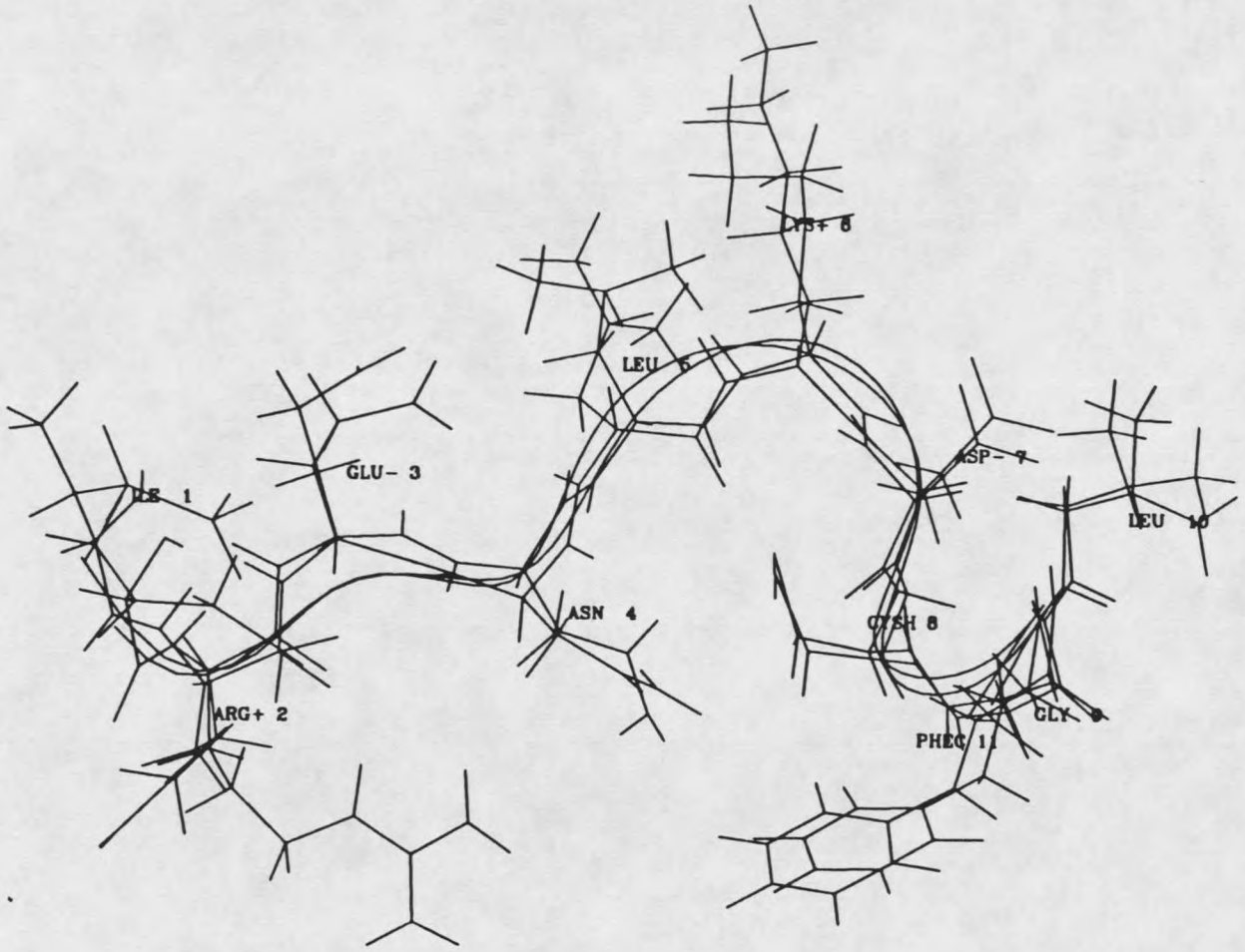


Figure 41. Superposition of two dark-bound structures (numbers 2, 20) generated by a simulated annealing run.

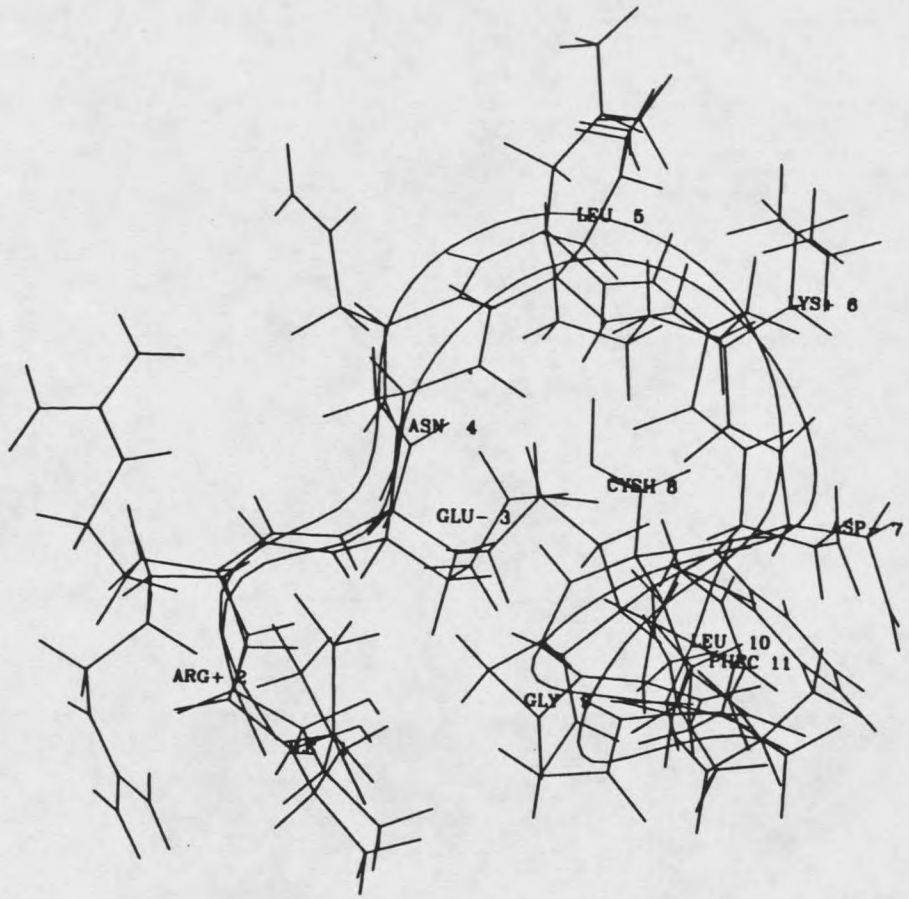


Figure 42. Superposition of two dark-bound structures (numbers 6, 8) generated by a simulated annealing run.

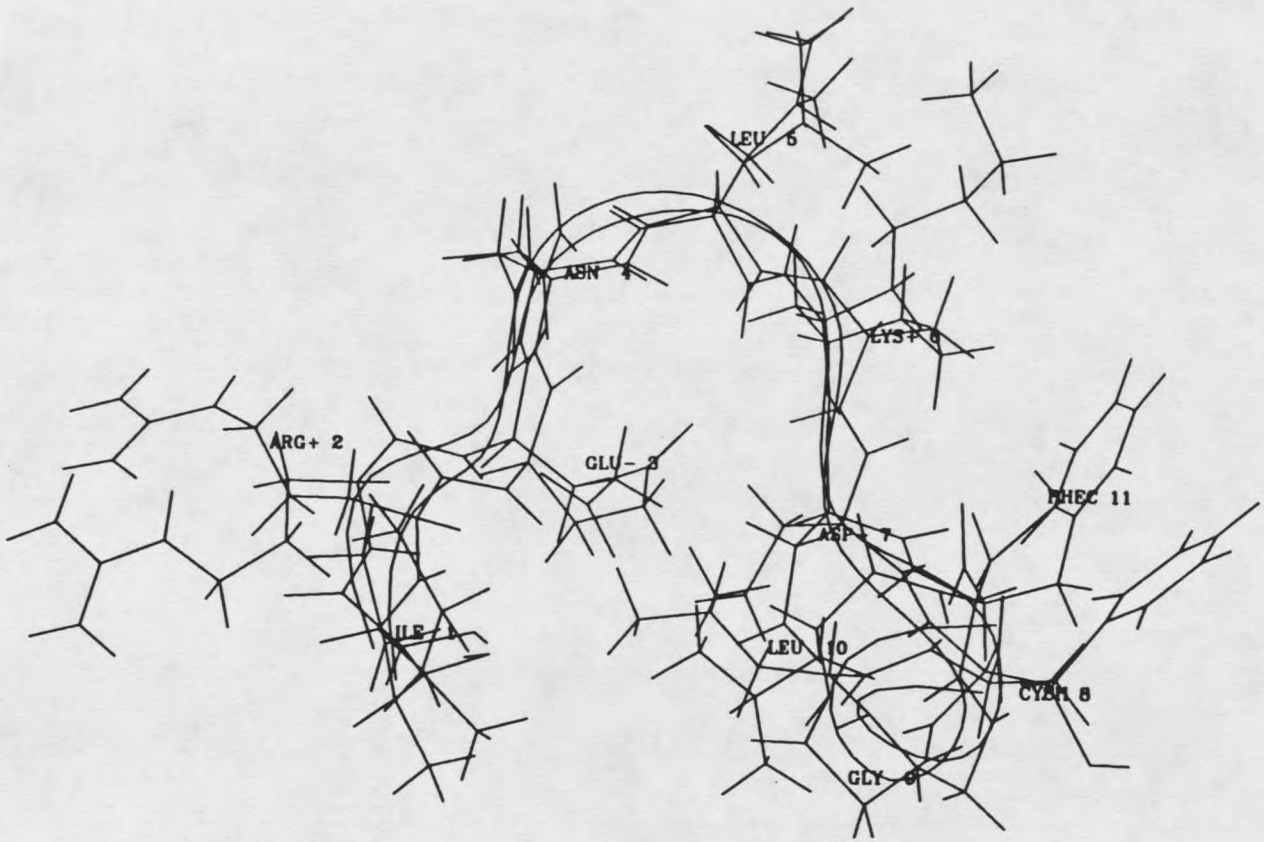


Figure 43. Superposition of two dark-bound structures (numbers 7, 14) generated by a simulated annealing run.

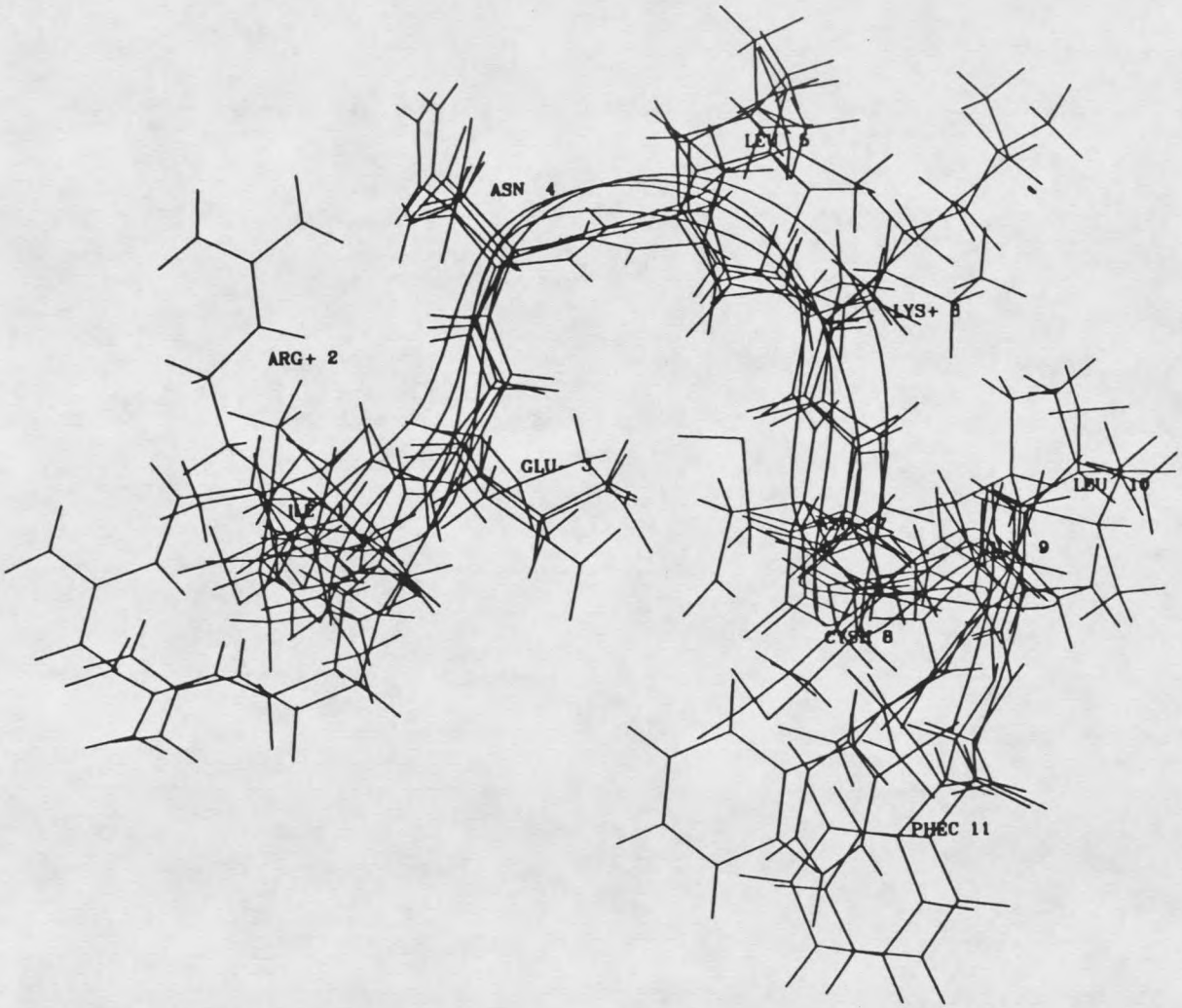


Figure 44. Superposition of four dark-bound structures (numbers 4, 11, 16, 19) generated by a simulated annealing run.

MARDIGRAS Refinement

When the five dark structure families were determined, one structure from each family (structure number 1,2,6,7, and 19) was used as starting structures in MARDIGRAS distance refinement (55). The MARDIGRAS program generates a theoretical 2D NOE (or transfer-NOE) spectrum based on the approximate geometry of a trial structure and the experimental NOESY intensities (see discussion in chapter 1, pages 32 - 34). The MARDIGRAS program is used to account for multispin effects and to overcome errors in the isolated two-spin approximation used for conversion of NOE intensities to distances. The effects of the other spins in the system can be accounted for by MARDIGRAS once approximate structures are available. The approximate structures are used to calculate all interproton distances for a complete relaxation matrix back-calculation of the NOESY. The complete relaxation matrix shows the influence of all interproton relaxation pathways on the two-spin distance of interest and allows a more accurate set of distances to be derived. Once the more accurate distances are obtained, MARDIGRAS is iterated to get the best set of distances given the approximate structure used in the current cycle of refinement. The better MARDIGRAS derived distances are used in cycles of molecular dynamics to obtain improved structures. The improved structures are used to repeat MARDIGRAS, and the process is iterated until the distances converge.

When the MARDIGRAS calculation is carried out, several files are written that allow comparison of the theoretical spectrum with the observed data. The most important of these is the *.BNDS file, which contains the final distance constraints

calculated by MARDIGRAS including error bars on the distance constraints which provide some measure of assessment of errors. This file can then be converted to a restraint file that can be read into the Biosym software, so that additional MD runs can "smooth" bad energy values that have occurred in MARDIGRAS and a structure of the molecule may be displayed. Several programs were written by David Poole (in the MSU Department of Chemistry and Biochemistry) to assist in the analysis of the structures generated by MARDIGRAS and MD. One of these, "rmsnoe" compares the RMS deviations of the MARDIGRAS/MD generated structures with the experimental NOE data. By selecting structures with low RMS deviations, along with low total energies, one or more new, refined structures can be selected for further MARDIGRAS analysis. This procedure can be followed iteratively until the MARDIGRAS R and Q factors converge (see page 34) and little further change is seen in the distances generated in the .BNDS file.

MARDIGRAS calculations were carried out on each of the five dark starting structures obtained from the SA structure analysis using a variety of effective correlation times. These results are summarized in Table 10. Although the τ_c^{eff} of 1 nsec has the lowest R and Q factors, it is rejected because it produces distances in the MARDIGRAS analysis that are unreasonably short (many NOE distances were 1.5 Å or less). Shorter τ_c^{eff} values gave even more unreasonable distances. Increasing τ_c^{eff} to 2 nsec gives much more reasonable distances, but slightly poorer R and Q factors. A "good" correlation time may give poorer R and Q factors if the trial structure has not yet converged to the "best fit" structure. The best fit τ_c^{eff} is probably greater than

1 nsec and less than 2 nsec.

It should also be noted that, in the course of a MARDIGRAS calculation, distances in the experimental NOE data file can be rejected for several reasons. The first of these is if MARDIGRAS is unable to assign a new relaxation rate to an observed intensity. According to the authors of MARDIGRAS, this seems to occur when "the model is poor over a region which is underdetermined by experimental data - the resulting inconsistencies may cause physically meaningless rates to appear" (55). MARDIGRAS will also reject distances where the relaxation rate is very small, so that the corresponding distance is 5Å or greater, due to a high level of uncertainty (55). For both the dark- and light-bound systems, the problem of underdetermined data seems to be a factor. Since the NOESY runs were very short (≈ 4 hours), there are relatively few NOEs (≈ 70), and after MARDIGRAS only 50 distances remained in the .BNDS file. In both cases, the NOEs that were lost were primarily distances within amino acid sidechains, from 54 used in the SA analysis to 32 that remained after MARDIGRAS in the dark structure. The side chains which are showing large TRNOESY signals are presumably interacting rather strongly with the protein. A possible explanation of why the side-chain NOEs were rejected by MARDIGRAS is that the protein bound side chains may have a longer correlation time than the backbone of the peptide, which might have some flexibility while bound to the receptor. Fitting models with more than one correlation time were not pursued, but the "model free" approach of Lipari and Szabo (102) would allow different motional constraints at different sites using a minimum number of additional parameters.

Table 10. MARDIGRAS R and Q factors vs. τ_c^{eff} (dark).

τ_c^{eff}	R factor	Q factor
0.8 nsec	0.249	0.138
1.0 nsec	0.158	0.084
2.0 nsec	0.236	0.110

The .BNDS file for each structure was converted into a restraint file, and the five structures were run through a molecular dynamics calculation, each MD run producing 20 structures in the end. Each of these runs was analyzed for RMS agreement with the NOE data and overall energy of the structure. From these sets of structures, seven structures showing good NOE agreement and low energy were selected, and the MARDIGRAS calculation was once again carried out at several different correlation times. The best agreement with the NOE data was noted, the resulting .BNDS files from these MARDIGRAS runs were once again converted to restraint files, and molecular dynamics run. At the end of these runs, the structures fell into three basic groups. One structure from each group was selected to undergo an additional round of MARDIGRAS and MD, and the best structure of each result was compared. These structures did not show any significant changes, nor any better agreement with each other, so further refinements were not attempted. The superposition of these three structures is shown in Figure 45, and Table 11 gives NOE distances for selected representative protons over the course of the MARDIGRAS and MD iterations.

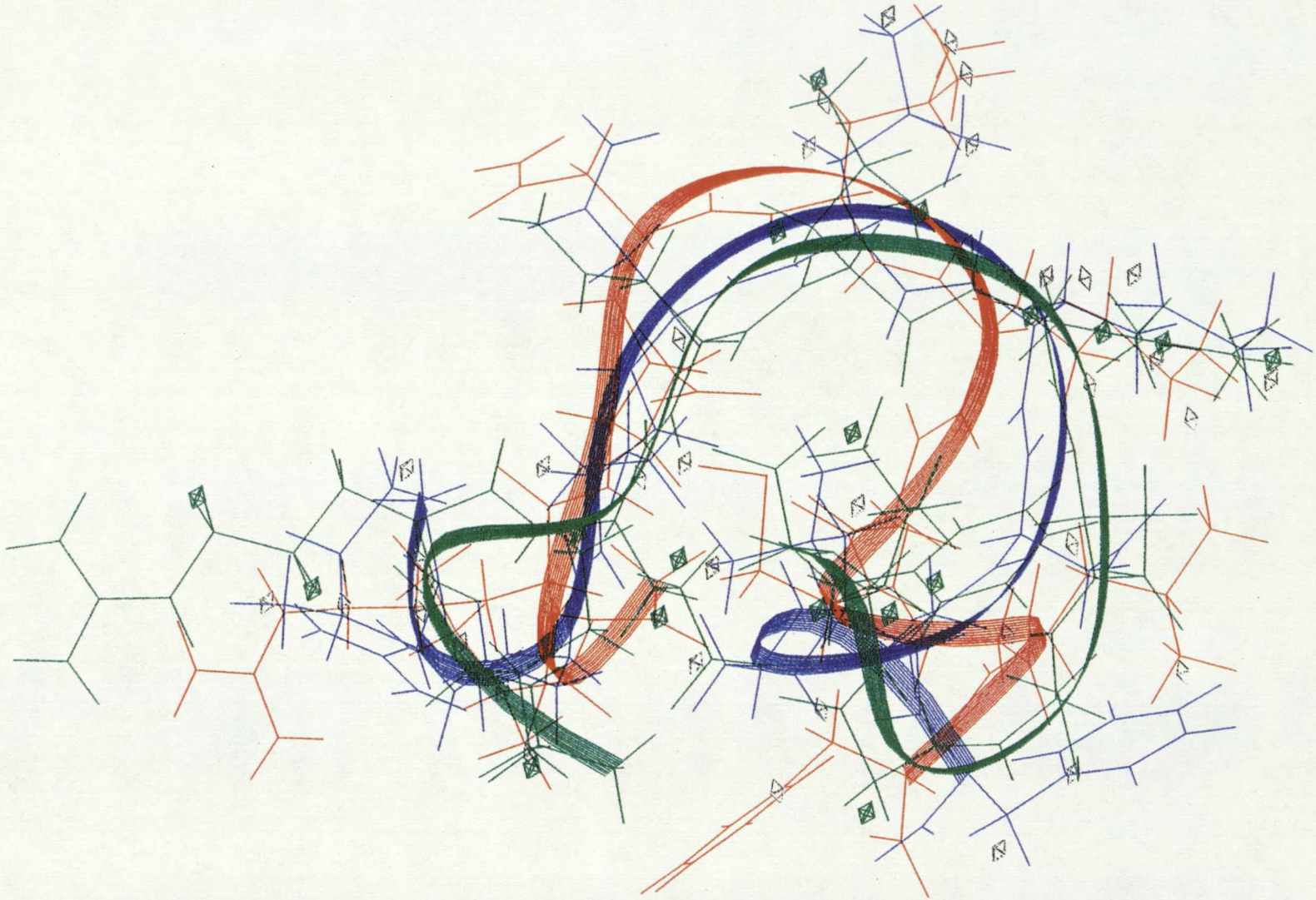


Figure 45. Superposition of one structure of each of the three groups of dark-bound structures after three rounds of MARDIGRAS and MD calculations.

Table 11. Selected "dark" NOE distance restraints (lower limit) throughout the course of MARDIGRAS and molecular dynamics iterations starting from SA generated structure #1. "Initial Value" is the distance restraint after the SA run; "Round 1" refers to distances generated after one round of MARDIGRAS; "Round 2" distances are those generated after a MD run followed by a second round of MARDIGRAS; "Round 3" distances are after a second MD run and a third round of MARDIGRAS.

Proton pair	Initial Value(Å)	Round 1 (Å)	Round 2 (Å)	Round 3 (Å)
Leu 5 HN-Hα	1.79	1.46	2.01	2.01
Lys 6 Hβ*-Hγ*	2.00	2.14	2.70	2.72
Leu 10 HN - Gly 9 Hα*	2.51	2.34	3.05	3.06
Phe 11 HN - Gly 9 HN	2.08	1.58	2.27	2.28

Refinement of the Light-Bound Structure

Discover Analysis

As for the dark-bound structure, twenty structures were generated through simulated annealing for the light-bound state, with the superposition of these structures shown in Figure 46. These structures were compared for RMS deviations, and the families that occurred are summarized in Table 12. For the light-bound data, structures 3, 12, 14, 16 and 20 show no RMSD agreement of less than 2.00 Å, and were not considered further in the analysis of the data. The superposition of the three families of structures is shown in Figures 47 through 49. Again, the structures show differences, but all fit the observed NOE constraints as shown in Table 13.

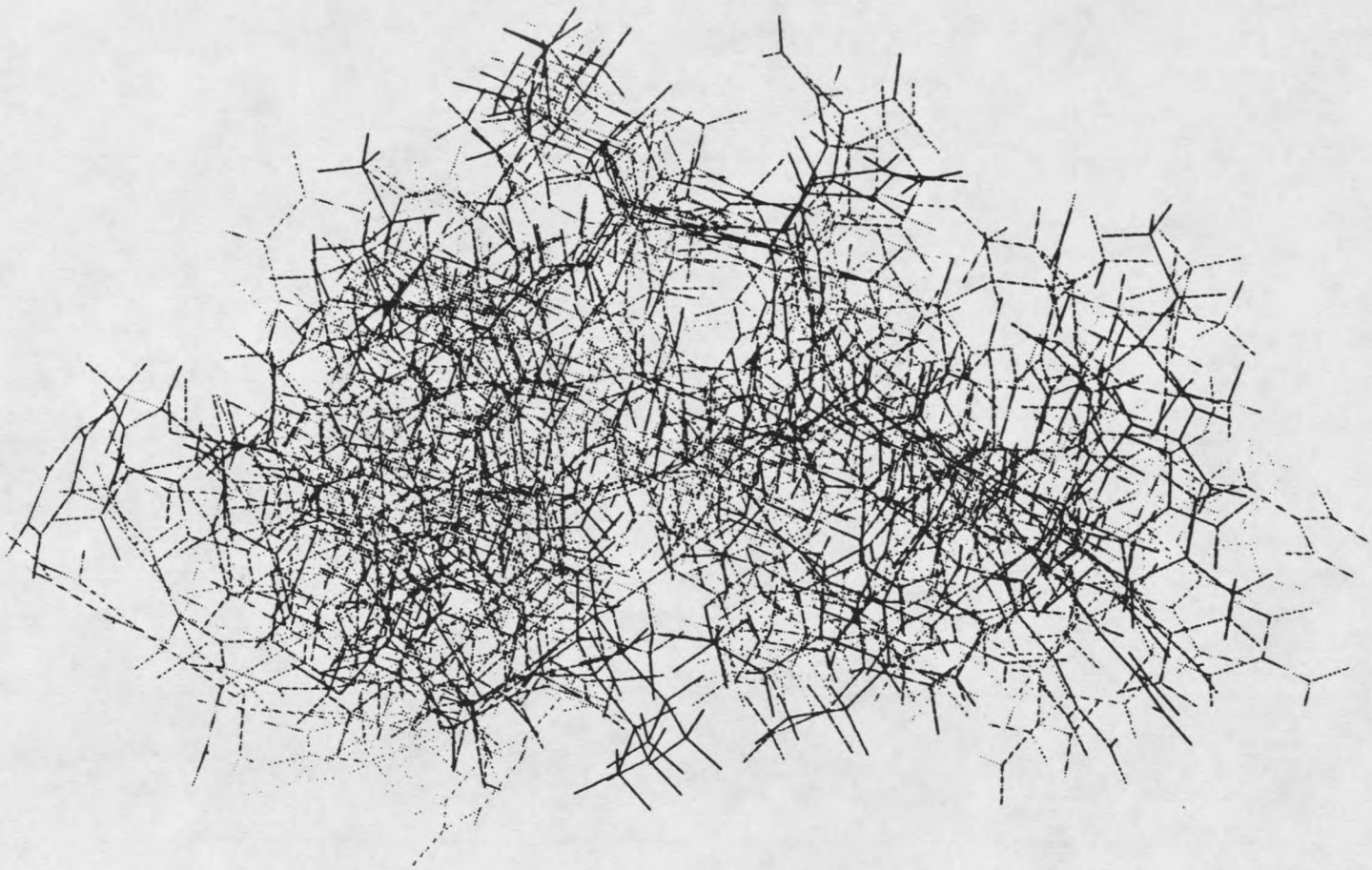


Figure 46. Superposition of the twenty light-bound structures generated by a simulated annealing run.

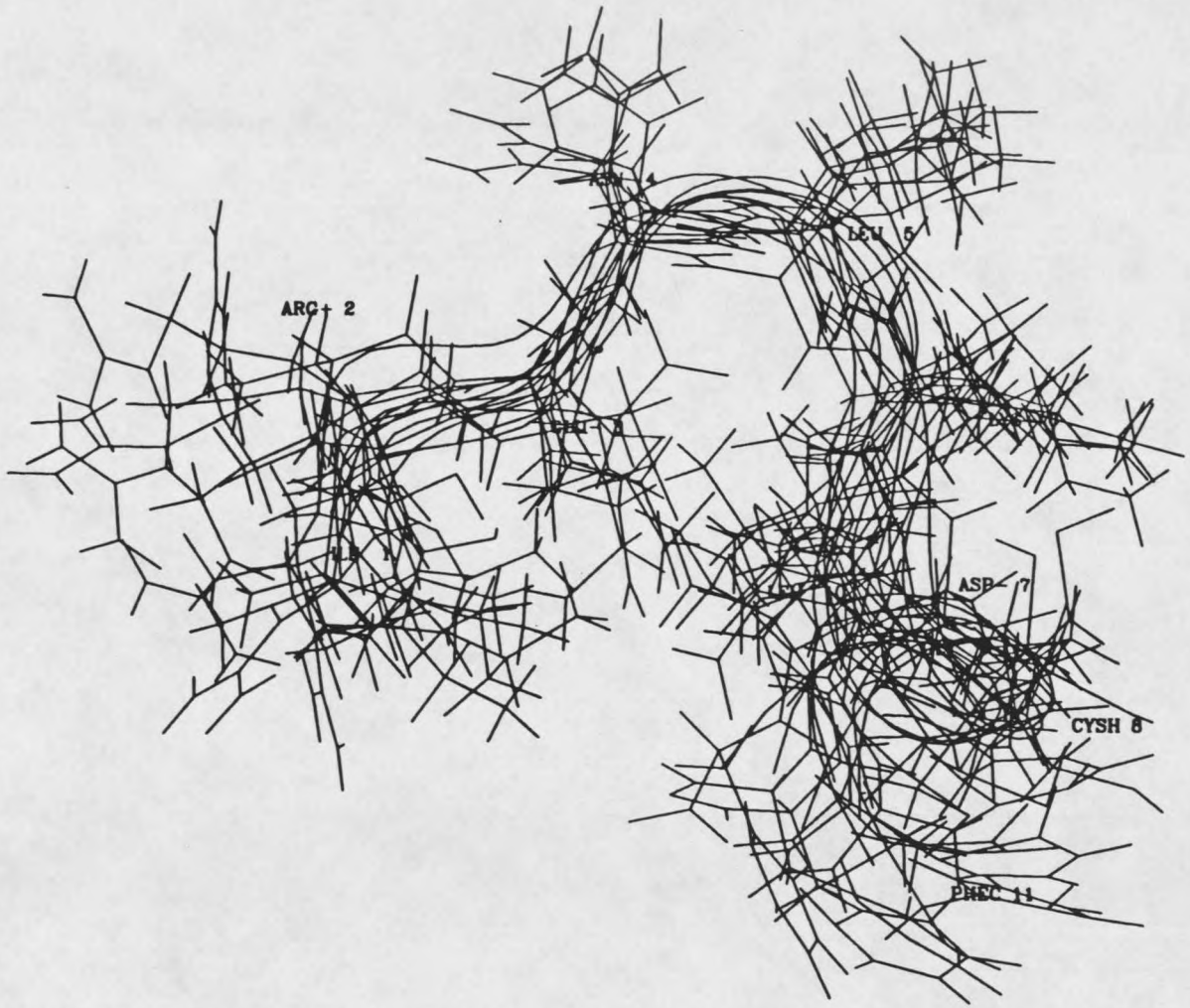


Figure 47. Superposition of seven light-bound structures (numbers 1, 4, 6, 7, 10, 15, 19) generated by a simulated annealing run.

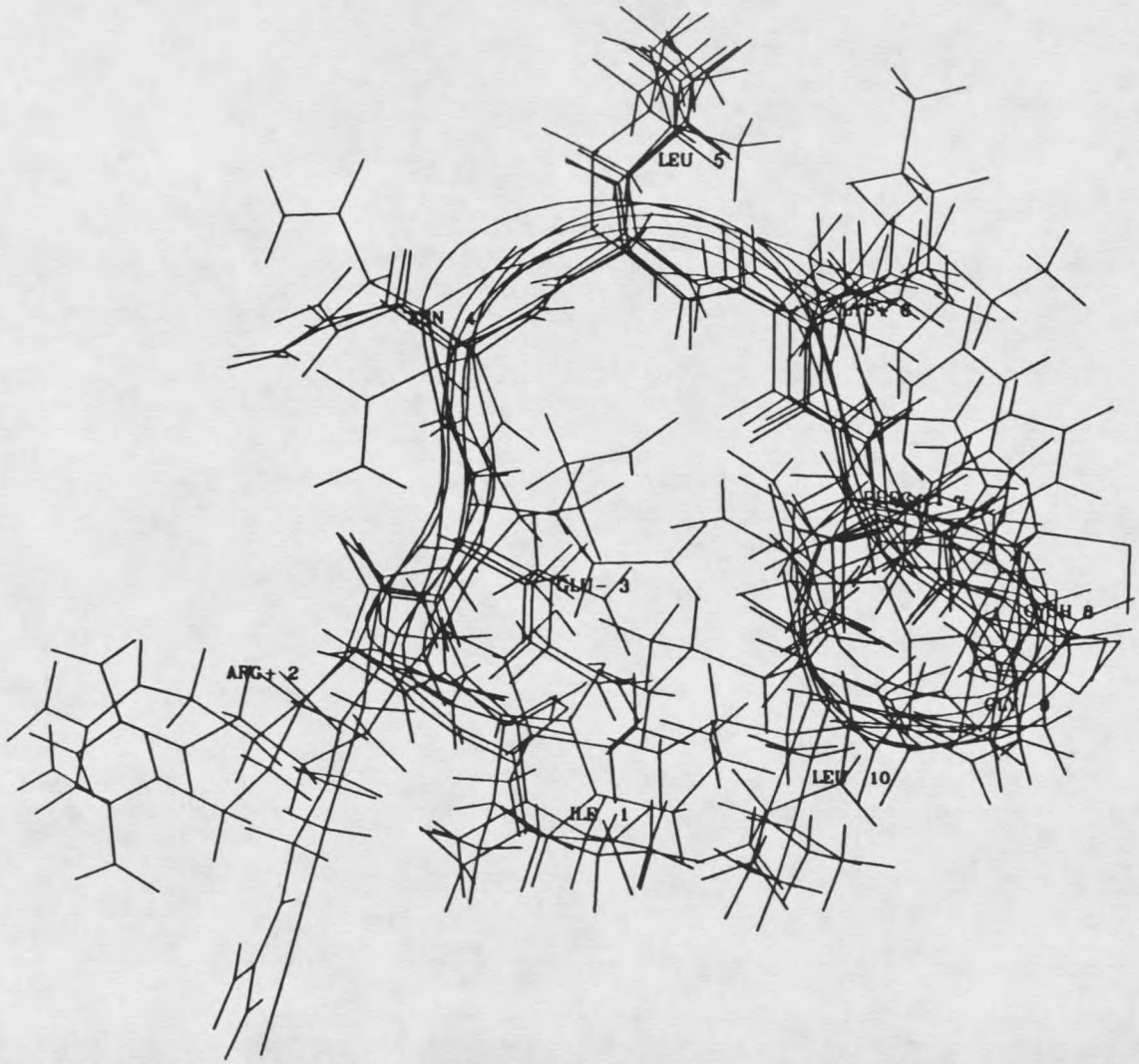


Figure 48. Superposition of five light-bound structures (numbers 2, 8, 11, 13, 18) generated by a simulated annealing run.

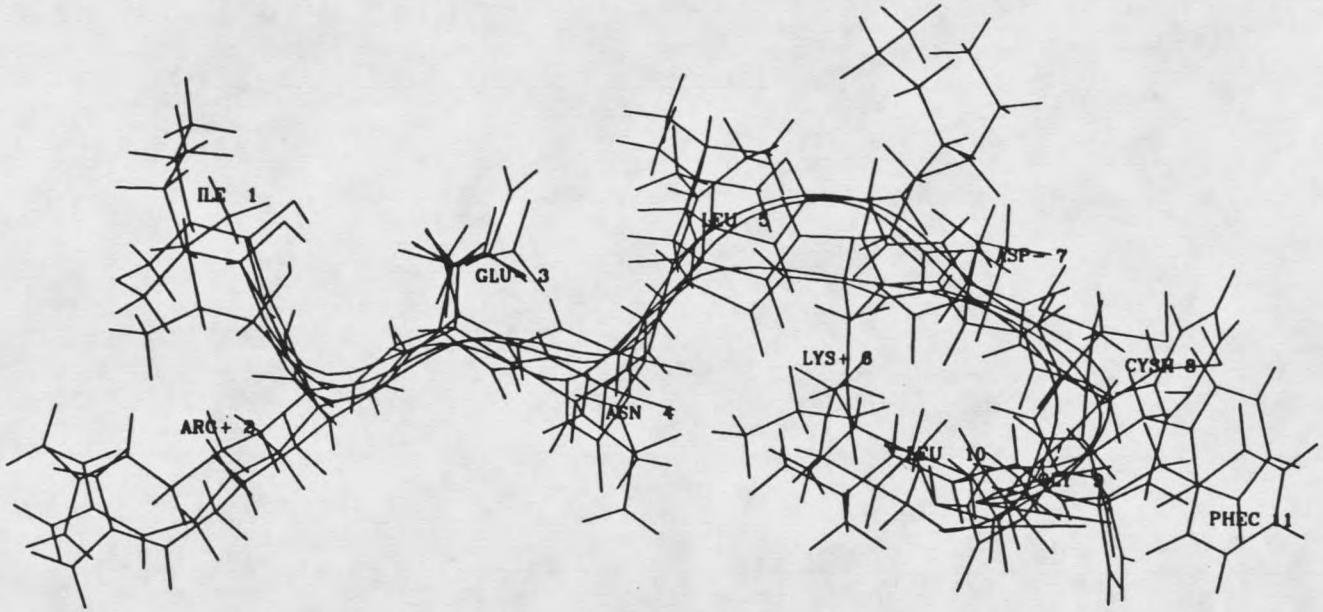


Figure 49. Superposition of three light-bound structures (numbers 5, 9, 17) generated by a simulated annealing run.

Table 12. Simulated Annealing Results: Structure number vs. Total energy (light).

SA Structure Families	Total Energy Range (kcal/mol)
7,1,4,6,10,15,19	368 - 530
8,2,11,13,18	386 - 471
17,5,9	449 - 503

Table 13. Simulated Annealing Results: Structure number vs. NOE violations (light).

Structure #	NOE violations > 0.1 Å	max. NOE violation (Å)
7	6	±0.19
8	5	-0.17
17	9	±0.22

MARDIGRAS Refinement

Again, one structure from each of the light bound families (structure number 7, 8, and 17) was used as a starting point for the MARDIGRAS calculation. Again, the effective correlation time was varied and the resulting R and Q factors were analyzed. Approximately twenty sidechain NOE distances were again rejected in the MARDIGRAS calculation. As previously discussed for the dark-bound system (p. 89-90), this is thought to be due to differing motional restrictions for the sidechain versus the backbone protons. The possible significance of these NOE distances will be

addressed further in the Discussion and Conclusions. For these structures, an effective correlation time of 0.7 nsec gave the lowest R and Q factors (Table 14), along with reasonable distance restraints in the .BNDS files.

Table 14. MARDIGRAS R and Q factors vs. τ_c^{eff} (light).

τ_c^{eff}	R factor	Q factor
0.7 nsec	0.550	0.221
0.8 nsec	0.609	0.237
1.0 nsec	0.683	0.256
2.0 nsec	1.038	0.342

This provides an interesting comparison between the dark and light bound states of the peptide - a significantly different effective correlation time (between 1 and 2 nsec for the dark-bound vs. 0.7 nsec for the light-bound peptide). Since the effective correlation time is the product of the true correlation time and the percent of bound peptide ($\tau_c^{eff} = P_b \tau_c^{true}$), one of two things could be occurring. If P_b remains constant, then the true correlation time of the light-bound peptide must be shorter than that of the dark-bound peptide (70 vs 150 nsec, if 1% binding is assumed). Physically, there seems to be no reason to believe that the true correlation time of the light bound peptide should get shorter, since the peptide and protein do not change molecular weights in the light or the dark. If one assumes alternatively that the true correlation time is constant, this would imply that there is a different percentage of bound peptide in the dark and light states, with the percent bound in the light state being the lower value. A possible explanation of this would be if the conversion of

rhodopsin to MII is less than 100 % and/or that some of the MII goes to MIII or other species during the time period of the NMR experiments. If the effective p_b of the light bound state is approximately 50 % of the dark state, this would be a plausible explanation of the data. Another possibility is that the binding of the peptide to the dark adapted rhodopsin is less specific than the binding to MII. This could allow more conformations of the peptide to bind in the dark, possibly giving a higher p_b in the dark vs the light. When the protein is bleached to its MII form, there is now probably only one specific binding site, and not all of the rhodopsin is in the MII form, therefore a lower percentage of peptide is able to bind in the light stimulated case. However, in other studies in the Dratz laboratory, the structure of the dark-bound peptide is being further refined using a much larger data set. It is possible to obtain many more NOE distances in long 2D NOESY and 3D NOESY/NOESY runs in the dark-bound state. The dark-bound refinement is still underway, but it appears that the dark-bound structure is quite well-defined by the additional data. Other studies in the Dratz laboratory have also shown that specific changes in the peptide sequence that abolish activity also abolish TRNOESY cross-peaks. Therefore the dark-bound state does seem to be specifically bound. Further studies are needed with mutant peptides, which are inactive, to investigate the possibility of non-specific binding in the dark and the light.

After the first round of MARDIGRAS, six light-bound structures were selected and run through molecular dynamics. Each of these six runs generated twenty structures, which were analyzed for NOE RMS agreement and total energy. This gave

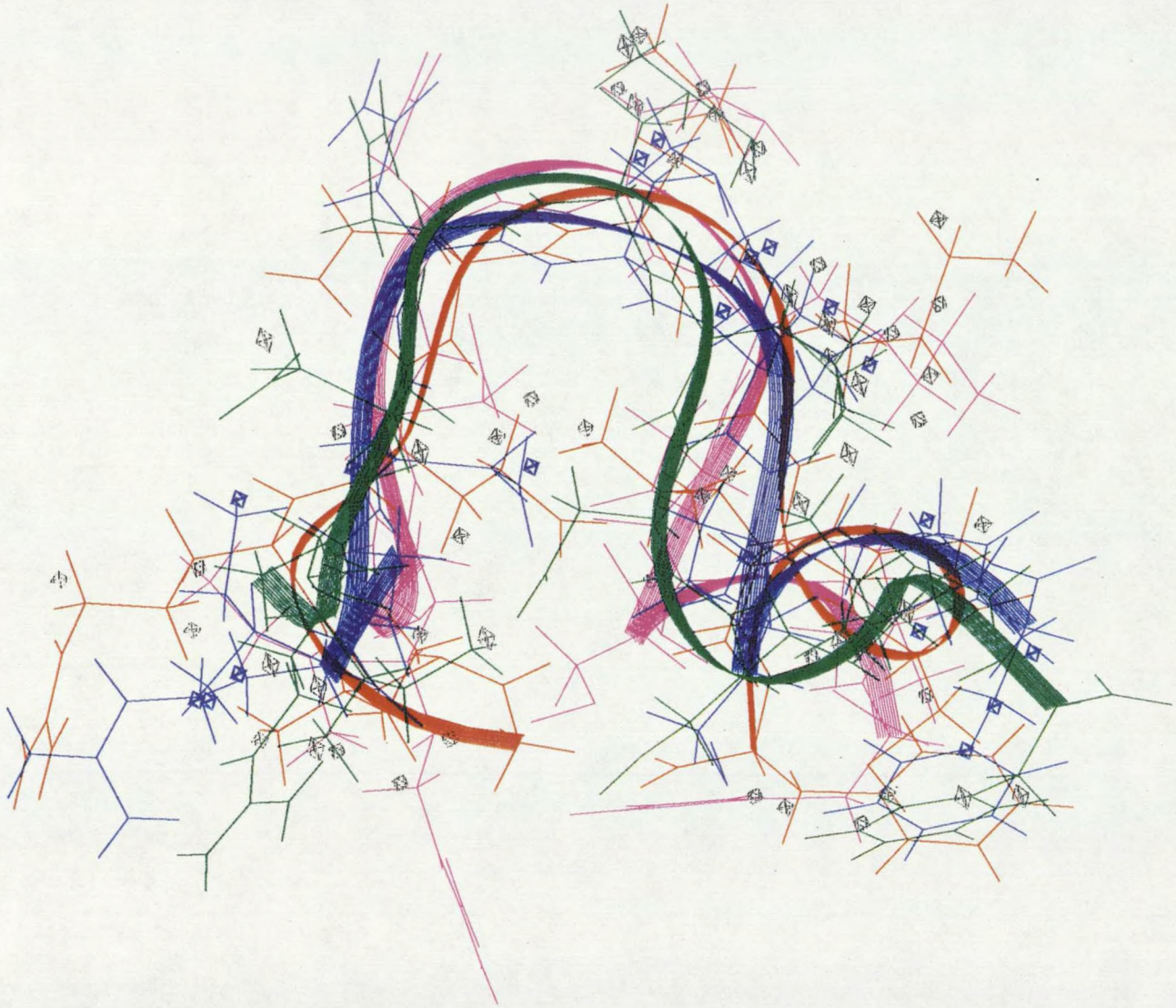


Figure 50. Superposition of one structure of each of the four groups of light-bound structures after three rounds of MARDIGRAS and MD.

nine structures that were used in the next round of MARDIGRAS/MD. Again, this iterative process was carried out for four rounds, until the NOE distances no longer changed significantly (Table 15). After this final iteration, four representative structures were selected, and the superposition of these structures is shown in Figure 50.

Table 15. Selected "light" NOE distance restraints (lower limit) throughout the course of MARDIGRAS and molecular dynamics iterations starting from SA generated structure #17. "Initial Value" is the distance restraint after the SA run; "Round 1" refers to distances generated after one round of MARDIGRAS; "Round 2" distances are those generated after a MD run followed by a second round of MARDIGRAS; "Round 3" distances are after a second MD run and a third round of MARDIGRAS.

Proton pair	Initial Value(Å)	Round 1 (Å)	Round 2 (Å)	Round 3 (Å)
Leu 5 HN-Hα	1.93	2.11	2.02	2.09
Lys 6 Hβ*-Hγ*	2.21	2.21	2.15	2.13
Leu 10 HN - Gly 9 Hα*	2.62	3.01	2.87	2.86
Phe 11 HN - Gly 9 HN	2.35	1.87	2.01	1.93

Discussion and Conclusions

The data and structures obtained lead to several interesting comparisons. As noted previously, the NOE build-up rates were quite similar for the dark- and light-bound experiments (Figure 36), although significantly more cross-peaks were observed in the light-bound experiments. The new cross-peaks were mainly from sidechain interactions and interactions on the C-terminal end of the peptide, as shown in Figure

34. This data may be important in suggesting peptide mutations in future work, although many of these sidechain distances were rejected by the initial MARDIGRAS analysis described here. The sidechain cross-peaks suggest more intimate binding in the light, and the increase in C-terminal cross-peaks suggests that this end is important in the light binding. The importance of the C-terminal end of the peptide in receptor coupling is supported by the chimeric G protein studies of Conklin et al (5). Data obtained in the peptide-protein exchange rates also suggests more intimate binding in the light state: T_2^b changing from 13 msec in the dark to 5 msec in the light (Tables 5, 6). This decrease in T_2^b is rather poorly defined by the data but is consistent with more intimate binding in the light state; as if the peptide is associated more intimately, it experiences more "protein-like" conditions, such as the shorter T_2 that is characteristic of larger molecules. The data on τ_c^{eff} used in the MARDIGRAS refinements (1-2 nsec for the dark, 0.7 nsec for the light) also may give insight into possible binding activity. The best explanation for the correlation time shift is the expected < 100% conversion efficiency to MII and a higher percentage of peptide bound in the dark than the light. The final structures obtained through MARDIGRAS are consistent with the idea of tighter binding in the light; the dark-bound structures qualitatively show weaker NOEs and less overall agreement with each other and with the NOE data than the light-bound structures.

At this point, the question should be asked "can anything be done to improve and further refine these structures?" Probably the largest factor that could be improved, from an NMR standpoint, is the length of the NOESY experiments

performed. The short NOESYs run on this system (NS = 32, NE = 256, total acquisition time ≈ 4 hours) do not give adequate signal-to-noise to get a very large number of weaker intensity NOEs or to obtain very strong cross-peak intensities. The longer range, weaker NOEs are especially important to define three dimensional structures. Work has been carried out and is still underway on the dark-bound system where much longer NOESYs can be run, where the stability of the peptide-protein complex is not an issue. With longer NOESYs, about 168 NOE cross-peaks have been measured in the dark-bound state (20) and about 450 are apparent in 3D NOESY/NOESY experiments (Dratz, personal communication).

For the light-bound structure, stability of the complex is the key to longer NOESY runs. Two ways have been proposed to get around this problem. First is to find peptides that stabilize MII for longer time periods. A possible substitution would be a second arginine for Lys 346, since the removal of the second lysine, if tolerated, would be expected to greatly stabilize MII (20). Professor Hamm had originally indicated that 340-350(K341R),(K346R) did not stabilize MII, but that seems to be an unwarranted conclusion (Hamm, personal communication to Prof. Dratz). In addition, the modified peptides can be investigated and examined for their biological activity. This has already been done in a number of cases involving Cys 347 and Gly 348, where substitution of a serine for the cystine, or alanine for the glycine has essentially abolished biological activity (20).

A second novel way to get around the problem of MII stability has been proposed (Dratz, personal communication) using site-specific rhodopsin mutants.

There are two classes of rhodopsin mutants of interest: (1) those that bind G protein upon bleaching and stabilize MII, but do not activate GTP exchange activity and (2) those that are constituatively active in the dark. The first class of mutants is predicted to produce a conformation close to that of the dark-bound peptide in the light-excited state, and the second class of mutants is predicted to produce a light-bound peptide conformation in the dark. If sufficient amounts of these mutants can be obtained (and this seems promising (Thurmond and Khorana, personal communication to Prof. Dratz; Oprian, personal communication to Prof. Dratz), these mutants should eliminate the problem of peptide-MII lifetime stability and allow for the longer NOESY runs desired.

Other avenues could be investigated to improve on these structures. One of these is the use of IRMA (Iterative Relaxation Matrix Analysis (97)) in the structure refinement process. IRMA uses a set of NOESY mixing time data in a single calculation, rather than a single mixing time as used by MARDIGRAS, and may yield better distance constraints. IRMA was tried by others in the laboratory with best estimates of bound correlation times (100-200 nsec), but the program would not work with such long τ_c. The use of an effective correlation time ($\tau_c^{eff} = p_b \tau_c^{true}$) may solve this problem as was done in MARDIGRAS. It is also likely that allowing for different local motions in the bound peptide sidechains vs the main chain would better model the data. Using the "model-free" approach of Lipari and Szabo (102), different order parameters could be introduced for sidechain protons, allowing retention of the sidechain NOEs now rejected in the MARDIGRAS refinements.

Recently, the three-dimensional structure of the retinal rod transducin Gα subunit in the GTPγS and GDP-bound forms were solved by x-ray crystallography (99, 100). The N-terminal end of the Gα subunit had to be removed to obtain crystals and the N-terminal end is implicated in rhodopsin interaction and interaction with Gβγ. The C-terminal end of Gα is disordered in two of the three molecules in the unit cell and poorly ordered in the third. In the most highly refined structures (100), the C-terminus is disordered after residue 342 or 343. Obviously, structural information such as we are developing in NMR experiments is needed on the precoupled (dark) and active (light) complex to begin to understand the mechanism of this crucial interaction. Closely related interactions are at the heart of a large fraction of cellular signalling systems.

In closing, this project has yielded preliminary structures for the metarhodopsin II bound (light) peptide segment $G_t\alpha$ Ac-340-350 (K341R). The quality of these structures is limited by the relatively short lifetime of the MII complex, and consequently weak intensity NMR NOESY data available. Work continues in this laboratory to better define these structures and yield further understanding of this protein interface, which is an important model for a large fraction of signal receptor - amplifier systems in biology.

REFERENCES CITED

REFERENCES CITED

1. Simon, M.I., Strathmann, M.P., and Gautam, N., Science, **252**, 802-808, 1991.

2. Gilman, A.G, "G Proteins: Transducers of Receptor-Generated Signals," *Annual Reviews of Biochemistry*, **56**, 615-649, 1987.

3. Hall, A., Science, **249**, 635, 1990.

4. Lochrie, M. and Simon, M.I., Biochemistry, **27**, 4957, 1988.

5. Conklin, B.R., Farfel, Z., Lustig, K.D., Julius, D., and Bourne, H.R., Nature, **363**, 274-276, 1992.

6. Tamir, H., Fawzi, A.B., Tamir, A., Evans, T., and Northup, J.K., Biochemistry, **30**, 3929-3936, 1991.

7. Hamm, H.E., Deretic, D, Arendt, A., Hargrave, P.A., König, B., and Hofmann, K.P., Science, **241**, 832-835, 1988.

8. Hamm, H.E. and Bownds, M.D., Biochemistry, **25**(16), 4512-4523, 1986.

9. Wald, G., J. Gen. Physiol, **19**, 351-371, 1935.

10. Wald, G., J. Gen. Physiol, **19** , 781-795, 1935.

11. Nathans, J., Biochemistry, **31**(21), 4923-4931, 1992.

12. Blazynski, C. and Ostroy, S.E., Vision Research, **21**, 833-841, 1981.

13. Dratz, E.A. and Hargrave, P.A., Trends in Biochemical Science, **8**, 128-131, 1983.

14. Fung, B.K.-K. and Stryer, L., Proceedings of the National Academy of Sciences, USA, **77**(5), 2500-2504, 1980.

15. Liebman, P.A., Parker, K.R., and Dratz, E.A., "The Molecular Mechanism of Visual Excitation and its Relationship to the Structure and Composition of the Rod Outer Segment," *Annual Reviews of Physiology*, **49**, 765-791, 1987.

16. Kibelbek, J., Mitchell, D.C., Beach, J.M. and Litman, B.J., Biochemistry, **30**, 6761-6768, 1991.

17. Fung, B.K.-K., Journal of Biological Chemistry, **258**(17), 10495-10502, 1983.

18. Fung, B.K.-K., and Nash, C.R., Journal of Biological Chemistry, **258**(17), 10503-10510, 1983.

19. König, B., Arendt, A., McDowell, J.H., Kahlert, M., Hargrave, P.A., and Hofmann, K.P., Proceedings of the National Academy of Science, USA, **86**, 6878-6882, 1989.

20. Dratz, E.A., Furstenau, J.E., Lambert, C.G., Thireault, D.L., Rarick, H., Schepers, T., Pakhlevaniants, S., and Hamm, H.E., Nature, **363**, 276-281, 1993.

21. Bax, A. and Lerner, L., Science, **232**, 960-967, 1986.

22. Wyssbrod, H.R., "The Use of Nuclear Magnetic Resonance Spectroscopy to Study Peptide Conformation," *Membrane Biophysics II: Physical Methods in the Study of Epithelia*, Alan R. Liss, Inc., 1983.

23. Kessler, H., Gehrke, M., and Griesinger, C., Angew. Chem. Int. Ed. Engl., **27**, 490-536, 1988.

24. Bax, A., "Two-Dimensional NMR and Protein Structure", *Annual Reviews of Biochemistry*, **58**, 223-256, 1989.

25. Farrar, T.C., Analytical Chemistry, **59**, 749A-761A, 1987.

26. Aue, W.P., Bartholdi, E., Ernst, R.R., Journal of Chemical Physics, **64**(5), 2229-2246, 1976.

27. Wüthrich, K., *NMR of Proteins and Nucleic Acids*, Wiley-Interscience, 1986.

28. Derome, A.E., *Modern NMR Techniques for Chemistry Research*, Pergamon, 1987.

29. Croasmun, W.R. and Carlson, R.M.K., *Two-Dimensional NMR Spectroscopy: Applications for Chemists and Biochemists*, VCH Publishers, 1987.

30. Abraham, R.J., Fisher, J., and Loftus, P., *Introduction to NMR Spectroscopy*, John Wiley and Sons, 1988.

31. Campbell, A.P. and Sykes, B.D., "The Two-Dimensional Transferred Nuclear Overhauser Effect: Theory and Practice," *Annual Reviews of Biophysical and Biomolecular Structure*, **22**, 99-122, 1993.

32. Wemmer, D.E., Concepts in Magnetic Resonance, **1**, 59-72, 1989.

33. Freeman, R., *A Handbook of Nuclear Magnetic Resonance*, Longman Scientific and Technical, 1988.

34. Bax, A. and Davis, D.G., Journal of Magnetic Resonance, **65**, 355-360, 1985.

35. Braunschweiler, L. and Ernst, R.R., Journal of Magnetic Resonance, **53**, 521-528, 1983.

36. Noggle, J.H. and Schirmer, R.E., *The Nuclear Overhauser Effect: Chemical Applications*, Academic Press, 1971.

37. Bothner-By, A.A., Stephens, R.L., Lee, J., Warren, C.D., Jeanloz, R.W., Journal of the American Chemical Society, **106**, 811-813, 1984.

38. Bax, A. and Davis, D.G., Journal of Magnetic Resonance, **63**, 207-213, 1985.

39. Balaram, P., Bothner-By, A.A., and Dadok, J., Journal of the American Chemical Society, **94**, 4015-4016, 1972.

40. Balaram, P., Bothner-By, A.A., and Breslow, J., Journal of the American Chemical Society, **94**, 4017, 1972.

41. Clore, G.M. and Gronenborn, A.M., Journal of Magnetic Resonance, **48**, 402-417, 1982.

42. Clore, G.M. and Gronenborn, A.M., Journal of Magnetic Resonance, **53**, 423-442, 1983.

43. Landy, S.B. and Rao, B.D., Journal of Magnetic Resonance, **81**, 371-377, 1989.

44. Campbell, A.P. and Sykes, B.D., Journal of Magnetic Resonance, **93**, 77-92, 1991.

45. Davis, D.G., Perlman, M.E., and London, R.E., Journal of Magnetic Resonance, in press.

46. London, R.E., Journal of Magnetic Resonance, in press.

47. London, R.E., Perlman, M.E., and Davis, D.G., Journal of Magnetic Resonance, **97**, 79-98, 1992.

48. Lippens, G.M., Cerf, C., and Hallenga, K., Journal of Magnetic Resonance, **99**, 268-281, 1992.

49. Nirmala, N.R., Lippens, G.M., and Hallenga, K., Journal of Magnetic Resonance, **100**, 25-42, 1992.

50. *Discover User Guide, Part 1*, version 2.8.0, San Diego: Biosym Technologies, 1992.

51. van Gunsteren, W.F. and Berendsen, H.J.C., Angew. Chem. Int. Ed. Engl., **29**, 992-1023, 1990.

52. van Gunsteren, W.F. and Mark, A.E., European Journal of Biochemistry, **204**, 947-961, 1992.

53. *NMRchitect User Guide*, version 1.0, San Diego: Biosym Technologies, 1992.

54. Nilges, M, Clore, G.M., and Gronenborn, A.M, FEBS Letters, **239**(1), 129-136, 1988.

55. Borgias, B.A., Thomas, P.D., Liu, H., and Kumar, A., *MARDIGRAS Documentation*, version 2.0, 1993.

56. Borgias, B.A. and James, T.L., Journal of Magnetic Resonance, **87**, 475-487, 1990.

57. Borgias, B.A., Thomas, P.D., Liu, H., and Kumar, A., *CORMA Documentation*, version 4.0, 1993.

58. Borgias, B.A., Gochin, M., Kerwood, D.J., and James, T.L., Progress in NMR Spectroscopy, **22**, 83-100, 1990.

59. Withka, J.M., Srinivasan, J., and Bolton, P.H., Journal of Magnetic Resonance, **98**, 611-617, 1992.

60. Kumar, A., Wagner, G., Ernst, R.R., and Wuthrich, K., Journal of the American Chemical Society, **103**, 3654-3658, 1981.

61. Bax, A., Sklenar, V., Clore, G.M., and Gronenborn, A.M., Journal of the American Chemical Society, **109**, 6511-6513, 1987.

62. Wuthrich, K., Science, **243**, 45-50, 1989.

63. Wright, P.E., Dyson, H.J., and Lerner, R.A., Biochemistry, **27**, 7167-7175, 1988.

64. Dyson, H.J., Rance, M., Houghten, R.A., Lerner, R.A., and Wright, P.E., Journal of Molecular Biology, **201**, 161-200, 1988.

65. Dyson, H.J., Rance, M., Houghten, R.A., Wright, P.E., and Lerner, R.A., Journal of Molecular Biology, **201**, 201-217, 1988.

66. Bax, A., Billeter, M., and Braun, W., Journal of Molecular Biology, **180**, 715-740, 1984.

67. Neuhaus, D. and Williamson, M.P., *The Nuclear Overhauser Effect in Structural and Conformational Analysis*, VCH Publishers, 1989.

68. Gross, K-H. and Kalbitzer, H.R., Journal of Magnetic Resonance, **76**, 87-99, 1988.

69. Schwartz, A.L. and Cutnell, J.D., Journal of Magnetic Resonance, **53**, 389-411, 1983.

70. Davis, A.L. and Wimperis, S., Journal of Magnetic Resonance, **84**, 620-626, 1989.

71. Zagorski, M.G., Journal of Magnetic Resonance, **86**, 400-405, 1990.

72. Marion, D., Ikura, M., and Bax, A., Journal of Magnetic Resonance, **84**, 425-430, 1989.

73. Summers, M.F., Marzilli, L.G. and Bax, A., Journal of the American Chemical Society, **108**, 4285-4294, 1986.

74. Laussac, J-P., Cung, M-T., Pasdeloup, M., Haran, R., Marraud, M., Lefrancier, P., Dardenne, M., and Bach, J-F., Journal of Biological Chemistry, **261**, 7784-7790, 1986.

75. Kessler, H., Bats, J.W., Griesinger, C., Koll, S., Will, M., and Wagner, K., Journal of the American Chemical Society, **110**, 1033-1049, 1988.

76. Heitz, A., Chiche, L., Le-Nguyen, D., and Castro, B., Biochemistry, **28**, 2392-2398, 1989.

77. Fry, D.C., Madison, V.S., Bolin, D.R., Breeley, D.N., Toome, V., and Wegrzynski, B.B., Biochemistry, **28**, 2399-2409, 1989.

78. Osterhout, J.J. Jr., Baldwin, R.L., York, E.J., Stewart, J.M., Dyson, H.J., and Wright, P.E., Biochemistry, **28**, 7059-7064, 1989.

79. Saudek, V. and Pelton, J.T., Biochemistry, **29**, 4509-4515, 1990.

80. Ostheimer, G.J., Starkey, J.R., Lambert, C.G., Helgerson, S.L., and Dratz, E.A., Journal of Biological Chemistry, **267**, 25120-25128, 1992.

81. Motta, A., Morelli, M.A.C., Goud, N., and Temussi, P.A., Biochemistry, **28**, 7996-8002, 1989.

82. Weiss, M.A., Hua, Q-X., Lynch, C.S., Frank, B.H., and Shoelson, S.E., Biochemistry, **30**, 7373-7389, 1991.

83. Banks, K.M., Hare, D.R., and Reid, B.R., Biochemistry, **28**, 6996-7010, 1989.

84. Campbell, A.P. and Sykes, B.D., Journal of Molecular Biology, **222**, 405-421, 1991.

85. Campbell, A.P., VanEyk, J.E., Hodges, R.S., and Sykes, B.D., Biochemica et Biophysica Acta, **1160**, 35-54, 1992.

86. Anglister, J., Levy, R., and Scherf, T., Biochemistry, **28**, 3360-3365, 1989.

87. Scherf, T., Hiller, R., Naider, F., Levitt, M., and Anglister, J., Biochemistry, **31**, 6884-6897, 1992.

88. Scherf, T. and Anglister, J., Biophysical Journal, **64**, 754-761, 1993.

89. Holak, T.A., Nilges, M., and Oschkinat, H., FEBS Letters, **242**(2), 218-224, 1989.

90. Holak, T.A., Gondol, D., Otlewski, J., and Wilusz, T., Journal of Molecular Biology, **210**, 635-648, 1989.

91. Habazettl, J., Cieslar, C., Oschkinat, H., and Holak, T.A., FEBS Letters, **268**(1), 141-145, 1990.

92. Levy, R.M., Bassolino, D.A., Kitchen, D.B., and Pardi, A., Biochemistry, **28**, 9361-9372, 1989.

93. Klaus, W., Dieckmann, T., Wray, V., Schomburg, D., Wingender, E. and Mayer, H., Biochemistry, **30**, 6936-6942, 1991.

94. Plateau, P. and Guéron, M., Journal of the American Chemical Society, **104**, 7310, (1982).

95. Bax, A., Ikura, M., Kay, L.E., and Zhu, G., Journal of Magnetic Resonance, **91**, 174-178, 1991.

96. Marion, D. and Bax, A., Journal of Magnetic Resonance, **79**, 352, 1988.

97. Boelens, R., Koning, T.M.G., van der Marel, G.A., van Boom, J.H., and Kaptein, R., Journal of Magnetic Resonance, **82**, 290-308, 1989.

98. Bourne, H.R., Sanders, D.A., and McCormick, F., Nature, **348**, 125-132, 1990.

99. Noel, J.P., Hamm, H.E., and Sigler, P.B., Nature, **366**, 654-663, 1993.

100. Lambright, D.G., Noel, J.P., Hamm, H.E., and Sigler, P.B., Nature, **369**, 621-628, 1994.

101. Lipari, G. and Szabo, A., Journal of the American Chemical Society, **104**, 4546, 1982.

102. Clore, G.M. and Gronenborn, A.M., "Determination of Three-Dimensional Structure of Proteins and Nucleic Acids in Solution by NMR Spectroscopy," *CRC Critical Reviews in Biochemistry and Molecular Biology*, **24**, 479-564, 1989.

103. Clore, G.M. and Gronenborn, A.M., Progress in NMR Spectroscopy, **23**, 43-92, 1991.

104. Clore, G.M. and Gronenborn, A.M. (eds.), *NMR of Proteins*, CRC Press, 1993.

105. Opella, S.J., "NMR Approaches to Membrane Protein Structure," *Membrane Protein Structure: Experimental Approaches*, Oxford, 1993.

APPENDIX

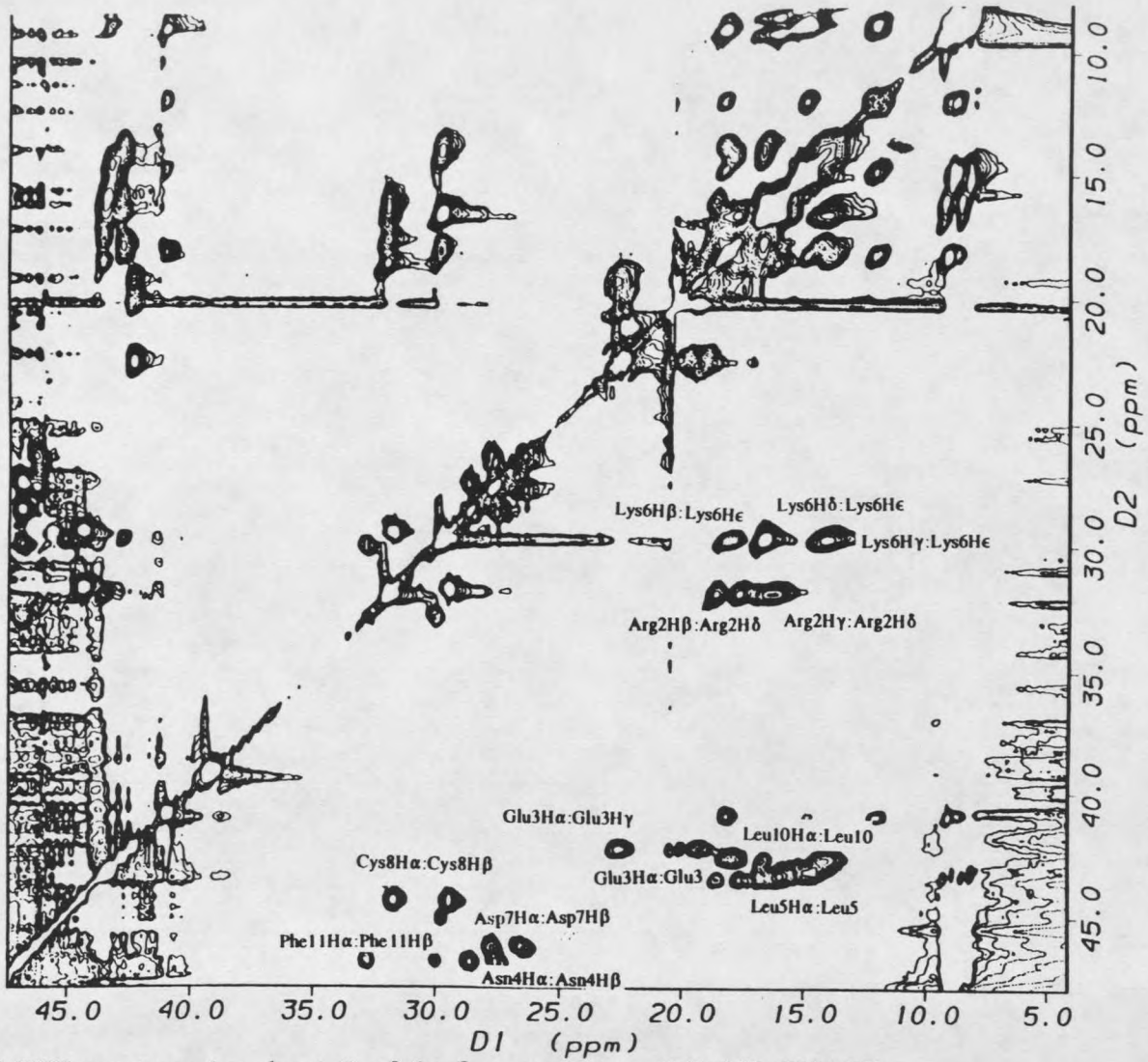


Figure 51. TOCSY spectrum (quadrant 1) of the free peptide Ac-340-350 (K341R).

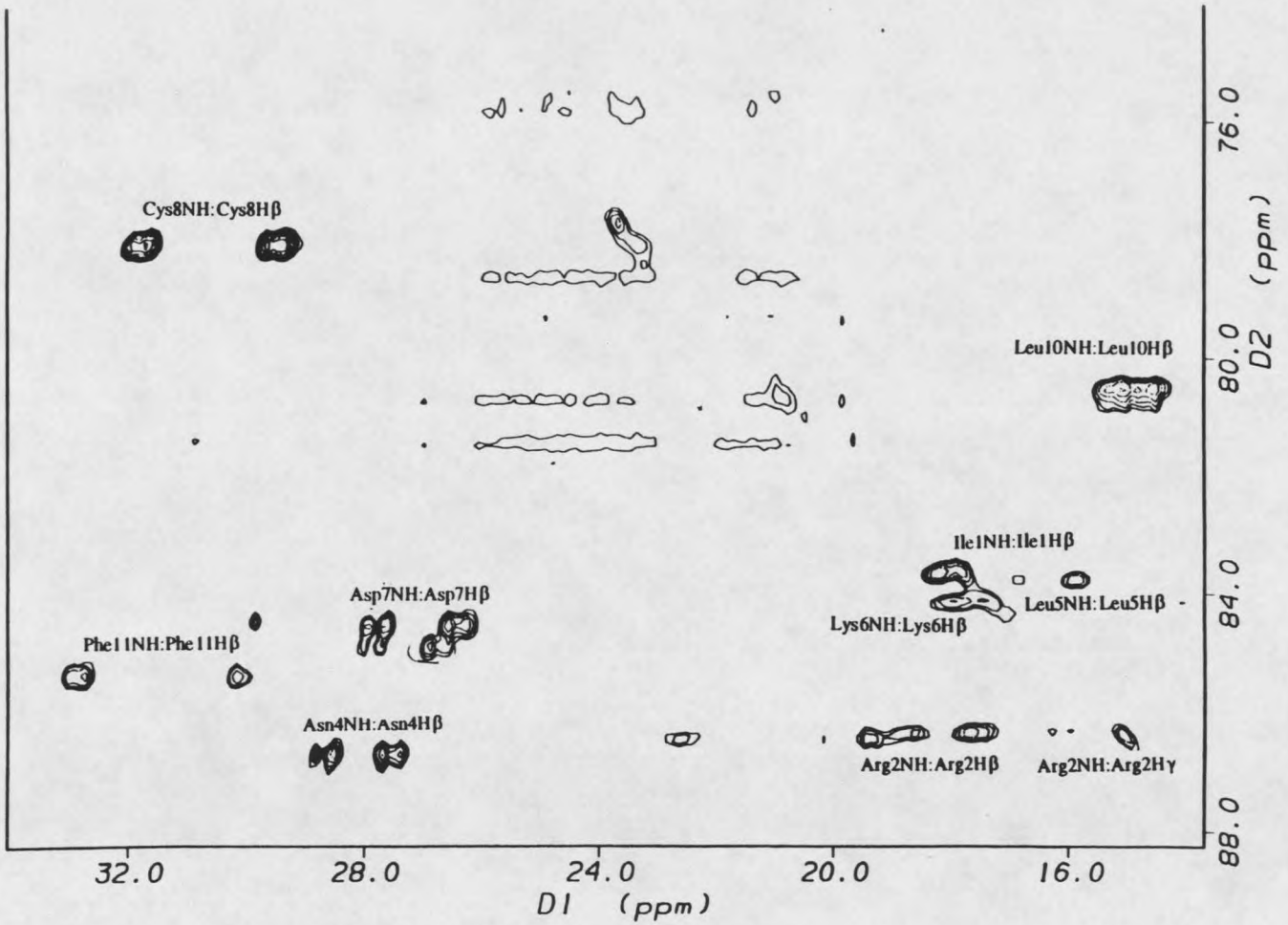


Figure 52. TOCSY spectrum (quadrant 4) of the free peptide Ac-340-350 (K341R).

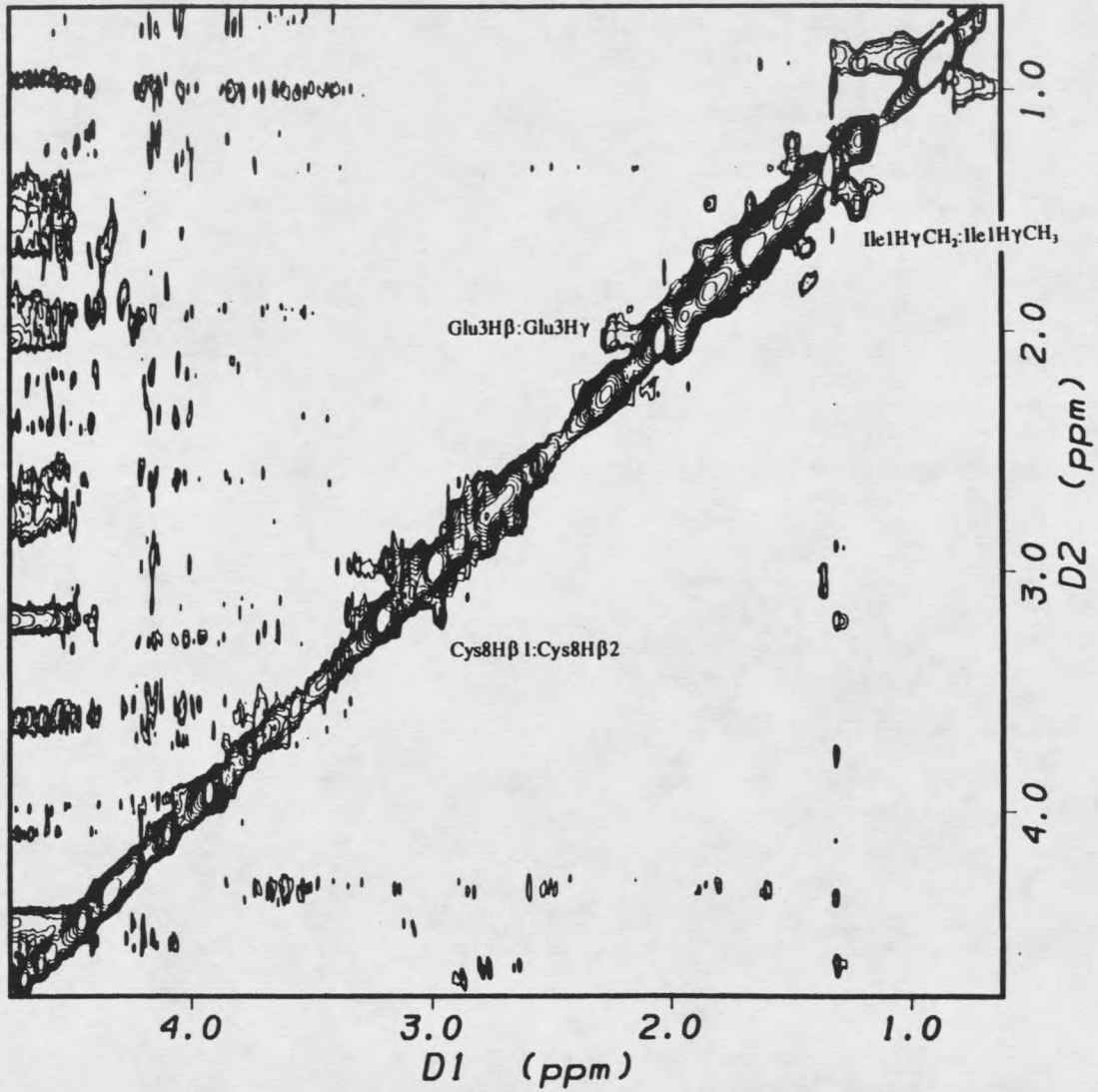


Figure 53. NOESY spectrum (quadrant 1) of the free peptide Ac-340-350 (K341R).

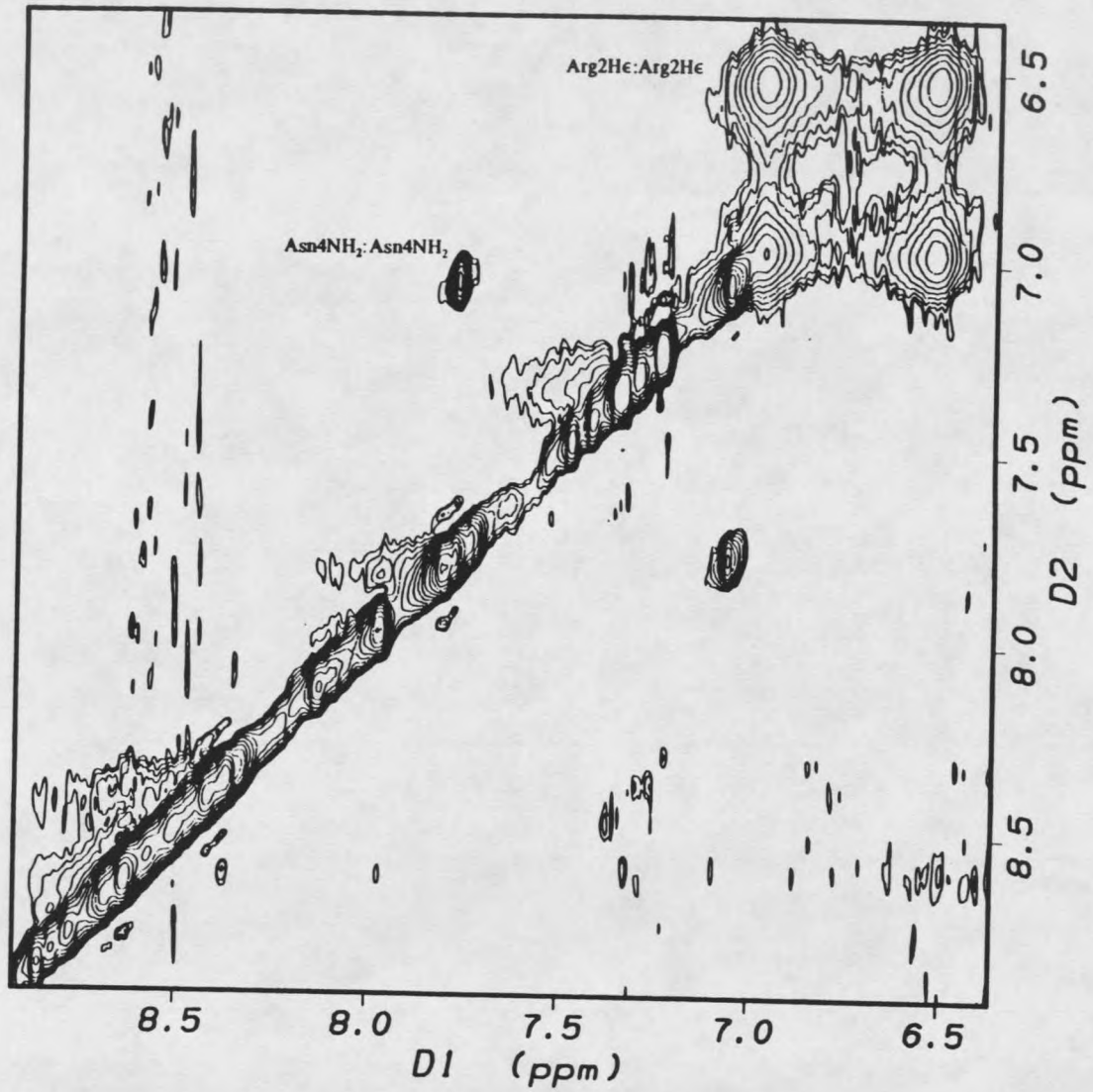


Figure 54. NOESY spectrum (quadrant 3) of the free peptide Ac-340-350 (K341R).

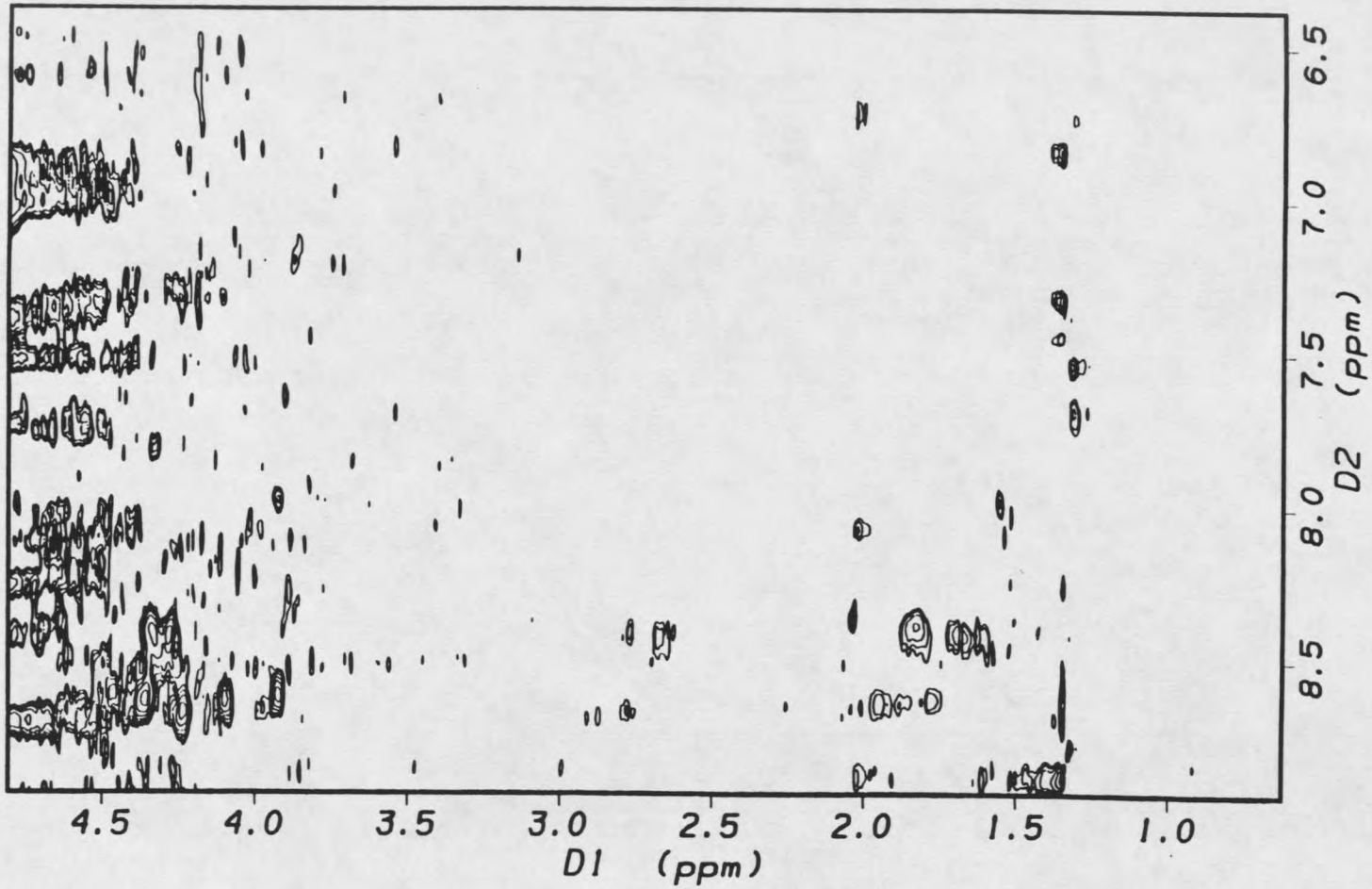


Figure 55. NOESY spectrum (quadrant 4) of the free peptide Ac-340-350 (K341R).

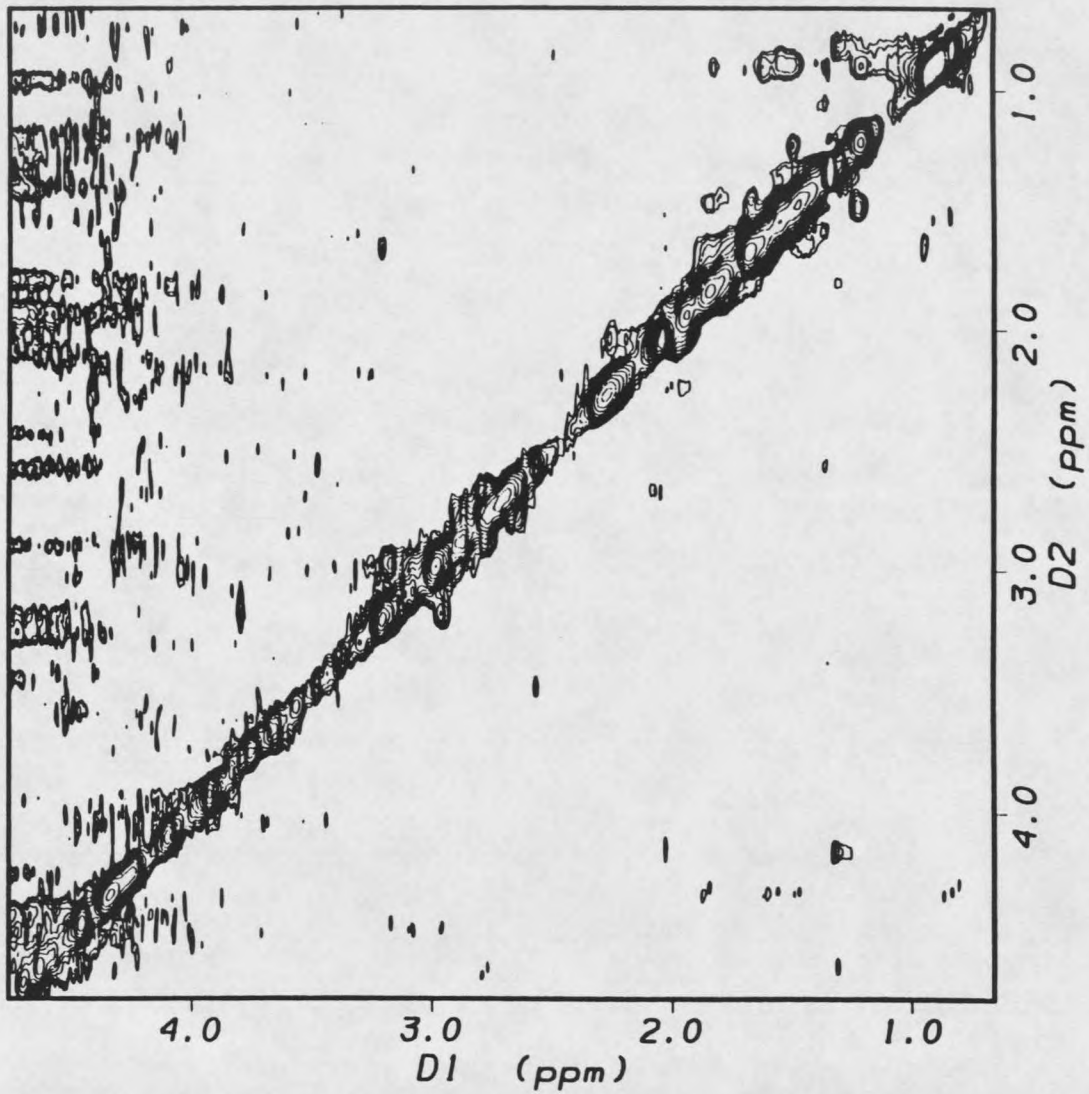


Figure 56. NOESY spectrum (quadrant 1) of the peptide Ac-340-350 (K341R) and rhodopsin (dark) in a 15:1 molar ratio.

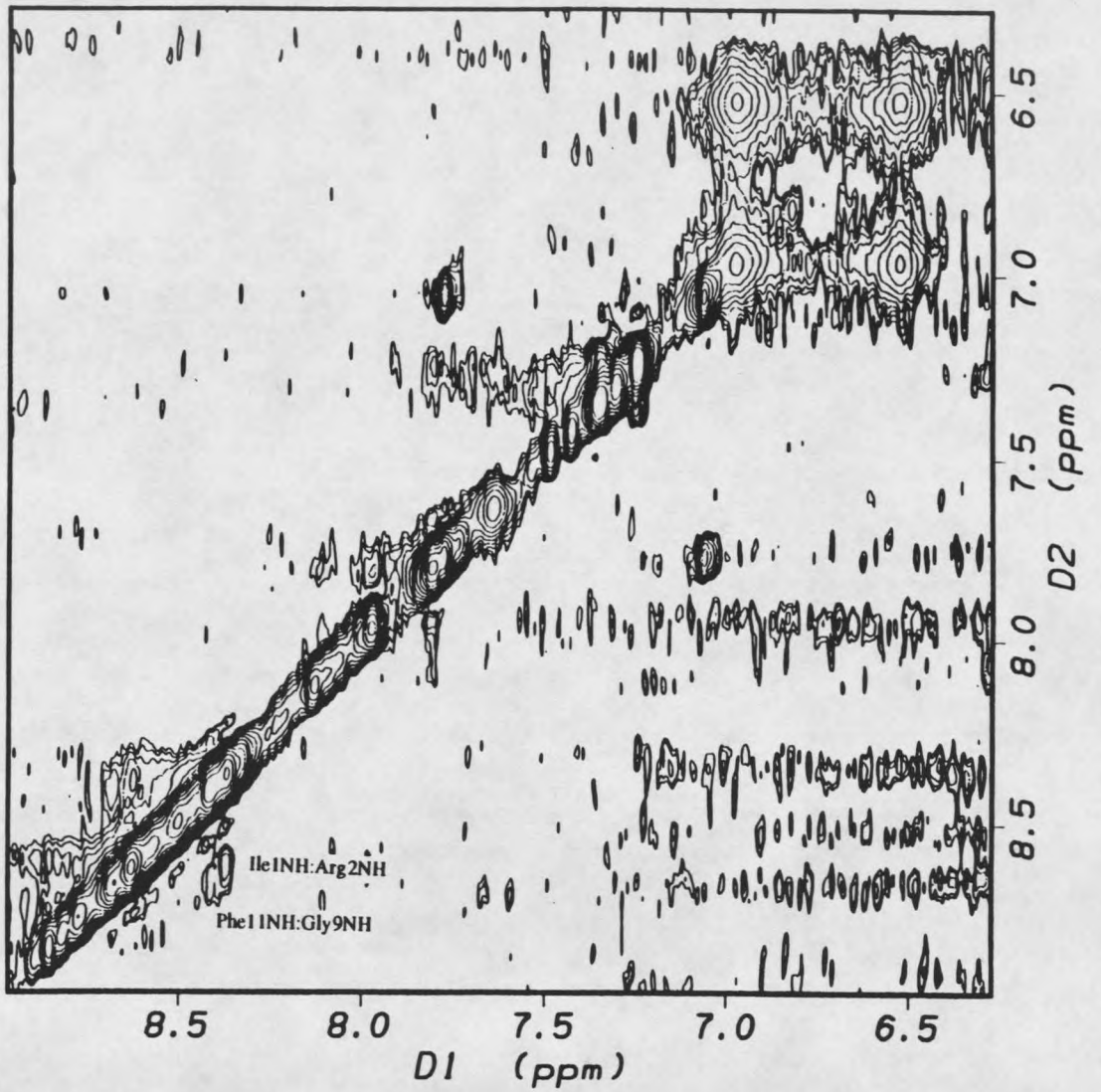


Figure 57. NOESY spectrum (quadrant 3) of the peptide Ac-340-350 (K341R) and rhodopsin (dark) in a 15:1 molar ratio.

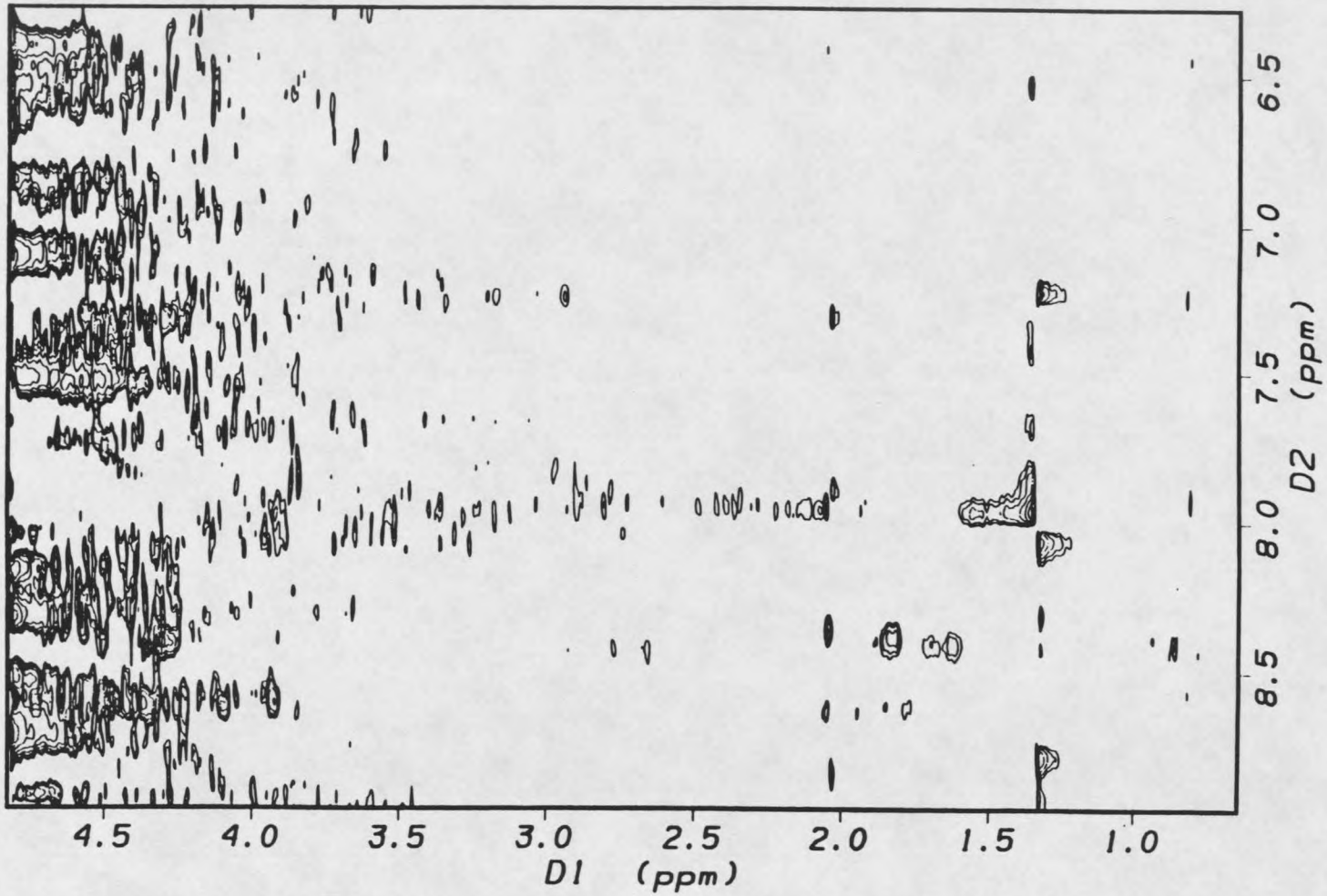


Figure 58. NOESY spectrum (quadrant 4) of the peptide Ac-340-350 (K341R) and rhodopsin (dark) in a 15:1 molar ratio.

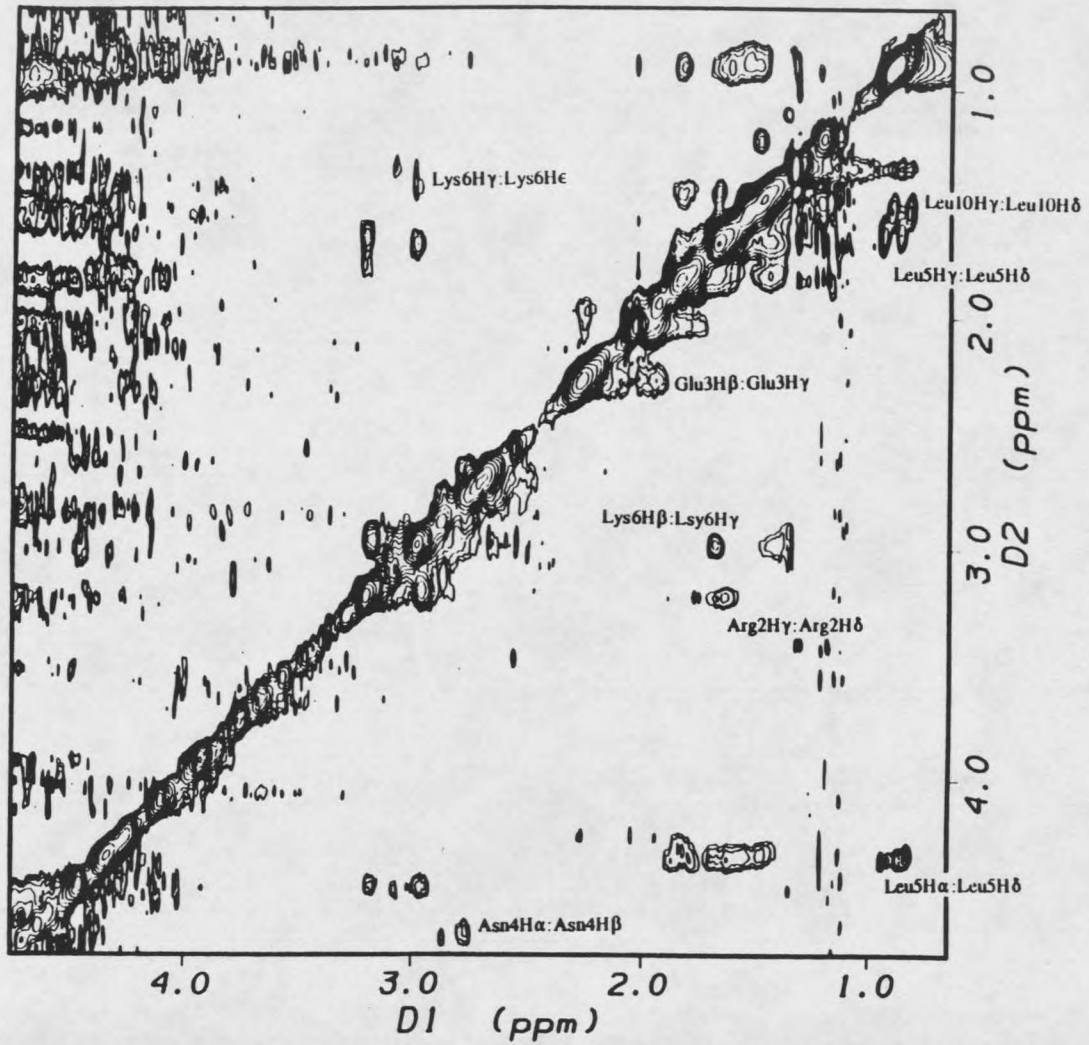


Figure 59. NOESY spectrum (quadrant 1) of the peptide Ac-340-135 (K341R) and metarhodopsin II (light) in a 15:1 molar ratio.

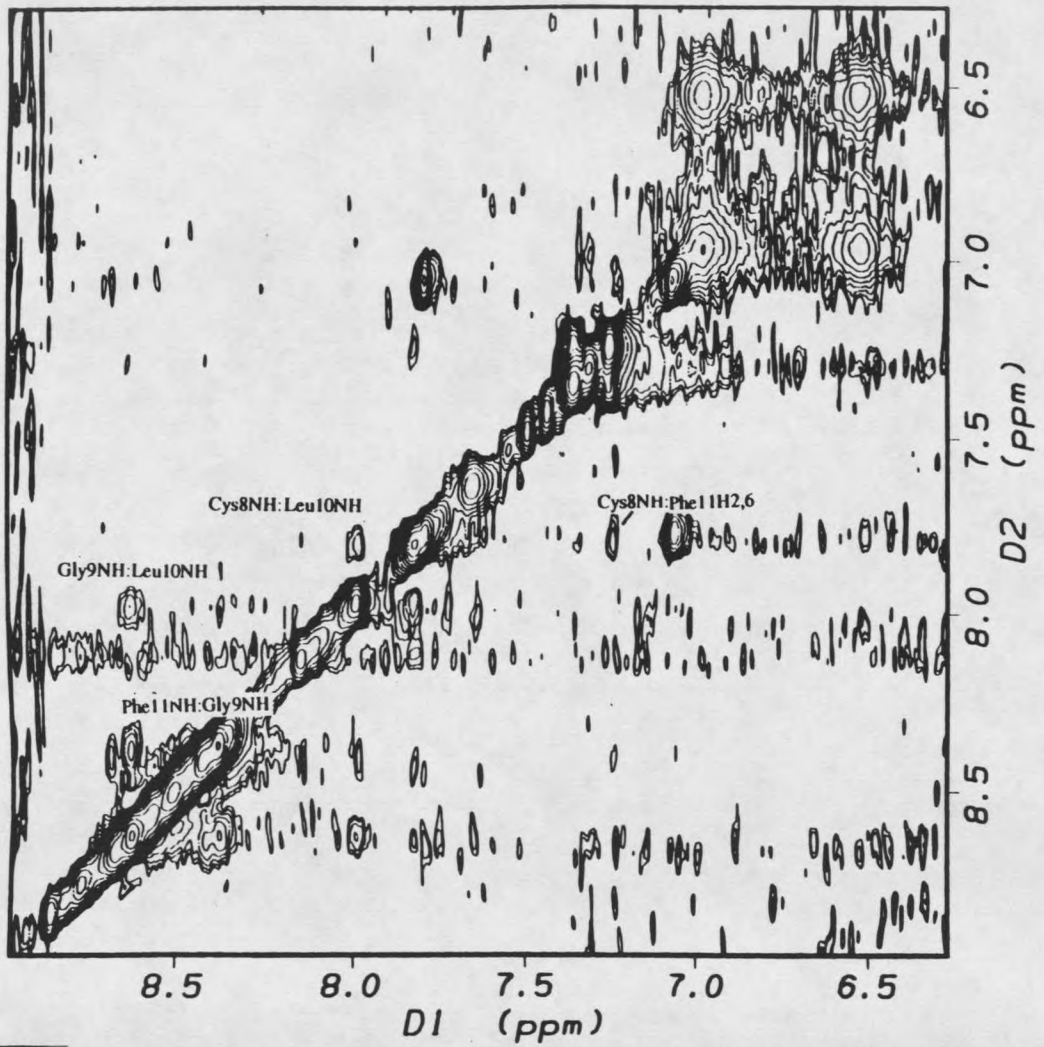


Figure 60. NOESY spectrum (quadrant 3) of the peptide Ac-340-350 (K341R) and metarhodopsin II (light) in a 15:1 molar ratio.

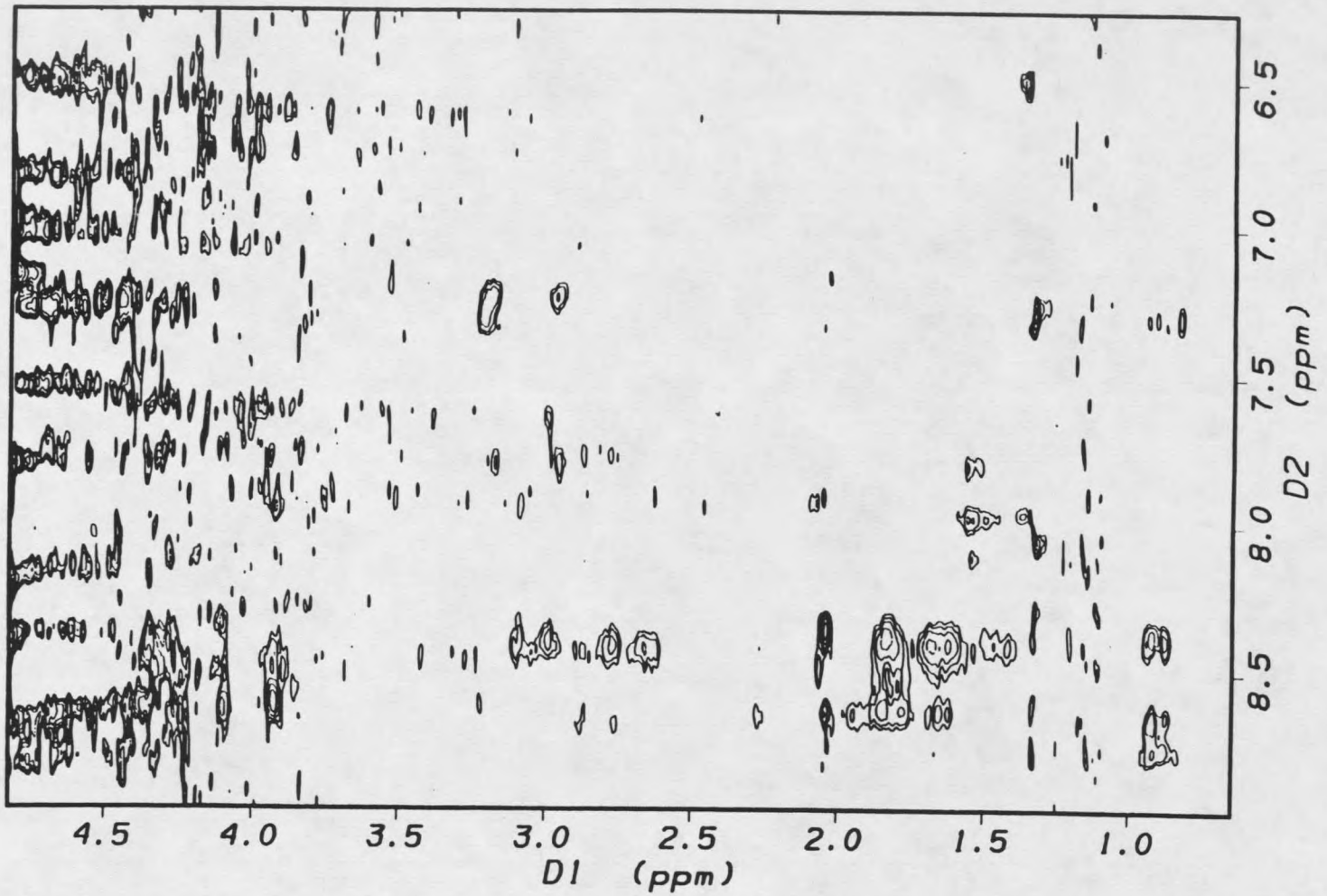


Figure 61. NOESY spectrum (quadrant 4) of the peptide Ac-340-350 (K341R) and metarhodopsin II (light) in a 15:1 molar ratio.

MONTANA STATE UNIVERSITY LIBRARIES
3 1762 10254038 0

HOUCHEN
BINDERY LTD
UTICA/OMAHA
NE.